

CRANFIELD UNIVERSITY



Joseph M. Hatt

**MECHANICAL DESIGN ASPECTS OF A TRI-AXIAL
ACCELEROMETER**

**SCHOOL OF INDUSTRIAL AND MANUFACTURING
SCIENCE**

MPhil THESIS

ProQuest Number: 10832221

All rights reserved

INFORMATION TO ALL USERS

The quality of this reproduction is dependent upon the quality of the copy submitted.

In the unlikely event that the author did not send a complete manuscript and there are missing pages, these will be noted. Also, if material had to be removed, a note will indicate the deletion.



ProQuest 10832221

Published by ProQuest LLC (2018). Copyright of the Dissertation is held by Cranfield University.

All rights reserved.

This work is protected against unauthorized copying under Title 17, United States Code
Microform Edition © ProQuest LLC.

ProQuest LLC.
789 East Eisenhower Parkway
P.O. Box 1346
Ann Arbor, MI 48106 – 1346

CRANFIELD UNIVERSITY

**SCHOOL OF INDUSTRIAL AND MANUFACTURING
SCIENCE**

MPhil THESIS

Academic Year 2003 – 2004

Joseph M. Hatt

**MECHANICAL DESIGN ASPECTS OF A TRI-AXIAL
ACCELEROMETER**

Supervisor Dr P. Kirby

June 2004

This Thesis is submitted in partial fulfilment of the requirements for the degree
of Master of Philosophy

© Cranfield University 2004. All rights reserved. No part of this publication may
be reproduced without the written permission of the copyright owner.

Abstract

This work describes the development of computer models for the design of a novel three-axis silicon accelerometer with thin-film PZT piezo-electric sensing. Theoretical and finite element methods are used to predict the resonant frequencies, resonant mode shapes, and charge sensitivity of the accelerometers. The strengths of each analytical method are used to allow the identification of trends in geometrical affects, and to optimise the design with respect to specification objectives for a commercial device.

The theoretical models have been developed and refined in conjunction with practical fabrication trials. This has allowed the material properties to be derived, specific to the thin-film deposition method used, and incorporated onto the models. The practical fabrication process has raised a number of unforeseen issues, and these have led to changes from the original design. These changes have been analysed with the theoretical models, and revised performance predictions produced. The practical findings are consistent with the revised predictions, and achieve close to the desired performance specification.

Acknowledgements

Thanks for support and assistance are due to: Dr Diana Hodgins and Ian Braithwaite of ETB for guidance on writing-up and advice on electronic design and signal noise issues;

Dr Paul Kirby, my supervisor, Ming Yu Lim, Meiling Zhu and Rob Wright of Cranfield University for their support and for fabricating the physical samples;

Paul Towers of Towers Associates for design of the electronic charge amplifier;

the STAMP project partners involved in aspects of testing;

and Juliette, my wife.

Contents

1. Introduction	1
1.1. Project Background	1
1.2. Objectives	1
1.3. Requirements of the Accelerometer	2
1.4. Structure of the Thesis	3
2. Literature Search and Background	5
2.1. Introduction	5
2.2. Existing Accelerometers	5
2.2.1. Conventional Piezo-electric sensors	6
2.2.2. MEMS Piezo-resistive sensors	6
2.2.3. MEMS Capacitive sensors	7
2.2.4. MEMS Piezo-electric sensors	7
2.3. Accelerometer Design Theory	8
2.3.1. Proposed Mechanism for a Tri-axial Piezo-electric Accelerometer	8
2.3.2. Concept Prototypes	9
2.3.3. Multi-layer Beam structures	9
2.3.4. Material Properties	10
2.4. Patents	11
2.5. Related Standards for Accelerometer Applications	12
2.6. Conclusions	12
3. Theory and Modelling - Mathematical models	14
3.1. Purpose for the mathematical models	14
3.2. Construction of the models	14
3.3. Selection of Modelling Configurations	16
3.3.1. Single Axis, Semi-symmetrical Devices	17
3.3.2. Two Axis, Highly Symmetrical Devices	18

3.3.3.	Rotationally Symmetrical Devices	19
3.3.4.	Novel, Multi-beam Devices	19
3.4.	Derivation of the Mathematical Models	20
3.4.1.	Strain in the Beams	21
3.4.2.	Generating Charge from Strain	22
3.4.3.	Non-linearity of Beam Deformations	23
3.4.4.	Effect of the Piezo-electric Sensor on Beam Stiffness	25
3.5.	Generic Features Affecting the Design	26
3.5.1.	Etching Method	26
3.5.2.	Wafer Thickness	26
3.5.3.	Beam Thickness	28
3.5.4.	Electrode Patterning	28
3.6.	Mathematical predictions	29
3.6.1.	Single Axis, Semi-symmetrical Devices	30
3.6.2.	Two Axis, Highly Symmetrical Devices	31
3.6.3.	Rotationally Symmetrical Devices	32
3.6.4.	Modified Semi-symmetrical Design	32
3.7.	Conclusions	33
4.	Finite Element Modelling	44
4.1.	Purpose for the Finite Element models	44
4.2.	Approach to Modelling using NISA	44
4.3.	Material Characteristics	46
4.3.1.	Self Excitation of PZT	46
4.4.	Verification of the beam models	47
4.4.1.	FE analysis Models	47
4.4.2.	Verification Calculations	48
4.4.3.	Verification Results	49
4.5.	Large Deflection Theory	50
4.6.	Finite Element predictions	51
4.6.1.	Distribution of the PZT Film	51
4.6.2.	Self Excitation of PZT	52
4.6.3.	Voltage Output from PZT sensors	53
4.6.4.	Response of the Devices	53
4.6.5.	Positional Tolerance	54
4.7.	Discussion of FE models	54
4.7.1.	Correlation Between Maths and FE	54

4.7.2.	Distribution of the Applied PZT Film	56
4.7.3.	Voltage Output from PZT sensors.....	56
4.8.	Comparison of FE and mathematical models.....	57
5.	Prototype Manufacturing.....	71
5.1.	Physical prototype Fabrication	71
5.2.	Sensor Fabrication Issues	72
5.2.1.	Oversize DRIE on the handle wafer	72
5.2.2.	Buried Oxide Layer etching sequence.....	73
5.2.3.	Effect of stress in the PZT and Platinum electrodes.....	73
5.2.4.	Effect of PZT layer thickness.....	74
5.2.5.	Poling the PZT	75
5.2.6.	Connection of the Electrodes	77
5.2.7.	Mounting of the Sensor Die	77
5.2.8.	Package Design	78
5.3.	Practical implications on the models.....	79
6.	Analysis of the Test Results.....	87
6.1.	Test Objectives.....	87
6.2.	Bare die testing	87
6.2.1.	Sensor capacitance.....	87
6.2.2.	Device isolation	88
6.2.3.	Drive and pick-off	88
6.3.	Laboratory characterisation	89
6.3.1.	Sensitivity.....	89
6.3.2.	Resolution	90
6.3.3.	Frequency response	91
6.3.4.	Amplitude non-linearity.....	91
6.3.5.	Resonant frequency	91
6.3.6.	Cross-axis sensitivity	92
6.3.7.	Temperature	92
6.3.8.	Shock limit / Structural strength.....	92
6.4.	Summary of Testing.....	93
7.	Conclusions and Recommendations	95
7.1.	Model construction.....	95
7.2.	Physical Prototypes.....	95
7.3.	Revision of material properties.....	96

7.4. Future work.....	96
References.....	98
Appendix 1. MathCAD models	105
1.1. Highly symmetrical design.....	106
1.2. In-plane sensing	109
1.3. Multi-layer beam stiffness.....	112
Appendix 2. Table of dimensions for proposed devices.....	113
Appendix 3. Drawings for Prototype Accelerometers	115
TAA001. Three axis sensor	116
TAA002. Oversize, high output sensor	117
TAA003. Single axis, highly symmetrical sensor.....	118
Appendix 4. Scaling Factor Analysis	119
Appendix 5. Full Results from Ground Acceleration FE	121
Appendix 6. Signal Coupling in the Device-Layer Silicon.....	125

Tables

Table 1-1 Target Specification for the STAMP accelerometer	4
Table 4-1 Displacement from 50g Z-axis acceleration.....	59
Table 4-2 TAA001 Z axis sensor - both sides of PZT layer held to zero volts	59
Table 4-3 TAA001 Y axis sensor - both sides of PZT layer held to zero volts	59
Table 4-4 TAA002 High Output sensor - both sides of PZT layer held to zero volts ...	60
Table 4-5 TAA003 Z axis sensor - both sides of PZT layer held to zero volts	60
Table 4-6 TAA001 Y axis sensor Predicted resonant frequencies.....	61
Table 4-7 TAA001 Relative open circuit Voltage Output calculated using NISA	61
Table 4-8 TAA001 Y-axis sensor Charge response.....	62
Table 4-9 TAA001 Z-axis sensor Charge response	62
Table 4-10 TAA002 Connected as a Y-axis sensor Charge response.....	63
Table 4-11 TAA002 Connected as a Z-axis sensor Charge response	63
Table 4-12 TAA003 Z-axis sensor Charge response	64
Table 4-13 TAA001 Y-axis sensor Charge response. 2um offset.....	64
Table 4-14 TAA001 Z-axis sensor Charge response. 2um offset.....	65
Table 4-15 TAA002 Connected as a Y-axis sensor Charge response. 2um offset	65
Table 4-16 TAA002 Connected as a Z-axis sensor Charge response. 2um offset.....	66
Table 4-17 TAA003 Z-axis sensor Charge response. 2um offset.....	66
Table 5-1 Effect of 20µm over-size on the DRIE rear-side etching.....	80
Table 5-2 FE results for stress between layers.....	81
Table 5-3 Effect of beam construction on beam stiffness and signal strength	81

Figures

Figure 2-1 Typical construction of a beam with PZT sensors ²⁸	13
Figure 2-2 Variation in silicon properties with orientation to the crystal lattice	13
Figure 3-1 Schematic layout for the three-axis accelerometer die	35
Figure 3-2 Acceleration out of the plane of the beams	35
Figure 3-3 Acceleration along the length of the beams	36
Figure 3-4 Acceleration Perpendicular to the Length of the Beams	36
Figure 3-5 Two-beam configuration of semi-symmetrical accelerometer ¹⁷	36
Figure 3-6 Schematic of semi-symmetrical design	37
Figure 3-7 Schematic of beams inset into semi-symmetrical design	37
Figure 3-8 4-beam highly symmetrical accelerometer	38
Figure 3-9 Highly symmetrical device	38
Figure 3-10 Inset Highly Symmetrical Design	39
Figure 3-11 Rotationally symmetrical device with offset beams	39
Figure 3-12 Modified Semi-Symmetrical Device with End Supports	40
Figure 3-13 Dependence of charge output on wafer thickness	40
Figure 3-14 Dependence of charge output on wafer thickness	41
Figure 3-15 Dependence of charge output on beam thickness	41
Figure 3-16 Increasing beam separation	42
Figure 3-17 Increasing beam width	42
Figure 3-18 Beams inset into the Proof mass	43
Figure 3-19 Graph showing affect of inset beams on charge output (constant mass)....	43
Figure 4-1 FE model of Z-axis sensor TAA001	67
Figure 4-2 FE model of X- or Y-axis sensor TAA001	67

Figure 4-3 FE model of High output Z-axis sensor (Oversize) TAA002.....	67
Figure 4-4 FE model of Z-axis sensor TAA003	68
Figure 4-5 Stress distribution in a deformed beam	68
Figure 4-6 FE model for validating beam element aspect ratio	69
Figure 4-7 Voltage generation from Y-axis acceleration	69
Figure 4-8 TAA001 Electrode numbering	70
Figure 5-1 SEM photograph from the rear of wafer 1 showing DRIE under-cut	82
Figure 5-2 Poling direction and Electrical Connections for Sensing	82
Figure 5-3 Graph of Change in Segment Capacitance against Polarisation Voltage.....	83
Figure 5-4 Graph of Change in Segment Capacitance against Polarisation Time	83
Figure 5-5 View of Prototype PCB (amplifier side) and Package	84
Figure 5-6 View of Prototype Accelerometer - Sensor Side	85
Figure 5-7 Assembled Prototype Accelerometer and Package.....	85
Figure 5-8 Prototype Accelerometer Package Circuit Diagram	86
Figure 6-1 Frequency sweep response to 500mV-peak Drive signal.....	94
Figure 6-2 Accelerometer response to 1 to 20g input signals.....	94

1. Introduction

1.1. Project Background

Accelerometers detect the change of velocity of an object by measuring the force required to accelerate a known mass. They have been in industrial use for many years, and have many applications. By measuring the frequencies and level of vibration in a machine, noise sources can be identified, expected fatigue life can be estimated, and the condition of bearings can be monitored. By double integrating the output from a set of accelerometers, relative position data can be generated (although this is subject to rapid drift from accumulated errors) and in combination with other sensors this is used for navigational systems. However, as with any measurement system, the use of the sensor can influence the subject being measured, and for accelerometers, the mass of the sensor is critical. This has led to the development of increasingly small devices, both by miniaturising conventional assemblies, and by the development of micro-machined or MEMS (Micro Electro-Mechanical System) sensors.

The subject of this study originated from a European funded CRAFT project, working in partnership with Dr P. Kirby of Cranfield University, amongst others. The project acronym is STAMP – Silicon Tri-axial Accelerometer Vibration Measurement Project. The STAMP objective was to develop a three-axis MEMS accelerometer as a planar silicon structure. The key features of the accelerometer are minimal weight and high resolution at a modest cost.

1.2. Objectives

This work primarily considers the Mechanical Design Aspects of a Tri-Axial Accelerometer, but requires an understanding of how this mechanical component fits into the working system.

The objectives are:

- o to collate and interpret information from a range of sources, in order to understand the current knowledge of micro-fabricated accelerometer design.

- o to develop new mathematical and FE models for a range of micro-fabricated accelerometer designs.
- o to use these newly developed models to predict the response of the accelerometer designs, in order that characteristic trends may be identified, and to create a set of prototype designs.
- o to verify the models by comparison with functional prototypes, produced by Cranfield University.
- o to use the verified models to predict the performance of a three-axis accelerometer design against a functional specification.

With piezo-electric devices, integration or charge amplification electronics is considered essential, in order to maintain a workable signal-to-noise ratio. Design of the on-board charge-amplifier electronics was obtained from Paul Towers, an expert in this field, and an electrical performance model was created by Ian Braithwaite, in order to help the understanding and assessment of the sensor.

1.3. Requirements of the Accelerometer

The configuration of the accelerometer was strongly influenced by the existing knowledge of the STAMP partners. It was defined that the sensing method for the accelerometer would be to use thin-film PZT as strain gauges, to detect the flexing of beams.

The accelerometer design has been tailored to meet specific commercial requirements, covering a number of applications for human interface vibration measurement, and human motion study. From these applications, a target specification was agreed between the STAMP partners, and this was used as the focus for design optimisation. The performance ranges for the applications are:

- o Hand Arm Vibration measurement – typically requiring 0.8 - 2000Hz frequency range, and 100m/s^2 (10g) maximum acceleration.
- o Whole Body Vibration measurement – typically requiring 0.1 - 400Hz frequency range, and 100m/s^2 (10g) maximum acceleration.
- o Ambulatory Motion and Posture Study – DC to 64Hz sample rate, 100m/s^2 (10g) maximum acceleration.
- o Ground and Building Vibration measurement – generally low frequency (DC to 100Hz), and up to 500m/s^2 (50g).

From a combination of these applications and existing equipment requirements, the STAMP target specification was created. This is shown in Table 1-1. The DC requirement cannot be achieved with piezo-electric devices, due to the dissipation of charge with time, but by careful design of the electronics very low frequency readings can be achieved. The zero-drift associated with some DC accelerometers can be

confused with low frequency inputs, particularly in positional or navigational systems. It was consciously decided to use the low power advantages of the piezo-electric sensing system, and accept the low frequency cut-off.

To meet this specification, the sensor must include amplifiers and a temperature reference. The electronic design has a huge influence on many factors, and must work in unison with the sensor, so was considered from an early stage of development.

1.4. Structure of the Thesis

The thesis is divided into seven chapters. Tables and figures are grouped at the end of each chapter, whilst references and appendices are at the end of the thesis. This Introduction chapter has explained the reasons for undertaking the research, and set the objectives. Chapter 2 presents the background knowledge of existing sensors, and the origins of the theory that forms the basis of the modelling.

Chapters 3 to 5 detail the construction of theoretical, finite element and practical models, and present the results obtained from them. Two theoretical methods were used, since each has its own advantages, and comparison leads to increased confidence in the results. Mathematical modelling allows the rapid identification of trends, either by inspection of the formulae, or from the calculation of a series of example values. The finite element models contain fewer assumptions on the geometry of the structures, but are time consuming to run. All of the theoretical work relies on assumptions about the behaviour of the structure, and the use of correct material data.

The theoretical model and physical prototype results are compared and discussed in Chapter 6. What had been thought to be negligible effects became apparent as the physical prototyping and testing progressed, and the origin of these discrepancies was investigated. Finally, conclusions are drawn, and unresolved discrepancies are presented as the subject for future work.

Table 1-1 Target Specification for the STAMP accelerometer

Dynamic	
Acceleration Range	± 50 g
Sensitivity	80 mV/g
Resolution	0.001 g
Amplitude Response (within ± 5%)	0.5 - 2000 Hz
Amplitude non-linearity	3% FS
Resonant Frequency	>5 kHz
Cross Axis Sensitivity	< 1%
Electrical	
Supply Voltage	± 5 Vdc
Supply Current (max)	2 mA per axis
Charge Amplifier Output Impedance	< 1 kohm
Environmental	
Operating Temp Range	-20 to +85 C
Temperature Drift	0.01 %/°C with compensation
Storage Temp Range	-50 to +250 C (sensor module)
Shock Limit	1000 g
Physical	
Dimensions	10 x 5 x 5 mm
Mass	0.6 gram
Sealing	Hermetic Glass/Silicon die

This table was derived from the STAMP project requirements.

2. Literature Search and Background

2.1. Introduction

Through the decades of research and development, which have already been focused on accelerometer design, there have been many ingenious designs devised, and many pitfalls encountered. Ignoring this wealth of information is both ignorant, and insulting to those who have gone before. For these reasons, the literature search has considered a number of alternative sensing systems and mechanisms beyond the obvious scope of the piezo-electric MEMS sensor proposed.

The literature search covers the current products available, and details their modes of operation. It then investigates recent papers related primarily to the design of beam-type MEMS (Micro Electro-Mechanical System) accelerometers, in particular the type using strain-gauge sensing of the flexure of the beams. Finally, there is a search for patents related to strain-gauge accelerometers.

2.2. Existing Accelerometers

There is a well-established market for accelerometers, which is served by a number of major players, and further selection of small companies. A number of miniature devices have been created, based on established and new technology, which are well suited to the study of lightweight machines, and have seen successful application to human motion and vibration measurement.

Accelerometers are used in a multitude of applications where the motion or vibration of an object is of interest. From their industrial origins, accelerometers are usually designed to be bolted securely to a piece of machinery. Typical dynamic applications include bearing condition monitoring, fatigue life prediction, or NVH study (noise, vibration and harshness). Low frequency or static applications include inclinometers, pedometers, and navigational systems. Human subjects provide less suitable mounting points, and require lighter accelerometers to record true acceleration levels without influencing the subject.

Four accelerometer technologies compete to cover most applications: conventional piezo-electric crystals; and MEMS piezo-resistive, capacitive, and piezo-electric.

2.2.1. Conventional Piezo-electric sensors

Conventional accelerometers use an assembly of discrete components to create a system comprising of a proof mass supported by piezo-electric crystal, enclosed within a rigid metal casing¹. When the assembly undergoes an acceleration, the proof mass directly strains the piezo-electric crystal, generating an electrical charge. The piezo-electric crystal may be in tension/compression or shear, dependent on the characteristics required. The charge signal may be amplified within the sensor head, or transmitted through low-loss cables to a remote amplifier. In spite of their size, these devices are suitable for many applications, since they are proven to be rugged and reliable, and have a broad dynamic range, typically from a few Hz to 10kHz or above. However, piezo-electric systems do not offer static-load (or DC) response.

Typical of conventional piezo-electric accelerometers with integral charge amplifiers, are Kistler and Endevco single-axis sensors, with the Endevco 65² three-axis accelerometer representing one of the smallest devices available as a 10mm cube and 5gram mass. Their limiting factor is usually cost, but their accuracy and shock survival are very good.

2.2.2. MEMS Piezo-resistive sensors

In the last 20 years there have been an increasing number of developments in MEMS sensors. These feature primarily micro-machined silicon mechanical components and integrated support electronics³. Early versions used piezo-resistive elements, typically using beams with integral strain-gauges to support the proof mass⁴. These devices are electronically simple, and are generally better able to sense low frequency accelerations than piezo-electric devices, but the beam structures within the package are more fragile. For improved accuracy, resonant devices were made. These measure the change of resonant frequency as the support elements are strained due to applied acceleration. The electronics required for resonant operation are complex, and this technology has been slow to take-off.

The piezo-resistive detection of arm flexure is illustrated by the TAG Electronic Systems accelerometer application notes⁵. Example piezo-resistive devices are the Endevco model 7268-B⁶ tri-axial accelerometer and SensoNor SA50⁷. This device combines three separate sensors in a single package to achieve the three-axis detection. MEMS type piezo-resistive accelerometers require a Wheatstone bridge arrangement to detect the change of resistance of the strained elements. In order to achieve some degree of temperature compensation, the fixed resistors of the bridge are usually included on the same silicon chip as the accelerometer. This gives rise to four wires per axis, which can become the dominant or limiting physical constraint when installing the device.

2.2.3. MEMS Capacitive sensors

Today's technology favours capacitive sensors to create truly integrated and very small accelerometers, typically packaged in surface-mount ICs³. The capacitive sensors can sense using one of two methods: passive sensing, where the proof mass is free to move, and the capacitance is measured between plates, one fixed to the casing and the other attached to a mass supported on beams, as demonstrated by Li⁸; and servo-active sensing, where the charge on the capacitor is driven to maintain a constant gap^{9,10}. The latter method increases linearity and accuracy, but requires complex ASIC's (Application Specific Integrated Circuits) immediately adjacent to the sensor. They offer true static-load response, and work well for navigational purposes, where mathematical integration is used to obtain velocity and position data. Three-axis devices are under development¹¹, but commercial capacitive accelerometers are typically represented by the two-axis Analog Devices ADXL250¹² and single-axis Endevco 7290-A¹³. Capacitive accelerometers are now frequently used in tilt monitoring applications, such as digital inclinometers.

The main advantage is the DC response, which is essential for motion monitoring. To use an accelerometer to measure the position of a slow-moving limb, the selected accelerometer must not produce any zero drift error. A tiny amount of zero drift in the acceleration output results in large velocity or displacement errors after numerical integration. Significant signal processing electronics are required adjacent to, or incorporated into the device, particularly for a digital output. IMI's application notes⁹ (now Analog Devices) show the principle of operation for their capacitive devices with two axes of in-plane motion sensed by comb-type capacitor structures, and configuration for both analogue and digital capacitive accelerometers. An alternative approach is used by VTI Hamlin¹⁴ for a single axis capacitive accelerometer sensing motion in the out of plane direction by using the faces of the proof mass and the casing to creating single plate capacitors. There are alternatives for z-axis detection, as described by Xie and Fedder¹⁵, and a combination of devices on a single chip could be created. To date, no manufacturers have taken this route, and any 3-axis devices currently available rely on precision mounting of two or more chips.

2.2.4. MEMS Piezo-electric sensors

Piezo-electric sensing methods are attractive due to the self-generating nature of the materials, so no direct power requirement for the sensor, and improved resolution compared to capacitive devices. Simple analogue amplification in the sensor head is sufficient to provide a low impedance signal for use in further analysis circuitry. Typical MEMS piezo-electric accelerometers are presented as surface mount devices¹⁶, and these are intended to be embedded within electronic equipment systems. However, in-sensor amplification is also of benefit to minimise cable-noise issues for remote-mounted applications.

Many variations of the piezo-electric MEMS accelerometer have been proposed using different materials, fabrication methods and structures. deReus and Zou use Zinc-Oxide sensor material, in spite of its low piezo-electric coefficients, but they use quite different constructions. de Reus¹⁷ has silicon beams and one axis per sensor, whilst Zou deposits the Zinc Oxide onto Parylene films to form either a highly symmetrical tri-axis sensor¹⁸ or a single-axis cantilever structure¹⁹, specifically aimed at the medical implant market. As deposition methods are being developed, PZT (Lead Zirconate Titanate) materials are now more commonly used, since they have piezo-electric coefficients an order of magnitude higher than Zinc Oxide. Yoon²⁰ is developing a surface micro-machined cantilever device, with metal-organic decomposition (MOD) deposited PZT. Beeby^{21,22} has used thick-film PZT screen-printed onto a multiple beam silicon structure, to create relatively thick bimorph beams of approximately 100µm. And Kunz²³ deposits thin-film PZT from sol-gel onto a slender silicon structure, with beams of around 10µm total thickness.

The only commercial device identified is from MSI¹⁶. This uses PVDF, a piezo-electric polymer to create three individual sensors in a common package, but the finished sensors are highly prone to temperature drift and air-drafts.

Current interest for this Thesis lies with thin film piezo-electric material deposited onto silicon structures, working on the same strain-gauge principle as the piezo-resistive sensors, but using less power since the piezo-electric material generates its own charge signal. This configuration has been neatly demonstrated by Kunz²³.

2.3. Accelerometer Design Theory

From the background of the STAMP project, and considering the current development of different accelerometer technologies, it was decided to develop the MEMS piezo-electric construction further. Capacitive sensors are now commercially available, but are of limited bandwidth, and require significant support electronics, whilst piezo-resistive devices draw higher current than was considered acceptable. This project was intended lead into a commercial product, with good resolution from a small, low-power device.

2.3.1. Proposed Mechanism for a Tri-axial Piezo-electric Accelerometer

The principle of measuring acceleration by flexing of the proof-mass support beams is well documented by vanKampen and Wolfenbuttel²⁴, and Yu and Lan²⁵. This method offers much potential, with the possibility of 3-axis detection from a single proof-mass, although this method was shown to be less than ideal. Both papers compare a number of approaches to MEMS accelerometer design, including cantilever-, and several multiple-supported options. These can be used to derive single or multiple axis readings, dependant upon the mechanical design, and electrical connections. For simplicity of the electrical connections to the sensor, and optimisation of the mechanical signal response, the best results were found using one sensor for each sensitive axis, as described in Chapter 3.3. Both of these references refer back to the work of Roark²⁶ to calculate the

forces and strains in the support beams. The measurement of the flexure of the beams requires a strain-gauge arrangement, and as such applies to both piezo-electric and piezo-resistive detection methods. However, for a single proof-mass device, the out-of plane movement detection signal is not of the same magnitude as the in-plane signal.

2.3.2. Concept Prototypes

The working principle of the accelerometer was described by Scheeper²⁷, then demonstrated by deReus¹⁷ using ZnO (Zinc Oxide) as the piezo-electric material. This tri-axial accelerometer is a set of four identical single-axis devices on a common wafer, including one redundant device. There are simple, permanent electrical connections from each device to separate charge-amplifiers. deReus¹⁷ presents a well developed prototype, but does not appear to have progressed into production at present. Charge output was 0.1pC/g out-of-plane, whilst in-plane the response was 0.01pC/g. These low signals reflect the low d_{31} piezo-electric charge constant value for the Zinc Oxide material used.

Kunz²³ has demonstrated that devices based on van Kampen²⁴ calculations can be fabricated using PZT (Lead Zirconium Titanate), with good correlation between the modelling and fabricated devices. However, the work by Kunz has concentrated on the fabrication of single-mass devices to measure all three axes. Ideally, this requires equal compliance in each direction, which has not been achieved, and compromises the performance in the in-plane axes. For the single proof-mass devices demonstrated, the out-of plane acceleration signal at 22pC/g is three times larger than the in-plane signals of 8pC/g. These signals are two orders of magnitude stronger than deReus, due to the use of PZT. Measurement is achieved using a bench-mounted charge amplifier, but sensitivity in each direction requires different connection of the piezo-electric segments. In the demonstrations, only one direction is actually measured at a time. The single proof-mass design by Kunz²³ does not appear to have progressed beyond the laboratory prototype stage at present.

2.3.3. Multi-layer Beam structures

As the theoretical model was developed, the level of detail required became apparent. The structure of the proposed accelerometer structure (as outlined by Kunz²³) uses thin silicon beams, with thin-film PZT sensors. The PZT sensor material and electrodes contribute significantly to the stiffness of the beams. The works by Wienberg²⁸ and Smits and Choi²⁹ elaborate the detail of multi-layer beams to calculate the beam stiffness with greater accuracy. The thin film piezo-electric elements on silicon beams create a structure with a minimum of five layers, as illustrated in Figure 2-1. This 'sandwich' constitutes silicon, silicon oxide, platinum, PZT, and further platinum. The material properties and thickness of each layer vary significantly; so proper consideration of the beam structure is required in the model.

2.3.4. Material Properties

Single crystal silicon is a standard material for the manufacture of electronic, and many MEMS devices. The crystal lattice gives a pronounced an-isotropic behaviour to this material, which affects both the shape formed by wet chemical etching; and the material strength.

The understanding of material data for single crystal silicon has proven difficult, and been the subject of much research³⁰. The material properties change significantly dependant on the crystal orientation, leading to a wide variation in values quoted. In many cases, the orientation for measurement is not stated. However, the influence of anisotropy is explained by Spiering³¹, and Figure 2-2 confirms the values for <110> orientation silicon that have been used.

Youngs Modulus $E = 169 \times 10^9 \text{ N/m}^2$ and Poisson's Ratio $\nu = 0.0625$

Sourcing accurate material properties for thin-film PZT also proved difficult, due to the range of compositions available. The data available is almost exclusively for bulk materials, and this is presented by trade reference rather than composition. Sol-gel deposited thin-films are referred to by the chemical composition, and are difficult to characterise, since conventional methods cannot be applied. However, a number of experimental techniques are being used to evaluate thin film PZT: 53% Zirconate/ 47% Titanate composition by Gardiniers³² of Enschede, 30% Zirconate/ 70% Titanate composition by Huang³³ at Cranfield, and 52% Zirconate/ 48% Titanate composition by Shepard³⁴ in Pennsylvania. For the initial stages of modelling, it was decided to use the material data for 52% Zr / 48% Ti PZT, quoted by Yu and Lan²⁵, since thin-film PZT data such as that quoted by Inostek³⁵ was incomplete. However, further investigation has produced the work by Kim^{36,37}, which is based on the research at Inostek, giving a more complete data source. Improved understanding of the piezo-electric properties has also aided interpretation of the available data. The work by Jaffe³⁸ provided an invaluable background, based on the properties of bulk PZT, but explaining the phase diagram, and the implications on material behaviour.

The use of 52/48 composition PZT is desirable, since the piezo-electric response is higher than for 30/70 composition PZT. However, for the development of physical prototypes, only 30/70 composition PZT was available through an established deposition process. The change of composition affects the level of charge generation, but has minimal affect on the behaviour of the mechanical system. All modelling work used the 52/48 composition PZT material properties (which exhibits approximately three-times higher d_{31} charge output coefficient than 30/70 composition), and it was accepted that the practical findings would be at approximately $\frac{1}{3}$ of the theoretical charge output values.

2.4. Patents

There are many areas of intellectual property related to this project which could be the subject of patents. A patent search has been carried out, based on known manufacturers, or European Patent Classification class G01P15/09D (bending or flexing type piezo-electric accelerometers). This has revealed a variety of related process and design features that have already been patented, including but not limited to :-

US 6252335 - 2001	Pacesetter - Beam-type Accelerometer
EP 0981754 - 2001	Kionix - Trench isolation for micro-mechanical devices
EP 1085325 - 2001	NGK Insulators - Acceleration sensor element, acceleration sensor & method of manufacturing the same
US 6105225 - 2000	Matsushita - Method of manufacturing a thin film sensor element
US 6043588 - 2000	Murata Manuf. - Piezoelectric sensor and acceleration sensor
US 6023972 - 2000	Allied Signal - Micro-machined rate & acceleration sensor
US 5911738 - 1999	Medtronic High output sensor & accelerometer implantable medical device
EP 0869367 - 1998	NGK Insulator - Three-axis sensor
EP 0667532 - 1995	Matsushita - Thin film sensor element & method of manufacturing the same

Of these, the US patents listed are only registered in the USA, and any European product should not be limited by their content.

The patents found originate predominantly from Japan or the USA. None appear to be showing the proposed STAMP device, or concepts therein. However, there are useful pointers for potential pitfalls in the design, and expected performance from piezo-electric MEMS accelerometers. Medtronic refer to the specialist application of accelerometers in conjunction with cardiac pacemakers, in order to regulate heart rate in response to physical activity, and other implanted pulse generators. Kionix offer an enhancement to Deep Reactive Ion Etching (DRIE), intended to aid in the manufacture of capacitive sensors. Whilst Matsushita describe methods of creating thin-film titanate lead zirconate (PZT) piezo-electric sensor elements, but use the PZT as a self exciting proof mass. This is of interest regarding the manufacturing methods, but not in conflict with the STAMP accelerometer, which is of beam construction.

2.5. Related Standards for Accelerometer Applications

As the accelerometer is intended to be a commercial device, it is important to consider the applications and restrictions on its usage. For example, if insufficient bandwidth is achieved, certain markets will be barred, since the sensor cannot meet the requirements of the test specifications. Related Standards include:

- o Hand Arm Vibration – BS 7482 (1991) (Instrumentation Spec), ISO 5349 (2001),
- o Whole Body Vibration – BS 6841 (1987), ISO 2631 (2001), ISO 10056 (2001), ISO 13090 (1998), EN 14253 (Draft 01/713276 DC)
- o Ambulatory Study – Proposals available from the International Society of Biomechanics, BS 3375 (1997) (Time and Motion Analysis at Work)
- o Ground and Building Vibration – BS 4142 (1997)(Industrial / Residential Noise), BS 5228 (1997) (Construction Sites), BS 6611 (1985) (0.063-1Hz), BS 6472 (1992) & ISO 2631 (2001) (1-80Hz)

Within these specifications, there are definitions of the scope of each application, which influences the performance requirements of the STAMP accelerometer. As can be seen, ISO 2631 is applicable to both Whole Body Vibration and Ground and Building Vibration, and there is overlap in the requirements between applications. Of the specifications listed, BS 6611 presents the most challenging requirement to include within the working range of a piezo-electric accelerometer, with very low frequency ground vibrations (0.063 to 1Hz). It is suggested that this range could not be included.

2.6. Conclusions

All of the building blocks are in place to create models and physical prototypes for a piezo-electric accelerometer. Whilst much research has been undertaken, no-one has ventured to develop a production three-axis piezo-electric MEMS accelerometer, based on the flexing of beams. This work is focussed on improving the understanding of the mechanism, its abilities and limitations, with the purpose of achieving this manufacturing goal.

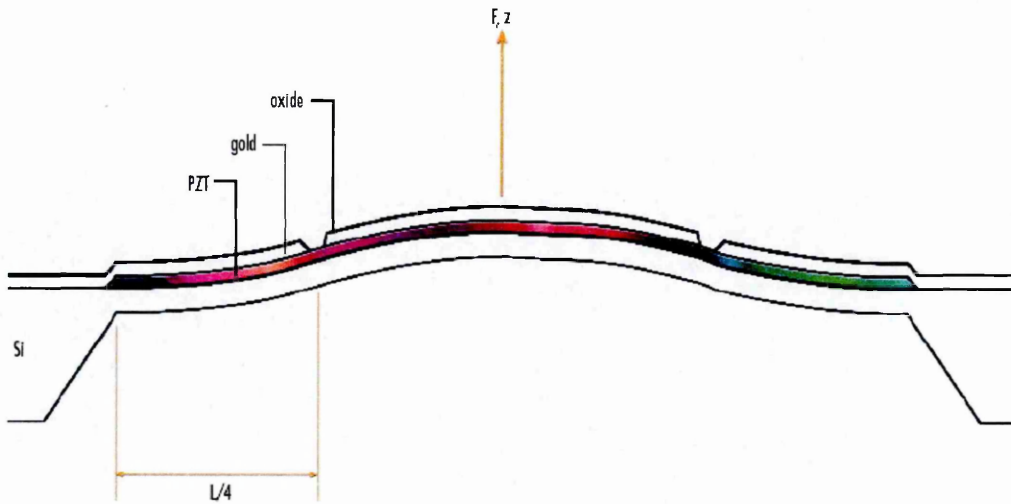


Figure 2-1 Typical construction of a beam with PZT sensors²⁸

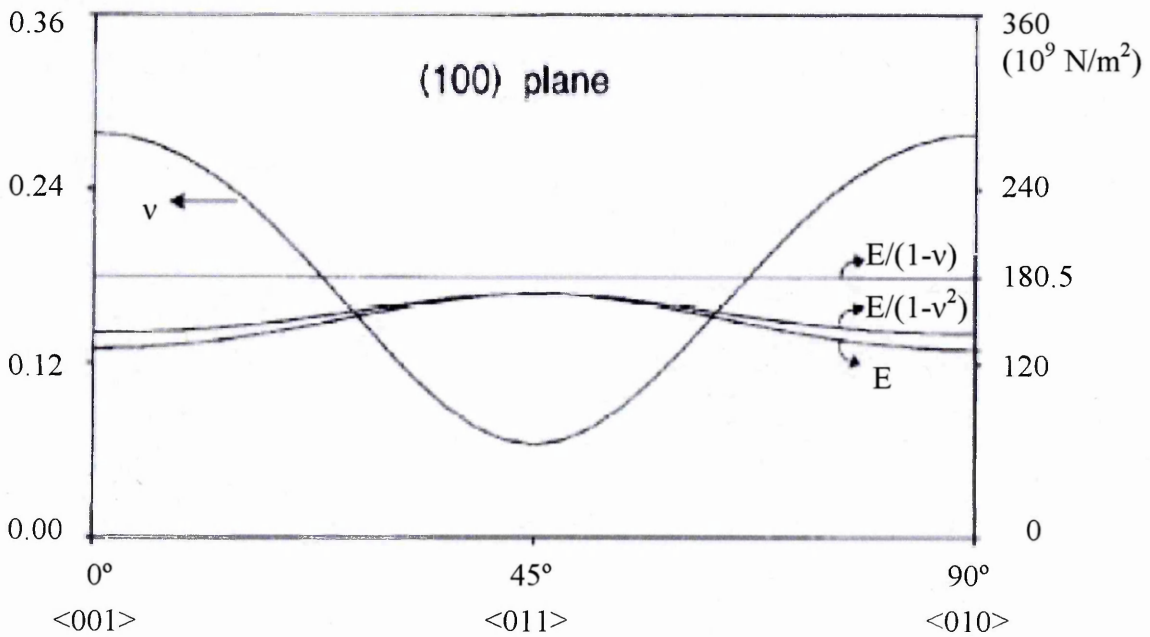


Figure 2-2 Variation in silicon properties with orientation to the crystal lattice
Young's Modulus 'E', Poisson's Ratio 'v' and ratios $E/(1-v)$ and $E/(1-v^2)$ ³¹

3. Theory and Modelling - Mathematical models

3.1. Purpose for the mathematical models

It was proposed to develop the STAMP accelerometer as a set of three single-axis devices on a common wafer, in order to optimise the design of each device, whilst maintaining alignment. The work by deReus¹⁷ shows that a single sensor design gives typically an order of magnitude greater response in the out of plane direction. It was proposed that the devices would be based on a mass supported by two or more beams. By using two designs of sensor, to cope with in-plane and out-of-plane signals, matching the signal strength sensitivity (mV/g) should be possible. The cross-axis sensitivity should be improved, and on-device electrical connections would be simplified. Figure 3-1 shows a typical layout for the proposed accelerometer. Two identical devices are used to sense the X and Y directions (in-plane), and a different configuration is used for the out of plane Z-axis. The performance range of the z-axis may differ from x- and y-axes due to the mode of operation. This would not be the first time that an accelerometer has exhibited different characteristics between axes².

3.2. Construction of the models

A separate mathematical model was developed for each device configuration, using MathCAD software. The models were parameterised in order to optimise the key features for each configuration of accelerometer, and to identify the behaviour of the device in response to changes in any of the variables. The need for separate models was due to the different arrangement of beams in each case, and differences in the way that each beam is deformed when a given acceleration is applied. A single model to cover all of the designs was considered unwieldy, since it would require numerous 'zero' values to eliminate the unused features, but there is commonality between models wherever possible. A typical MathCAD model for a single axis MEMS accelerometer is shown in Appendix 1.1.

The mathematical models are used to identify trends in the expected behaviour of the accelerometer structure, based on geometrical changes. Whilst measures have been included to improve the accuracy of the models, they only consider linear-static load

cases, and do not include damping. These significant simplifications limit the credibility of the results.

It is proposed that the three-axis accelerometer design will consist of piezo-electric sensor elements deposited onto a set of three micro-fabricated structures, on a common silicon wafer. This is shown schematically in Figure 3-1.

The models developed were required to include piezo-electric strain to charge calculations to determine the electrical output in response to a range of acceleration forces.

From the specification in Table 1-1, key design characteristics were identified as:

- the minimum resonant frequency to be greater than 5kHz (to retain a linear response even with a heavily damped structure).
- the amplitude of movement of the proof mass in response to a given acceleration of the frame.
- to maximise the magnitude of the piezo-electric charge signal that would be generated in response to a given acceleration in the sensitive direction, 5pC/g is desired.
- to minimise the magnitude of the piezo-electric charge signal that would be generated in response to a given acceleration not in the sensitive direction (cross-axis sensitivity).
- and the device footprint area to be less than 5mm by 10mm.

From these key sensor characteristics, secondary performance characteristics can be interpreted. For example, the signal resolution performance is calculated from the signal to noise ratio. This may be affected by cross-axis sensitivity, or dominated by the electrical noise from the amplifier, and it is a goal of this project to quantify these noise sources.

Noise sources were considered, and fall into electrical and mechanical categories. The mechanical noise sources include the effect of air molecules colliding with the proof mass, but when these effects were evaluated they were found to be well below the resolution of the sensor. Similarly, with relatively large clearances around the proof mass, thin film damping could also be neglected throughout the working frequency range. However, it should be noted that at high frequencies (above 10kHz), the air damping of the proof mass becomes beneficial since it helps to support the proof mass. The main noise sources are predicted to be from the electronics, particularly Johnson (thermal) noise from the high value resistors in the circuit, and electrical interference pick-up, if there is insufficient screening. The electrical considerations were discussed by Paul Towers in his proposal for the charge amplifier design.

3.3. Selection of Modelling Configurations

A number of alternative arrangements for a three-axis MEMS accelerometer have been investigated. All options are based on three separate MEMS fabricated proof masses, each supported in the frame by multiple-beams. The whole device is etched from a single silicon wafer. All beams are on one surface of the wafer, and there is some degree of symmetry for each individual mass in order to achieve selectivity for cross-axis isolation. The creation of equal but opposite charge allows the device to be configured such that the charges generated by accelerations not in the chosen axial direction will cancel each other out. The movement of the mass in response to acceleration would be detected by thin film piezo-electric sensors directly measuring the surface strain of the support beams. For each design, the models are used to calculate the resonant frequency (to estimate the working frequency range) and bending moments, surface strain, and charge generated (to obtain the sensitivity of the device). In each MathCAD model, checking calculations are in place for in-plane stiffness of the beams (to ensure that the mode of deformation is predominantly out of plane, as modelled), mechanical amplitude of motion (to comply with the signal amplitude linearity requirements) and the capacitance of the sensors (to allow calculation of voltage output instead of charge).

In all the designs considered, out-of-plane accelerations are measured by a translation of the mass, with all beams deforming equally, as shown in Figure 3-2, whilst in-plane accelerations cause a rotation of the mass about one of its axes, as shown in Figure 3-3. For in-plane measurement, the centre-of-mass is offset from the beams, and lateral acceleration causes equal but opposite deflection of the beams located along the axis of movement. The dimensions of the device are such that the beams are relatively thin, and out-of plane stiffness is much lower than in-plane (sheet) stiffness.

Cross-axis noise can be generated on the in-plane signals by rotation of the sensor. These signals are indistinguishable from linear acceleration, but these can usually be accepted as part of the signal noise, since they are either of short duration or of low magnitude. The out of plane sensor should cancel-out any rotation-induced signals, if there is sufficiently accurate symmetry of the manufactured sensor die. The effect of misalignment of the electrodes is analysed using the Finite Element models in Chapter 4.6.

There are a number of options on the arrangement of the beams to support each mass, and the types of device required to achieve three-axis detection. The final accelerometer designs would be a combination of the devices suggested below, selected and sized in order to achieve the best overall performance within the available space. Either two or three proof-masses would be required, dependent on the designs selected.

For each of the possible configurations listed below, the measurement sensitivity, mechanical-thermal noise, cross-axis sensitivity, and natural frequencies were investigated by mathematical modelling. The shape of the proof mass was considered,

with the options being wet or dry etching techniques. These produce truncated pyramid or parallel-sided proof-masses respectively.

3.3.1. Single Axis, Semi-symmetrical Devices

The accelerometer described by de Reus¹⁷ is a combination of three identical single axis devices, each using two-beams to support the mass, as shown in Figure 3-5. This design presents the simplest configuration for electrical connections, however it can be improved if each axis uses an optimised device. Figure 3-5 shows an x-direction accelerometer. Acceleration in the y-direction would cause a rotation about the centreline of the beams, and hence the generated charge would cancel-out across the width of each piezo-electric element. Acceleration in the z-direction would deform the beams symmetrically, causing a similar self-cancellation of the charge generated.

The semi-symmetrical device is designed for use in either the y- or z-axis directions. Figure 3-6 shows the layout of a typical device, and how the notation is applied. The requirement for symmetry is limited to x- and y-axis only. All beams are of the same dimensions, and symmetrically positioned along opposite sides of the proof mass. Mathematically, one continuous beam on each side can be modelled as two separate beams with no gap between them. The shape of the mass and the spacing of the beams can be varied to optimise performance for the chosen axis.

The deformation of the beams is different for acceleration in each of the axial directions. Accelerations in the y- direction corresponds with Figure 3-3 and z-axis accelerations have the effect illustrated in Figure 3-2. Sensing of y-axis acceleration is not impeded by the deformation of side beams in torsion. However, x-axis acceleration causes a combination of torsion and displacement, illustrated in Figure 3-4. This is described in more detail in section 3.4.1. The torsional deformation of the beams results in the surface strain varying over the width and length of each beam, although the predicted level of charge generation tends to be comparable to y-axis sensing.

The piezo-electric sensor electrodes are patterned to suit the y- or z-axis, in accordance with section 3.5.4. All beams supporting the mass would be used to sense acceleration in the same axis, so a separate device is required for each axis. The x-axis sensor would be identical to the y-axis, but rotated through 90°.

Inset Beams

If the beams are inset into the proof mass (Figure 3-7), then for a given mass value and beam dimensions, the z-axis response will be fixed. However, as the distance from the end of the beams to the centre of the proof mass decreases, the distribution of the mass moves out (increasing the second moment of inertia) and the leverage of an in-plane acceleration to displace the beams increases.

Inset beams are incorporated into the model using the method of defining x dimensions as a stepped function of the y distance from the pivot. For fixed values of a_x and a_I , the

mass is increased by increasing dimension a_y . There is a disproportionate increase in the moments of inertia for rotation about the x- and y-axes, where the x-axis gains little inertia, since the additional mass is concentrated towards the axis of rotation, whilst the y-axis gains a significant amount of inertia, since all the additional mass is further from the pivot.

3.3.2. Two Axis, Highly Symmetrical Devices

The second option is to use two highly symmetrical devices. The first device would be measuring x- and y-axis, with equal response on each, and the second device would be optimised for the z-axis. From initial investigation, the z-axis device is likely to be smaller, in order to match the response achieved on the other axes. The highly symmetrical device has been demonstrated in laboratory trials as a single-mass tri-axial accelerometers by Kunz²³ (Figure 3-8). The single mass device uses different summations of the charge signals to detect x- and y- or z-axis accelerations, so requires either switched connections or eight individual charge amplifiers, but either option significantly increases the complexity of the sensor electronics. It was decided to consider the use of two similar devices, each with permanent connections to the appropriate axis charge amplifiers.

The mathematical model of this device uses a square mass with identical beams in the centre of each side (Figure 3-9). There is a high degree of symmetry, about both x- and y- axes, the diagonal axes, and by rotation through multiples of 90°. It can be used to sense accelerations in the x- and y-axes simultaneously.

Acceleration in the direction of the x- or y-axis causes a combination of lateral and angular displacement of two beams (Figure 3-3), and torsion in the other two beams. The piezo-electric sensor electrodes are patterned identically on each beam, with the pattern optimised according to section 3.5.4, for charge generation when the acceleration is applied along the length of the beam. The acceleration is detected by sensors on the beams in-line with the appropriate axis, using the inner electrode on each beam connected to the outer electrode on the opposite beam. X-y cross-axis sensitivity is low, since the torsion in the other pair of beams should not generate any net output charge.

Z-axis acceleration gives equal lateral displacement of all four beams, since they have equal stiffness, and are evenly distributed (Figure 3-2). To maximise the charge signal, the sensor electrodes should be of equal size on either end of each beam, with the four inner electrodes connected, and the four outer electrodes connected. Cross-axis sensitivity to x- and y-axis accelerations is taken as self-cancelling, since the piezo-electric sensors of each beam undergo the same magnitude but opposite sense of strain to the sensor in the diametrically opposite position. The same principle of isolation also holds true for cross-sensitivity in the x- or y-axis due to z-axis accelerations.

Inset Beams

If the beams are inset into the proof mass (Figure 3-10), then similar advantages are gained to the semi-symmetrical design. As the distance from the end of the beams to the centre of the proof mass decreases, the distribution of the mass moves out to the corners (increasing the second moment of inertia) and the leverage of an in-plane acceleration to displace the beams increases.

In the mathematical model, this is incorporated by defining the shape of the proof mass with x as a stepped function of y , then integrating to find the mass and moments of inertia. This model is shown in Appendix 1.1, as an example of how the models are constructed.

3.3.3. Rotationally Symmetrical Devices

A modification to the highly symmetrical device is to offset the beams to the corners of the mass, as shown in Figure 3-11. If the beams are deformed by an applied acceleration, either the ends of any beam move towards each other or the true length of that beam is increased, as discussed in section 3.4.3. Due to the symmetry of the devices modelled in sections 3.3.1 and 3.3.2, the beams are in-line, and the length of the beams cannot foreshorten as they undergo deformation. This is exaggerated for in-plane accelerations, since the proof mass also rotates out of plane, and therefore becomes foreshortened (Figure 3-3). This puts additional axial strain on the beams.

By the use of offset beams, the rotationally symmetrical design allows the proof mass to rotate about the z -axis. Where all beams are equally loaded (z -axis acceleration) they all pull in the same direction, and the proof mass can rotate, in preference to incurring axial strain on the beams. Where the beams are un-evenly loaded (acceleration in-plane), the proof mass will rotate to achieve a balance of strain in all beams, reducing any extreme values. The stable condition is when zero average strain is achieved, with some beams in compression and some in tension. By reducing the axial strain, the working range of displacements is increased for the specified 3% non-linearity.

3.3.4. Novel, Multi-beam Devices

The semi-symmetrical device can also be modified by supporting the 'free' ends onto the frame (Figure 3-12). The extra beam either end should be short but slender, in order to act as a y -axis pivot, and symmetry about the x - and y -axes must be maintained. The beam thickness is dictated by the wafer manufacturing method, and therefore must be the same as the main support and sensing beams. Due to the short length, the end support beams are relatively stiff for out of plane movements, and can virtually eliminate x - or z -axis movements, whilst incurring low rotational stiffness about the x -axis. Rotational stiffness would reduce the sensitivity in the y -axis, as noted in section 3.3.2, so a low value is desirable. The limitation of this concept is that the end beams are highly stressed by x - and z -axis accelerations, and the fracture strength of silicon

becomes important. The mathematical model calculates the fracture strength of the end support beams to ensure that the device can withstand shock-loads of 1,000g.

In order to reduce cross-axis sensitivity, a single central beam for sensing (as shown in Figure 3-12) would minimise the charge generated by x-axis accelerations, compared to using two sensing beams on each side. Using one beam each side would also reduce the number of interconnecting tracks between sensor electrodes, compared to using four sensing beams. The piezo-electric sensor electrode patterning would be optimised according to section 3.5.4 for acceleration along the length of the beams.

3.4. Derivation of the Mathematical Models

Each mathematical model starts by defining which configuration of device is being studied, then illustrating how the notation is applied. The dimension variables and material properties are defined, and from this information, the mass, position of the centre of mass, second moments of inertia, and stiffness for displacements in the x-, y- and z-axis directions are calculated. This allows the resonant frequency to be calculated for each axis, using Equation 3-1. It is desirable that resonance is not encountered within the working frequency range of the accelerometer, but that the first resonance should be in the desired sensitive direction. To achieve 5% linearity over the working frequency range (from Table 1-1), the first resonance should be at a frequency of approximately three times the maximum working frequency.

$$Frequency = \frac{1}{2\pi} \sqrt{\frac{Stiffness}{Inertia}}$$

Equation 3-1

For acceleration out of plane, where the proof mass travels in a linear direction, the resolved units are $[Hz] = \sqrt{\frac{[N/m]}{[kg]}}$ and for in-plane accelerations, where the proof mass rotates about the orthogonal in-plane axis $[Hz] = \sqrt{\frac{[N.m/rad]}{[kg.m^2]}}$

vanKampen²⁴ assumed that any acceleration will cause an out-of-plane deformation of the beams. Since the mass is not in the plane of the beams, it is assumed that an in-plane acceleration would cause the mass to rotate about an axis through the plane of the beams. The in-plane stiffness of the beams has been calculated, and is typically 1000 times higher than the out-of-plane stiffness, verifying that this is a reasonable assumption to make.

3.4.1. Strain in the Beams

In the designs proposed, the strain in the surface of the beam will be converted to charge by piezo-electric sensors on the surface of the beams. The charge generated in the piezo-electric sensors is proportional to the stress in the piezo-electric material. If the piezo-electric sensor is thin compared to the beam, the surface strain of the beam is used to calculate the stress in the piezo-electric material, as demonstrated by Yu²⁵. If the piezo-electric material forms a significant portion of the beam thickness, then the properties of a composite beam must be considered, as described by Smits²⁹ and Weinberg²⁸. This is considered in section 3.4.4.

The surface strain of each beam can be calculated from the bending moments (curvature) in the beam, as explained by Roark²⁶. There are three distinct load cases generated by different device geometries, and these are now considered.

- The simplest case is a z-axis acceleration causing displacement of the proof mass perpendicular to the plane of the beams (Figure 3-2). All beams undergo equal deflection, the surface of the proof mass remains parallel to the frame, so each beam forms a symmetrical 'S'-bend. Since all constraints are applied at the ends of the beams, the bending moment varies linearly from one end of the beam to the other, passing through zero at the centre of the length of each beam, as defined in Equation 3-2. There is no variation across the width of the beam.

$$M_1(x) = W_1 \frac{L}{2} - W_1 \cdot x \quad [\text{N.m}]$$

Equation 3-2

where $M_1(x)$ is the moment at distance x along the beam from the proof mass end
 W_1 is the force applied $W_1 = \text{Mass} \times \text{Acceleration}$ L is the length of the beam

- The second case is when acceleration is applied in-plane in the direction of the length of the beams. The centre of mass is offset from the plane of the beams, and the proof mass will roll about an axis parallel to the ends of the beams. The beams are deflected by equal but opposite distances out of plane, and also undergo an angular displacement out of plane at the proof mass end (Figure 3-3). The constraints are again confined to the ends of the beams, so the bending moment varies linearly from one end to the other, with the moment due to the angular displacement superimposed on top of the moment applied by the displacement. In Equation 3-3 it can be seen that the first two terms are identical to Equation 3-2, the components due to out of plane displacement, and the last two terms are due to the angular displacement. The moment due to the angular displacement decreases linearly through zero at two thirds of the length of the beam, so the point of zero bending moment occurs closer to the frame end of the beam. The exact position is dependant on the relative dominance of out of plane and angular displacement, governed by the length of the beam and the distance from the

end of the beam to the axis of rotation. Again, there is no variation across the width of the beam.

$$M_2(x) = W_2 \frac{L}{2} - W_2 \cdot x + W_2 \frac{L^2}{3 \cdot a} - W_2 \frac{L}{2 \cdot a} x \quad [\text{N.m}]$$

Equation 3-3

where $M_2(x)$ is the moment at distance x along the beam from the proof mass end
 L is the length of the beam W_2 is the force applied
 a is the distance from the point of rotation to the end of the beam

$$W_2 = \frac{\text{Mass} \times \text{Acceleration} \times 3 \cdot Z_c \cdot a}{L^2 + 3 \cdot a \cdot L + 3 \cdot a^2}$$

Z_c is the distance from the point of rotation to the centre of mass

- The third case is when in-plane acceleration is applied perpendicular to the length of the beams. The proof mass rotates about an axis parallel to the length of the beams, and the beams undergo a combination of displacement and torsion. The bending moments associated with the displacement can be approximated by considering a series of narrow strips along the length of the beam, the ends of each strip remaining virtually parallel, but the displacement changing across the width of the beam. Integration over the width of the beam shows a linear increase in deflection with distance from the point of rotation. This equates to the entire width of the beam being deflected by the average displacement, and Equation 3-2 can be used.

Using the integral of displacement theory across the beam is reasonable, providing that there are two beams per side, and the beams are distant from the axis of rotation. In this case displacement is the dominant factor. When the axis of rotation passes through the beam, torsion is the dominant component of the stiffness. This causes shear forces within the beam, and the surface strain is no longer adequately calculated from the bending moments used in the displacement theory. In this situation, the charge is usually an unwanted component of cross-axis sensitivity, and it is desirable for symmetry to make the charge generated self-cancelling.

3.4.2. Generating Charge from Strain

Dependant upon the geometry of the device and the direction of the applied acceleration, the beams undergo one or more of the bending moment load-cases described above. This causes a pattern of surface strain on each beam, corresponding to the internal moments. If only the silicon layer of the beam is being considered to influence the stiffness of the beam, the neutral axis (points of zero strain) is considered to be at the mid-point of the beam thickness, and the surface strain is defined by Equation 3-4.

$$\sigma = M(x) \frac{d}{2EI}$$

Equation 3-4

where σ is the surface strain on the beam
 I is the second moment of inertia of the beam
 E is the Young's Modulus of the beam (silicon)
 d is the thickness of the beam.

The charge generated is proportional to the strain in the piezo-electric material, and for simplicity it is assumed that the strain in the piezo-electric material is the same as the surface strain in the beam. By integrating the surface strain over the area of the beam covered by a piezo-electric sensor, then multiplying by the Young's Modulus and dielectric constant, the charge generated by that sensor can be calculated (Equation 3-5). This is an instantaneous value at the moment the load is applied, and will decay away due to leakage currents through the PZT material and into the amplifier circuit.

$$Q = d_{31} \cdot c_{11} \iint_{Area} \sigma dx \cdot dy$$

Equation 3-5

where Q is the charge generated
 c_{11} is the Young's Modulus of the piezo-electric material
 d_{31} is the piezo-electric charge constant for charge orthogonal to applied strain
 $Area$ is the area of the sensor covering the beam surface

Each beam is deformed into an 'S'-bend by the applied acceleration. This generates separate regions of compressive and tensile surface strain on the beam, and these should each be detected by separate piezo-electric sensors. By selecting to calculate the sum or difference of the charge generated by a combination of piezo-electric sensors, the device can show sensitivity to acceleration in one axial direction in preference to another, and the charge sensitivity to acceleration in the chosen axial direction can be calculated.

The charge sensitivity can be converted to an idealised voltage signal amplitude by using the capacitance of the sensor. The capacitance of the piezo-electric sensor can be calculated using the electrode area, dielectric properties and thickness of the piezo-electric material. Voltage values derived are the maximum that could be achieved, and will be reduced by additional electrical loads such as amplifiers connected to the sensor.

3.4.3. Non-linearity of Beam Deformations

If the beams are deformed by an applied acceleration, either the ends of the beam move towards each other or the true length of the beam must increase. In the models considered here, the ends of the beams are constrained, so a lateral deformation causes

an axial tensile strain. The affect of axial restraint on displacement is defined in 'Beams restrained against horizontal displacement at their ends' [Roark²⁶, Table 12], as shown in Equation 3-6.

$$y_{\max} + \frac{A}{16I} y_{\max}^3 = \frac{4WL^3}{\pi^4 EI}$$

Equation 3-6

where y_{\max} is the deflection of the proof mass with beam ends constrained

W is the force applied $W = \text{Mass} \times \text{Acceleration}$

A is the cross sectional area of the beam $A = b \cdot d$

I is the second moment of area of the beam $I = b \cdot d^3 / 12$

This represents two beams of length L in-line, with the proof mass between them (the z-axis load case). This is a special case where the axial load is self imposed, but Roark has produced a table of 'Reaction and deflection coefficients for beams under simultaneous axial and transverse loading' [Roark²⁶, Table 9] that is applicable to any load-case. From this, it can be seen that for a given axial tension in a beam, the maximum effect is the reduction in lateral displacement of the beam, whilst angular deflection and bending moments are reduced to a lesser extent.

It is intended to maintain the working range of the accelerometer within 3% of the linear value. Since we have Equation 3-6, we can resolve the deflection of a beam with axial restraint, but equivalent formulae are not available for angular deflection or bending moments. If we compare the lateral deflection with and without axial strain, and maintain less than 3% non-linearity, then the angular displacement and bending moments will also be within 3%. The charge generated is proportional to the bending moments, so it will also be within the desired linearity.

For a z-axis acceleration applied to a mass supported by a pair of beams free to move along their length this is defined by Equation 3-7 [Roark²⁶, Table 3].

$$y_{\text{theory}} = \frac{1}{2} \cdot \frac{WL^3}{12EI}$$

Equation 3-7

where y_{theory} is the deflection of the proof mass with free beam ends

The limiting case is when $y_{\text{theory}} = 1.03 y_{\max}$. If we use this to equate Equation 3-6 and Equation 3-7, we get Equation 3-8.

$$\frac{\pi^4}{4} \left(y_{\max} + \frac{A}{16I} y_{\max}^3 \right) = 24 \times 1.03 y_{\max}$$

Equation 3-8

By using the definitions of area (A) and the second moment of area (I), Equation 3-8 can be reduced to Equation 3-9, which calculates as $y_{\max} = 0.15 d$, where d is the thickness of the beam.

$$y_{\max}^2 = \left(\left(24 \times 1.03 \times \frac{4}{\pi^4} \right) - 1 \right) \frac{16}{12} d^2$$

Equation 3-9

Therefore, if acceleration of 50g in the z-axis causes a deflection of 15% of the beam thickness or less, the charge generated by acceleration within the working range of the device will be within 3% of the linear value calculated. In the MathCAD models, beam deflections and bending moments are calculated using theory without axial constraints, such as Equation 3-7. There is a check to ensure that deflection caused by the 50g maximum acceleration is less than 15% of the beam thickness, and if this is true the linearity of the model is considered acceptable.

3.4.4. Effect of the Piezo-electric Sensor on Beam Stiffness

In section 3.4.1, the strain in the piezo-electric material was approximated by the surface strain of the silicon beams. For the devices proposed, the 1-micron thick piezo-electric film represents approximately 10% of the total beam thickness. The model in Appendix 1.3 was developed using the method described by Weinberg²⁸. Using this model, it can be shown how the composite beam structure affects the stiffness of the beams. With the piezo-electric film, electrodes, and the buried oxide layer not etched from the back of the beams, the second moment of inertia of the beam structure increases from $85 \times 10^{-9} \text{m}^4$ (for the bare silicon beam, assumed in the simple model) to $144 \times 10^{-9} \text{m}^4$. The surface strain of the bare silicon beam was found to be 145% of the mid-material strain for the piezo-electric film of the composite beam.

This example demonstrates the importance of modelling the sensor layers, since they increase the stiffness of the beam, and reduce the strain in the PZT. The variance values calculated above are true for all models that use the beam thickness and construction described, and reduce if the beam thickness is increased. It was decided to run initial models without including the composite beam structure, and to only add the composite beam structure detail to those models that warranted further investigation.

Where the composite beam structure is modelled, the bending moments in the beams must be based on the second moment of area (I) for the composite beam, and the strain in the thin film piezo-electric sensor is taken as the value at the mid-material thickness.

The strain calculation in Equation 3-4 must be modified using the distance from the neutral axis to the centre of the piezo-electric layer instead of half the beam thickness ($d/2$).

3.5. Generic Features Affecting the Design

There are a number of common features that will affect the performance of any beam / mass device. These are the etching method (affecting the shape of the proof mass), wafer thickness, beam thickness, and electrode patterning (affecting the amount of available charge being collected).

3.5.1. Etching Method

Comparison of wet etched (KOH) and DRIE proof masses was investigated. The wet etched mass was considered as a simple truncated square pyramid, with sides inclined at 54.7° but ignoring any corner effects, whilst the DRIE mass was modelled as a cubic shape. The mass, position of the centre of mass, and second moments of inertia were calculated for each shape.

The shape of the proof mass affects the mass and second moments of inertia of the mass. These are calculated by defining the x and y dimensions as functions of z , the distance through the wafer, then integrating over the volume of the mass.

In the range of dimensions expected for the three axis accelerometer, the wafer thickness is of the same order of magnitude as the length of side of the proof mass. Using the same area of wafer, the models showed that due to the increased mass, and the increased distance from the plane of the beams to the centre of mass, the DRIE fabricated device could generate approximately double the charge output for an in-plane acceleration compared to a wet etched mass.

If the in-plane dimensions of the proof mass are reduced to square-root-of-two times the wafer thickness, the sides of the wet etched truncated pyramid converge. Below this dimension, the feature is reduced to a 'V'-shape in cross section, and the depth of the 'V' is the in-plane dimension divided by square-root-of-two. If the proof mass is more complex than a square or rectangular shape, many dimensions fall below square-root-of-two times the wafer thickness. The effects of wet etching generally render complex designs un-useable, since the centre of mass is too close to the plane of the beams, and only DRIE etching was used to model the geometries of the devices described in the following sections.

3.5.2. Wafer Thickness

The affect of wafer thickness on resonant frequency and charge generation was investigated. The equation for resonant frequency (Equation 3-1) is key to the design of the accelerometer, since it combines all the dimensions of the beams and proof mass. Equation 3-10 shows z -axis stiffness and inertial mass values entered into the resonant

frequency equation. For a 5kHz resonant frequency, if the geometry of the device is fixed except for the wafer thickness and the beam width, then the beam width varies linearly with the wafer thickness and hence the mass.

$$Frequency = \frac{1}{2\pi} \sqrt{\frac{4E \cdot b \cdot d^3 / L^3}{\iiint \rho dx dy dz}} \propto \sqrt{\frac{b \cdot d^3 / L^3}{tw}}$$

Equation 3-10

where tw is the wafer thickness
 b is the width of the beam
 d is the thickness of the beam
 L is the length of the beam

As the mass increases, the stiffness increases proportionately, so the moments along the length of the beam are unchanged. Since the charge generated is proportional to the area of the beam, and the moments are constant across the width of the beam, then by increasing the width of the beam, the charge generated will increase accordingly. Z-axis charge generation is linearly proportional to wafer thickness and beam width.

When sensing in-plane accelerations applied along the length of the beam (case 2 in section 3.4.1), the resonant frequency equation is defined by Equation 3-11. The stiffness is now dependant on the length and position of the beams (L, a), and the second moment of inertia is dependant on the distribution of the mass (a, tw). The thicker wafer has a greater mechanical advantage to displace the beams, as well as the increased mass, and the in-plane charge signal generated increases in line with the wafer thickness squared. Figure 3-13 shows the results obtained from a series of example models.

$$Frequency = \frac{1}{2\pi} \sqrt{\frac{\frac{L^2 + 3aL + 3a^2}{6} \cdot \frac{E \cdot b \cdot d^3}{L^3}}{\iiint \rho (y^2 + z^2) dx dy dz}} \propto \sqrt{\frac{(L^2 + 3aL + 3a^2) \frac{b \cdot d^3}{L^3}}{(a^2 + tw^2)}}$$

Equation 3-11

where y is y-dimension of the proof mass
 z is z-dimension of the proof mass
 a in the dimension from the axis of rotation to the proof mass end of the beam

Working from Equation 3-10 and Equation 3-11, if the beam width is fixed, then in order to maintain the resonant frequency the length of the beams must be varied to compensate for changes to the wafer thickness. In the z-axis, the charge output is now proportional to the cube root of wafer thickness, whilst the in-plane charge output is proportional to the wafer thickness to power 1.5. This is confirmed by calculation of a series of example models, with the results plotted in Figure 3-14.

3.5.3. Beam Thickness

The thickness of the support beams is usually controlled by a chemical etch-stop in the wafer. This commonly takes the form of an implanted or doped region of the original silicon wafer, or the use of the silicon dioxide insulator layer within a SOI wafer. Whichever process is used, it is preferable to have all etch-stop regions at the same depth.

The effect of the beam thickness on stiffness and charge generation was investigated. Because the proof mass is fixed, the inertia values in Equation 3-10 and Equation 3-11 are fixed, and for a fixed resonant frequency the beam dimensions must be balanced to achieve constant stiffness. For a range of beam thickness values, the beam length was calculated to maintain 5kHz minimum resonant frequency.

The charge generated by acceleration in the direction of the z-axis was independent of beam thickness. Stiffness is proportional to d^3/L^3 , and therefore beam length is proportional to beam thickness. As the length of the beam reduces, the moments increase, but the area of the piezo-electric sensors decrease. Since these are linear relationships, they cancel out to leave a fixed charge generation value.

If beam length is varied, then for in-plane acceleration the charge generated is dependant on one over the square root of the beam thickness. This is not immediately obvious from Equation 3-11, but has been shown by calculation of example models in Figure 3-15. The use of thin beams generates more charge per unit acceleration in-plane, and is considered preferable on this basis.

3.5.4. Electrode Patterning

In order to obtain the maximum signal to noise ratio from the accelerometer it is proposed to generate the maximum charge per unit of acceleration within the constraints of the specification. This supplies the maximum amount of signal energy to the charge amplifier, giving improved resolution.

The maximum charge would be generated if the entire surface of the beam were to be covered by the piezo-electric sensors, split for positive and negative collection at the exact position that the bending moments (and therefore generated charge) reverse polarity. Since the bending moments in the beams can be calculated (Equation 3-2 and Equation 3-3), the patterning of the piezo-electric sensor electrodes can be designed to

cover areas of maximum bending moment, and not cross into areas of negative bending moment, since this would reduce the net charge generated.

- For pure z-axis acceleration, the point of zero bending moment occurs at the centre of the length of the beam.
- For acceleration only along the length of the beam, zero bending moment occurs at a position x , defined where Equation 3-3 has zero value. This lies at a point between half and two thirds of the distance along the length of the beam, dependent on the geometry of the beams and proof mass.

These can be individually calculated, and used to define the patterning of electrodes for specific axes. When a combination of accelerations is applied, the position of zero bending moment can be anywhere in the outer half of the beam length, dependant on the exact combination of accelerations and geometry. Acceleration not in the chosen direction will not necessarily generate balanced charges from the two piezo-electric sensors on each beam, but by using symmetrical patterns of beams and sensors no net cross-axis signal would be produced.

3.6. Mathematical predictions

The models described above have been created by combining the theory from a number of sources, together with material properties and wafer dimensions selected as typical values. The models provide a comparative tool to determine which of the configurations considered provides the best solution to the specification requirements. When values for the actual processes and materials to be used become available, these can be simply inserted into the models, and the design assessed based on the new information. However, trends should remain true.

The minimum resonant frequency is an important factor in the design of the accelerometer. If the working frequency range (0.5 to 2000 Hz) is close to the resonant frequency in the axis being sensed, then the signal response will tend to be increasingly high as the resonant frequency is approached. If the lowest resonant frequency of the device is not in the sensed axis, but is close to the working frequency range, the deformation of the beams in that axis will tend to be disproportionately large compared to the applied acceleration. Since lateral deflection of the beams causes axial strain (as shown in section 3.4.3), and this affects the stiffness in all directions, then the sensed axis will be affected, and the signal amplitude linearity will be compromised.

The specification laid out in Chapter 1.3 requires that there is equal response from each axis of 80mV/g. This is a requirement of the amplifier output signal, so there is scope for different scalar multiplication on each axis, but it is considered desirable to achieve equal charge response from the three axes. This is unlikely to be achieved by using just

one design of device, so for each design, sensitivity to both z-axis and x- or y-axis acceleration is considered separately.

3.6.1. Single Axis, Semi-symmetrical Devices

The mathematical modelling of the semi-symmetrical device (Figure 3-6) was used to explore a number of variations in order to optimise each device for operation in either the x-, y- or z-axis. In the following cases, the length of the beams is adjusted to maintain the lowest resonant frequency at 5kHz. These single axis devices would be used to sense acceleration in either the z-axis (out of plane) or the y-axis (along the length of the beams). Acceleration in the direction of the width of the beam (x-axis) is not detected.

Separation of Fixed Width Beams

If we first consider the separation of a pair of beams on each opposite side of the proof mass, it can be shown that the greater the spacing between the beams along their side, the greater the stiffness of the device becomes in the x-direction. The graph in Figure 3-16 shows how the y- and z-axis charge output varies with the separation of the beams, when the beams are of fixed width. The length of the beams is varied to maintain the minimum resonant frequency at 5kHz. The two parts of each trace show the charge generated if the x-axis resonance is fixed (the main curve) or if the z-axis resonance is fixed (the horizontal line, no affect). The y-axis resonant frequency was above 5kHz in all cases. The area below these lines is the usable area, where the lowest resonant frequency is above 5kHz. The z-axis is the limiting resonance only when the beams are towards the corners of the mass (large separation of the beams).

Central gap between full width beams

In Figure 3-17 we consider the affect of an increasingly wide gap between beams of reducing width. The beams always extend to the outer edges of the mass. The two parts to each trace again relate to the x-axis or z-axis resonance fixed at 5kHz, with the usable area being below both curves. When the beams touch (separation of 400 μ m), the x-axis is the limiting resonance, but as the beams become narrower and shorter the flat x-axis curve is crossed, and the z-axis resonance becomes the limiting factor.

Proportions of the Proof Mass

Since this device is being used to sense acceleration in a single axis, the proof mass can be shaped to maximise the response from the chosen axis at the expense of others. For a simple rectangular mass, the y-axis sensitivity is improved for beams of a fixed width and a fixed mass if the mass is elongated in the x-direction and narrowed in the y-direction. This increases the beam separation, so reduces x-axis sensitivity, whilst increasing the x-axis resonant frequency. Reducing the y-dimension improves the leverage of the centre of mass relative to the beams (reduce a_1 in Figure 3-6), giving greater charge output from the y-axis.

Inset Beams

The advantages of inset beams are similar for both highly symmetrical and semi-symmetrical devices. If the beams are inset into the mass, it increases the amount of charge generated in the y-axis, since for a given mass the mechanical leverage of the mass increases, increasing the bending moments in the beams. This is shown using a fixed mass in Figure 3-18, where the charge output is plotted against the distance from the axis of rotation to the end of the beams. At the greatest distance (400 μm) the mass is rectangular. The resonant frequency of the x-axis is lowest, so the length of the beams is reduced to maintain 5kHz minimum. As the beams are inset, the z-axis becomes dominant, and the beam dimensions remain constant. At maximum inset (200 μm), the y-axis has the lowest resonant frequency, and the beam length is reduced to maintain 5kHz minimum resonant frequency. The reduced beam length reduces the charge generated, outweighing the benefits of the increased leverage.

Summary

To maximise the y-axis charge generation of a semi-symmetrical device, the proof mass should be elongated in the x-axis in order to increase the x-axis stiffness and resonant frequency, and the beams should be inset in the direction of the y-axis (Figure 3-7) in order to increase the leverage of y-axis acceleration. To make best use of the available wafer space, the central portion of the proof mass would extend to fill the space between the beams, allowing for etched gaps of greater than 50 μm to suit the manufacturing process, since uniform gap widths give a more uniform etch rate across the structure. The portion of the proof mass between the ends of the beams (dimension a_1 in Figure 3-7) must be sufficiently rigid to cause the predicted beam deformations, rather than twisting the bulk material of the proof mass.

Maximum z-axis charge generation is achieved by using a mass elongated in the x-direction, with the lowest resonant frequency being the z-axis, but maximising the beam width. Both x- and y-axis signals should be minimised, since they are both potential contributors to cross-axis sensitivity. This can be achieved by using an elongated mass to reduce x-axis signal, and not inseting the beams, to reduce the y-axis signal.

3.6.2. Two Axis, Highly Symmetrical Devices

The highly symmetrical device (Figure 3-9) is suitable for sensing acceleration in any direction. To sense all three axes individually, two devices would be required; one for the z-axis and a second device for both in-plane axes. Acceleration can be separated into axial components, and cross-axis sensitivity should be at an acceptable level. Within the size range of the proposed highly symmetrical device, all models show that the z-axis is the most responsive. This remains true until the side length of the proof mass is approximately half of the wafer thickness. Due to practical limitations on the available wafer thickness, the proof mass would be very small, leading to very low charge output signals. One way to overcome this is to inset the beams into the mass.

Inset Beams

If the beams are inset into the mass, it increases the amount of charge generated in-plane, since the mass can be increased by using the 'corner' space between the beams without increasing the area of wafer used by the device. This is shown by plotting the results for a series of models in Figure 3-19. The use of inset beams is limited by the geometry when the inner ends of the beams intersect ($a = b/2$ in Figure 3-10). The corners of the mass become isolated without support, and leave a square proof mass, somewhat smaller than the original. This is then identical to the previous highly symmetric device, but with a smaller proof mass, reducing the amount of charge generated.

For maximum response from the x- and y-axes, the beams must all be inset to the centre of the mass, which is obviously impossible to achieve in practice. However, the charge response for in-plane axes can be increased by using inset beams.

3.6.3. Rotationally Symmetrical Devices

In order to separate x- and y-axis signals, the accelerometer must be designed such that no net charge is generated in the y-axis sensors by an x-axis acceleration, and vice-versa. Whilst theoretical models can be made to balance, the mathematical assumptions are critical to the design. Because the deformed shape of each pair of beams is different for a given acceleration, the theory used to calculate the signals also changes. Inaccuracy in one part of the calculation will result in a different cross-axis signal to that which was calculated. It is likely that this design can only be used for the z-axis, since cross axis sensitivity would make the x- and y-axis readings very difficult to distinguish. Cross-axis sensitivity on the z-axis should be similar to the highly symmetrical device, and acceptably low.

The advantage of this configuration is to increase the usable range of lateral beam deflections. On analysis of a number of models using in-line beam configurations, the level of acceleration required to deform the beams by 15% of the beam thickness (section 3.4.3) is typically 150g, three times the working range. Therefore, the benefits of the rotationally symmetrical design are not significant to the current specification.

3.6.4. Modified Semi-symmetrical Design

The modified semi-symmetrical design is only suitable for sensing y-axis accelerations. The relatively high stiffness in the x- and z- axes is almost entirely due to the end support beams. This reduces the deformation of the sensing beams due to cross-axis accelerations, and consequently reduces the level of cross-axis sensitivity. The high stiffness in the x- and z-axes means that the resonant frequency in these axes is also high, again allowing a clean signal to be sensed in the y-axis.

The proof mass should be elongated along the x-axis, as with the semi-symmetrical design, in order to increase the mass relative to the second moment of inertia about the x-axis. This increases the bending moments in the beams for a given acceleration.

Since the sensing beams are only significant to the stiffness in the y-axis, they can be designed to achieve maximum sensitivity, without the compromise required previously to avoid resonance in the x- and z-axes. The beams are required to be the full width of the proof mass in order to maximise the charge generated. This works favourably with the elongation of the proof mass to create beams of large area, and to create large piezo-electric sensors. The y-axis resonant frequency can be set to 5kHz, since this is now the limiting factor on the beam dimensions for a given proof mass.

Piezo-electric electrode connection would be relatively simple since there would be just four piezo-electric sensors per device, and only one axis of sensitivity. Each inner electrode would be connected to the opposite outer electrode, giving a simple layout of tracks across the proof mass.

3.7. Conclusions

The modelling work supports the intent to create a three axis accelerometer. The desired performance specification is compatible with what can be achieved, as calculated by the models.

Within the footprint of 5mm by 10mm, three individual accelerometers can be designed on a single wafer, with each accelerometer measuring one primary axis. Using piezo-electric material to sense the flexing of beams supporting a proof mass, a charge output greater than 5pC/g should be achievable from each accelerometer.

Equal charge response from the three axes is unlikely to be achieved by using just one design of device. Therefore, further development of two or more models is required to find an optimised device for each axis. This is constrained by the wafer and beam thickness dimensions, which are fixed for any one wafer, so must be consistent between devices.

The strongest charge signal from the y-axis was achieved using a modified semi-symmetrical device (Figure 3-12), elongated in the x-direction. This is best able to fit the available space if it is combined with an identical device, rotated by 90° to align for x-axis detection, and a semi-symmetrical device without end support beams (Figure 3-7) for the z-axis. These are defined in the table of dimensions in Appendix 2.

The highly symmetrical device (Figure 3-9) does not achieve such high in-plane charge generation, but the equal response rate for in-plane signals should not be overlooked, since this should give good cross-axis separation. Analysis of the effect of acceleration

in two directions simultaneously is required, to confirm the predicted cross-axis sensitivity.

All calculations in the models described consider acceleration in one axial direction at a time. Acceleration in a direction oblique to the axes must be considered. Dynamic response of the accelerometers has only been considered by calculation of the resonant frequency in each primary axis. This is studied further in Chapter 4 using finite element techniques.

Four structures were selected from the theoretical optimisation for further study.

- o Drawing TAA001 – three sensors on a common wafer die, with each sensor tailored to be sensitive in one axial direction.
- o Drawing TAA002 – a larger device designed to generate larger signals, operating in one axial direction.
- o Drawing TAA003 – an alternative out of plane sensor, for evaluation in comparison with the equivalent sensor of drawing TAA001.

These drawings are shown in Appendix 3.

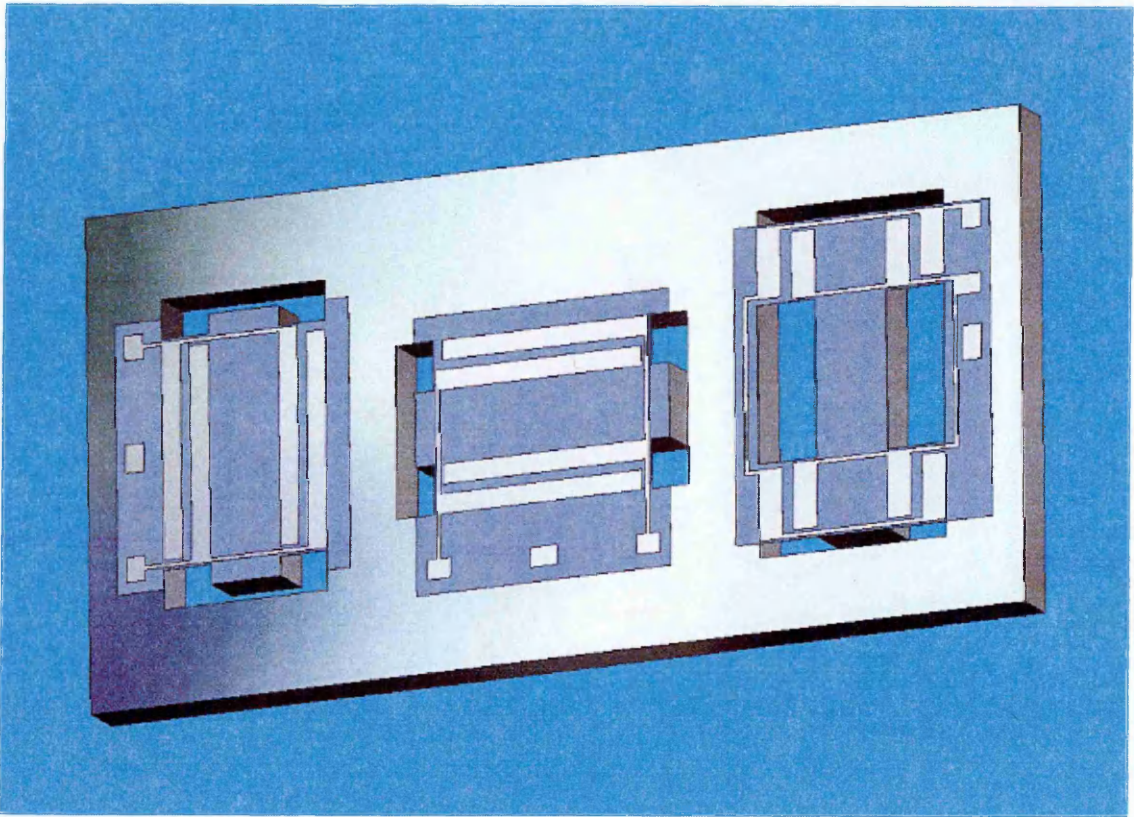


Figure 3-1 Schematic layout for the three-axis accelerometer die

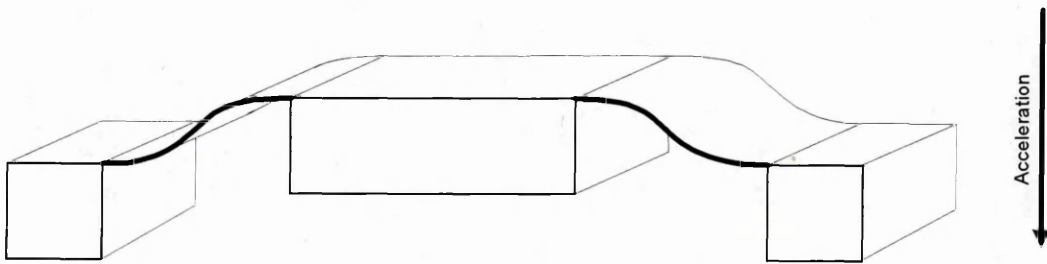


Figure 3-2 Acceleration out of the plane of the beams

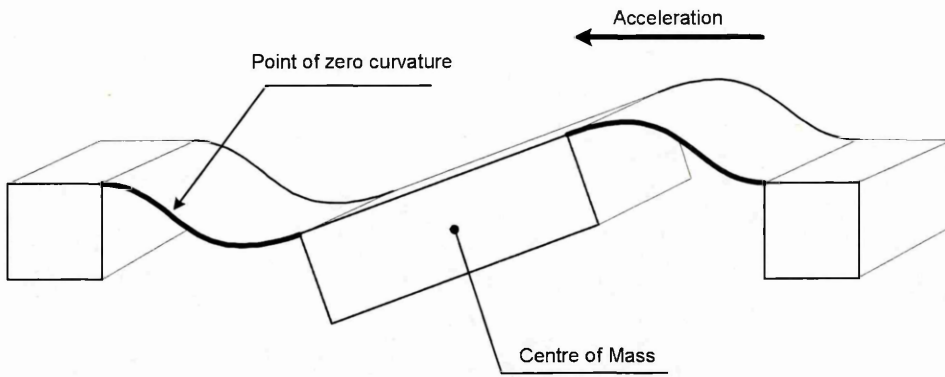


Figure 3-3 Acceleration along the length of the beams

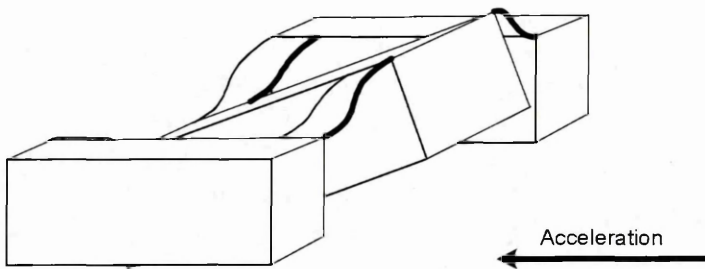


Figure 3-4 Acceleration Perpendicular to the Length of the Beams

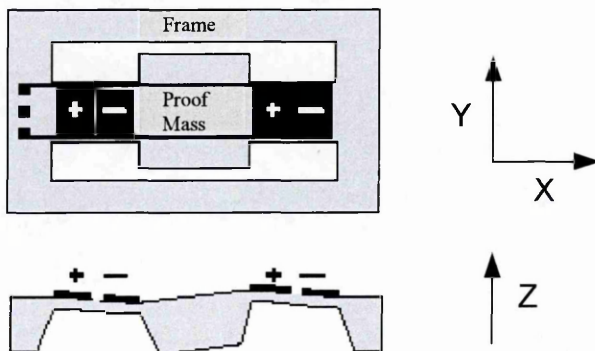


Figure 3-5 Two-beam configuration of semi-symmetrical accelerometer¹⁷

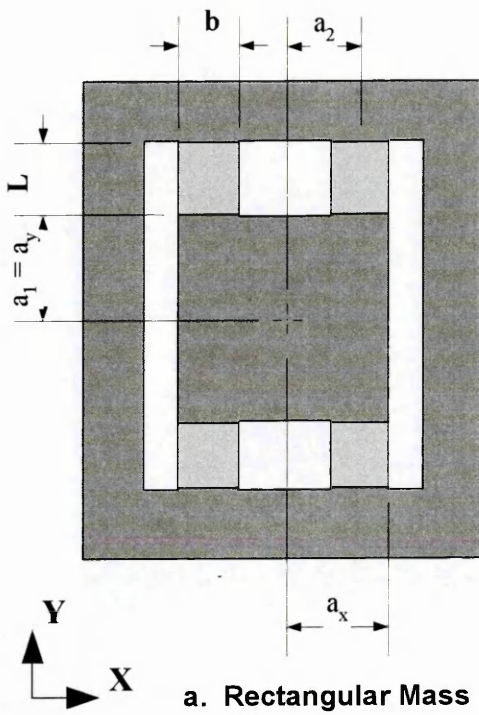


Figure 3-6 Schematic of semi-symmetrical design

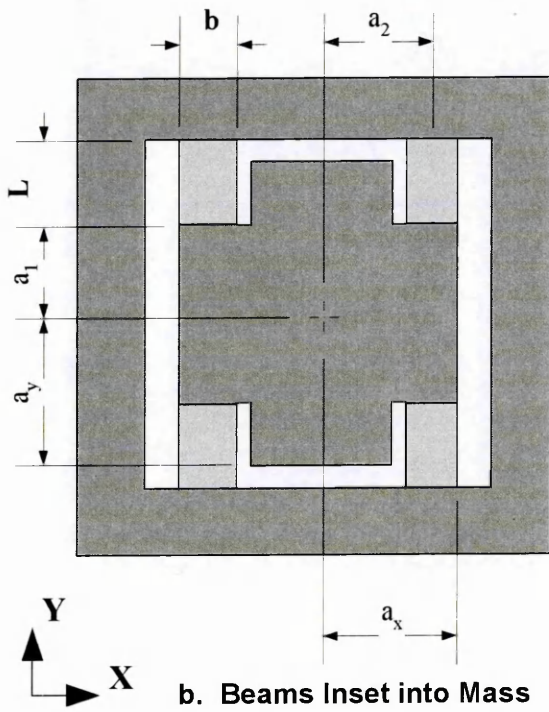


Figure 3-7 Schematic of beams inset into semi-symmetrical design

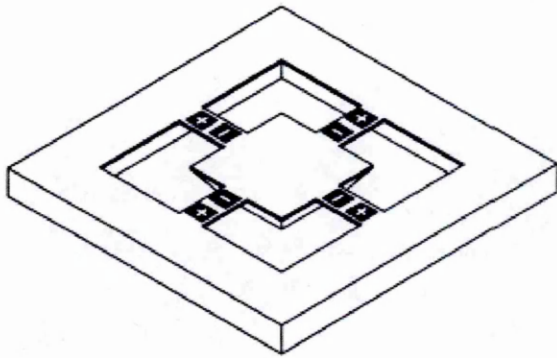


Figure 3-8 4-beam highly symmetrical accelerometer

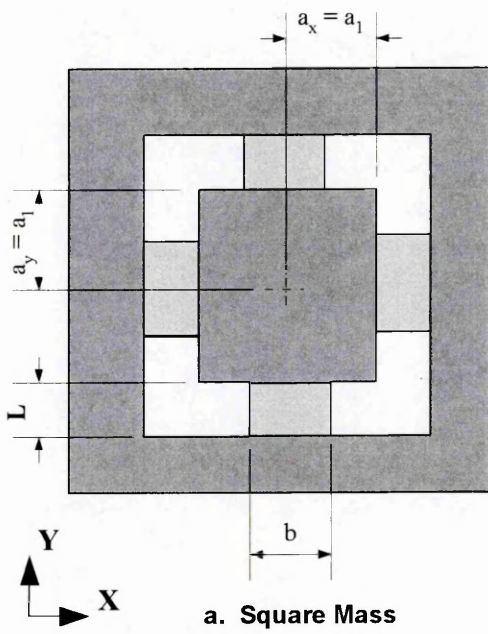


Figure 3-9 Highly symmetrical device

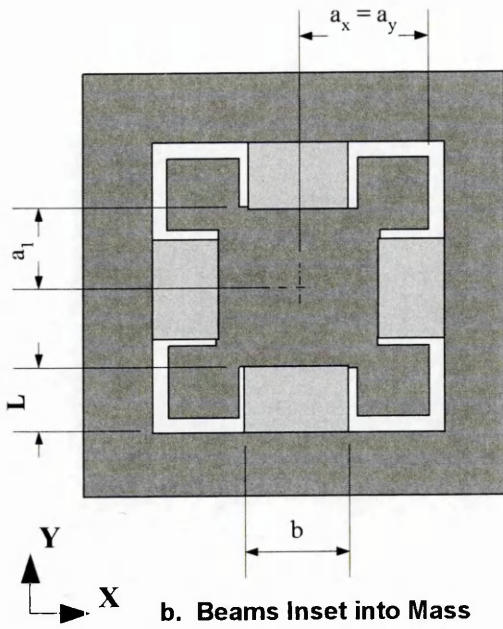


Figure 3-10 Inset Highly Symmetrical Design

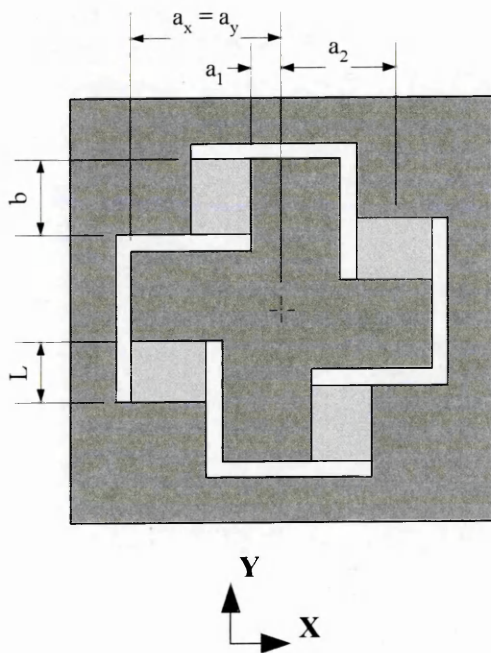


Figure 3-11 Rotationally symmetrical device with offset beams

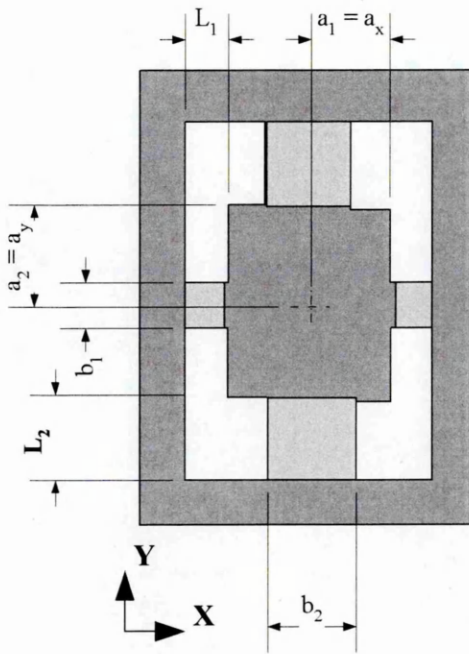


Figure 3-12 Modified Semi-Symmetrical Device with End Supports

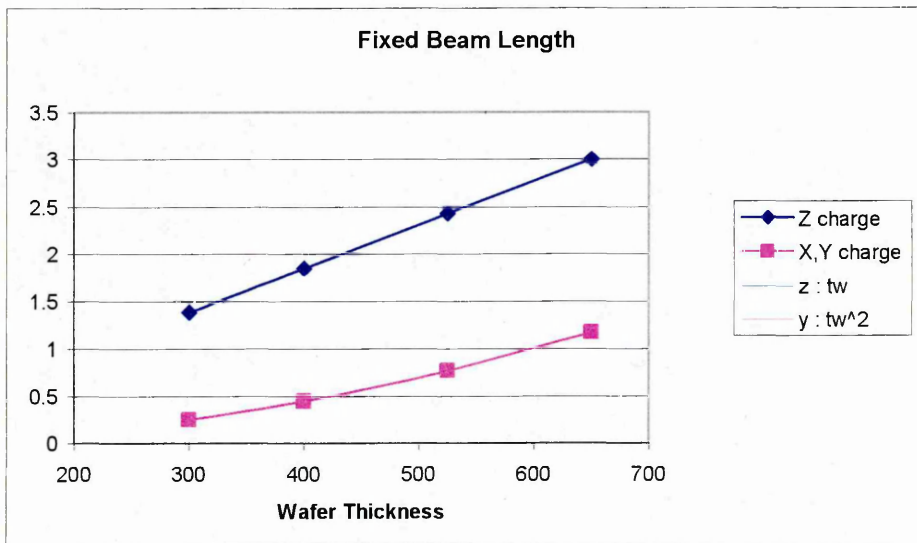


Figure 3-13 Dependence of charge output on wafer thickness

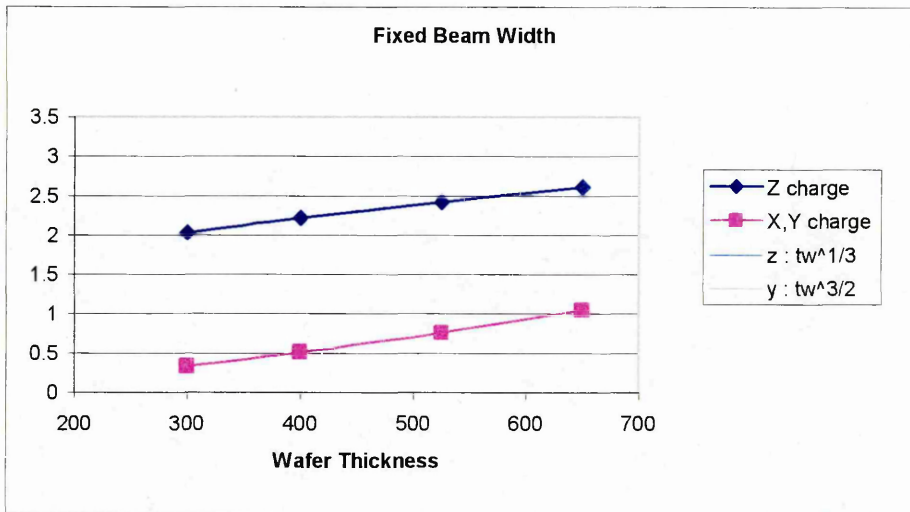


Figure 3-14 Dependence of charge output on wafer thickness

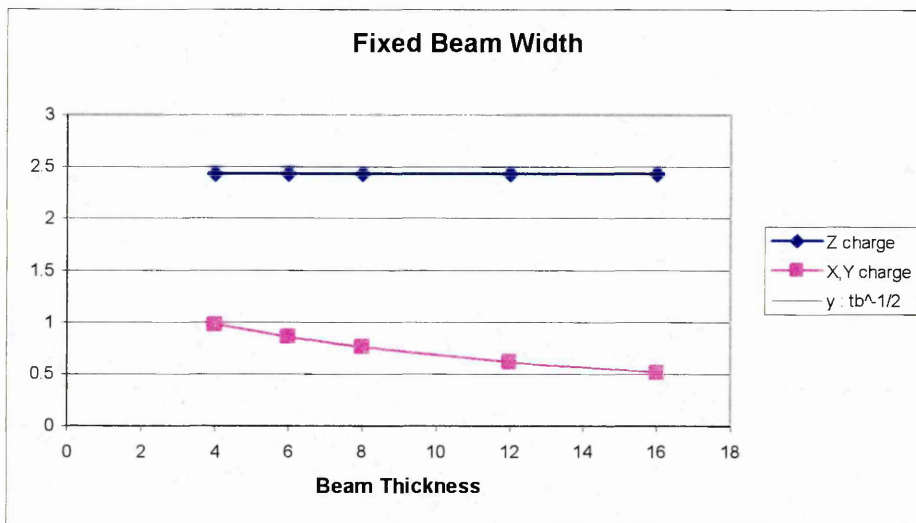


Figure 3-15 Dependence of charge output on beam thickness

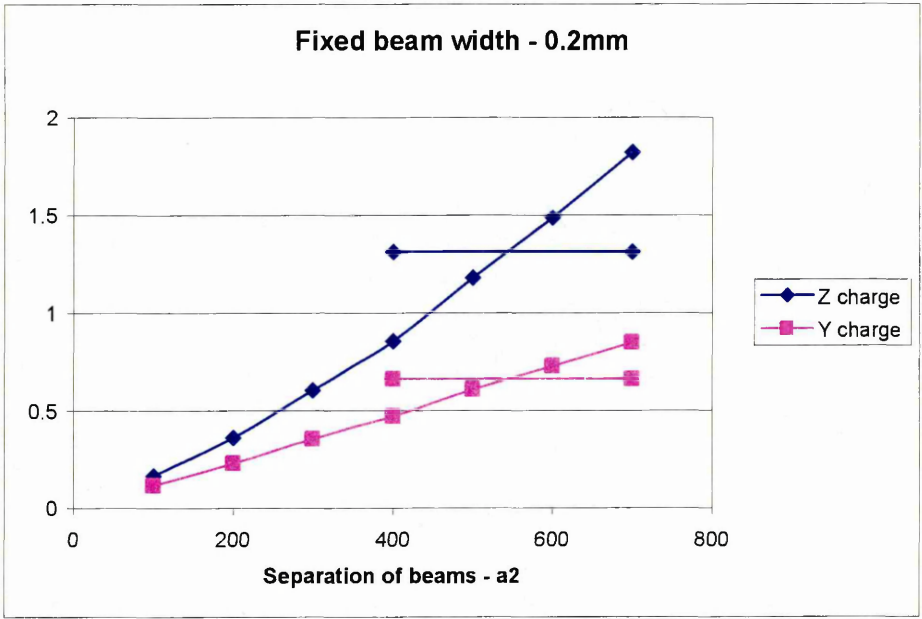


Figure 3-16 Increasing beam separation
 Curve is for fixed x-axis resonant frequency
 Line is for fixed z-axis resonant frequency (no affect)

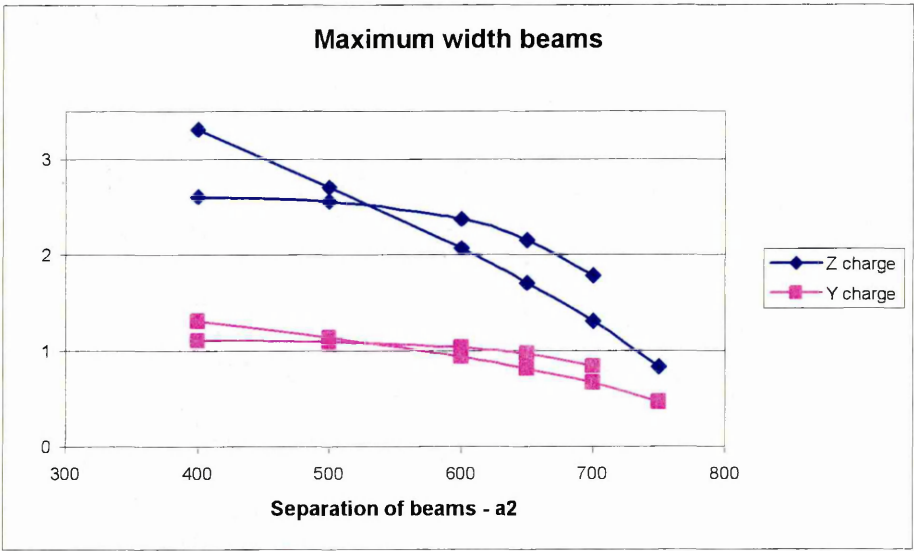


Figure 3-17 Increasing beam width

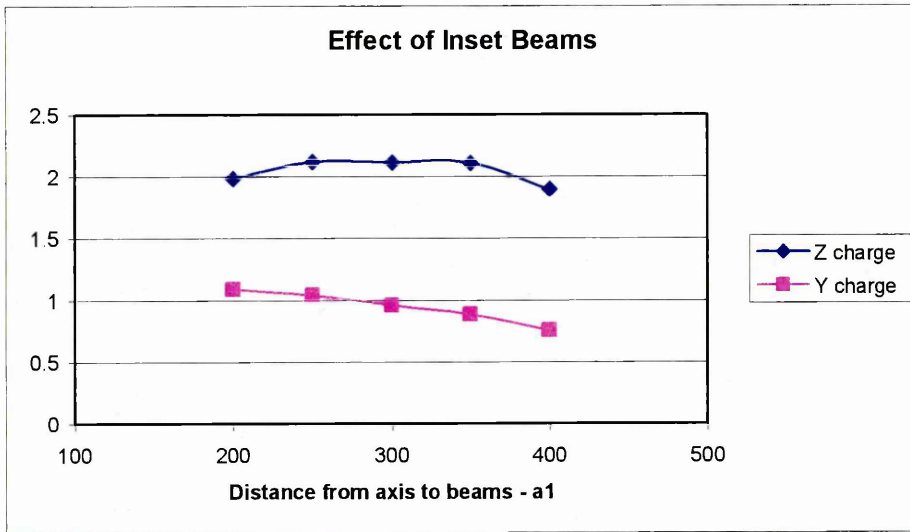


Figure 3-18 Beams inset into the Proof mass

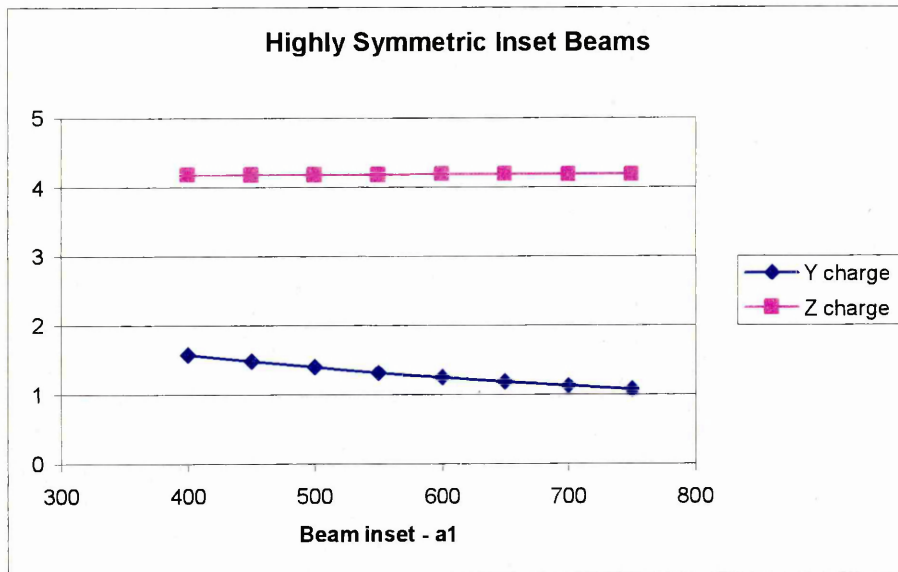


Figure 3-19 Graph showing affect of inset beams on charge output (constant mass)

4. Finite Element Modelling

4.1. Purpose for the Finite Element models

Finite Element models were created using NISA software from EMRC (Engineering Mechanics Research Corporation). The Finite Element (FE) models were used to investigate and detail the designs proposed in the mathematical models. The FE models calculate some of the marginal effects within the structure, but are still limited by the details that are incorporated. There are also limitations in the software package as to which combinations of properties and load cases can be considered together.

The FE modelling concentrates on two areas: Eigenvalue analysis to find the natural resonant frequencies; and dynamic loading to predict the level of charge generation that should be expected. They are also used to assess the affect of alignment tolerances between the beam structure and the electrodes.

All the proposed structures are based on a 525-micron thick SOI wafer, with an 8-micron device layer, which is used to form the beams. Thin film PZT is deposited on the surface of the beams, mass and frame, with electrodes patterned onto the PZT film to form active regions for strain sensing. The direction in which acceleration is sensed depends on the geometry of the mass and beams, the pattern of the active PZT regions, and the order in which the electrodes are connected.

4.2. Approach to Modelling using NISA

The FE analysis was to verify the design of the devices proposed for manufacturing as first prototypes. FE models were created of the proposed accelerometer devices, as optimised using the mathematical models, by manual transfer into NISA format. Appendix 3 shows the drawings for the devices modelled, and Figure 4-1 to Figure 4-4 show views of the NISA models. Each device included a section of 'frame' attached to each beam, to allow local deformations beyond the ends of the beams to be modelled. The NISA models were set-up using millimetres as the standard length dimension, with mass and time in kilograms and seconds respectively. Therefore, other units required scaling to suit, and the scale factors used are shown in Appendix 4.

The bare Silicon structure was modelled initially, and the PZT thin film added in stages corresponding to partial or complete coverage. This matched the options for patterning of the PZT film for prototype manufacturing trials: the PZT is either patterned to match the top electrode, or left as a blanket coating over the entire surface of the sensor. The mathematical model developed in Chapter 3.4.4 was used to calculate the theoretical properties of the composite beam for comparison.

The general shapes of the accelerometer devices have high aspect ratios, with 100-micron wide trenches in a 500-micron thick wafer. Most dimensions are in the range of 0.5 to 5.0 millimetres, but the beam and PZT thickness are 0.008 and 0.001 millimetres resulting in 1.2mm by 2.0mm areas of 1-micron PZT film and 0.1-micron Platinum electrodes. This influences the way in which the FE model is constructed. It was decided that for accurate analysis, two layers of elements should be used on the beams, with an aspect ratio of less than 5:1. This led to a relatively fine mesh over the area of the beams, the area expected to show virtually all deformation and stress, with increasing mesh size in the bulk of the proof mass and frame. Figure 4-5 shows the stress distribution in a cross section through the FE model of a flexing beam.

When the 1 μ m PZT layer was added to the 8 μ m beams, the aspect ratio of this single layer of elements was 20:1 in the areas of interest on the beams, and in some places worse when the PZT was extended to cover the entire face of the device. This aspect ratio is not ideal, but given that the model was already large, it was regarded as necessary: To reduce the aspect ratio of the PZT elements to 5:1 in the region of the beams would approximately triple the size of the model. This was considered impractical on computing time. No attempt was made to model the platinum electrodes above and below the PZT layer, since they are only 0.1 μ m thick.

One objective is to confirm the previous assumptions about symmetry and mode shapes, so complete devices were modelled. An Eigen value analysis was run for each model, and compared to the equivalent MathCAD model. The mode shape for each Eigen value was compared to the predicted form, on which the MathCAD model was based. The mode shapes were all as predicted, except for the highly symmetrical sensor. This had the first resonant frequency in the z-axis direction, as expected, but the in-plane resonance was at an oblique angle rather than along the line of the beams, as can be seen from Figure 4-4.

The second objective is calculation of the electrical output, the PZT thin film was modelled over the entire surface of each structure, with the interface between the silicon and the PZT held at zero volts, representing a grounded bottom electrode. The top electrodes were modelled by constraining the voltage at the relevant nodes using rigid links. The pattern of electrodes is as shown in the drawings, and the order of connection is dependant on the direction in which the device is required to be sensitive. In each model, two or more top electrodes are connected by sharing a common master node.

The same material properties are used throughout, based on the bulk values used by Yu & Lan²⁵.

The output from the FE models is taken as the voltages on the two top electrodes. The capacitance of the PZT sensor elements is calculated from the area, thickness, and dielectric properties, in order that the voltages can be converted to charge output signals. This allows the clearest comparison of the energy output from each device. Overall output from each device is calculated from the difference in the voltage or charge signals on the two top electrodes. This represents the use of an operational amplifier as a comparator, as proposed for the charge amplifier on the prototype devices.

Finally, positional tolerancing was assessed by moving all of the PZT elements in the region of the top electrodes by $2\mu\text{m}$ in X and Y directions. All elements were moved in the same direction, to represent misalignment of the masks. The models were then run with 'ground acceleration', where the rigid constraints applied to the frame of the sensor are moved in the model simulation, as had been previously applied.

4.3. Material Characteristics

In the FE model, the Silicon is represented as an isotropic material, and the PZT as an orthotropic material. The accelerometer structure is aligned with the Silicon crystal, so the principal strains are in the direction of the $\langle 110 \rangle$ crystal lattice. The material property values used are appropriate to this crystal orientation, and the isotropic model should give a good representation of the actual material. Only in the highly loaded end beams of the X or Y axis device of TAA001 (Figure 4-2) is there concern that the isotropic material model may not be sufficient. The sharp corners and high loading at the ends of the beams may lead to inaccuracies, since the direction of the strain as the load is spread into the frame is not expected to align with the $\langle 110 \rangle$ orientation.

The PZT is a truly orthotropic material, and the model should give a good representation of this. The NISA FE package includes the option of modelling piezo-electric materials, with analysis of both the mechanical and electrical properties. The connection of electrodes to the piezo-electric material affects the mechanical behaviour due to the presence or absence of electrical stiffness. To this end, a series of models were run to investigate the variance in resonant frequencies due to the electrode connection arrangement.

4.3.1. Self Excitation of PZT

The FE model of the PZT material takes account of many of the more subtle effects which were omitted from the mathematical model for simplicity. The model including the PZT material was built-up in stages, and checked against the MathCAD model.

The first stage was to disregard the electrical characteristics, and treat the PZT as a conventional orthotropic material. This most closely reflects the assumptions in the MathCAD model.

The second stage was to use thick shell elements (NKTP 5) for the PZT layer instead of brick elements (NKTP 4). The thick shell element "... is derived by specializing the 3-D solid element (NKTP 4) to have a linear variation of displacement through the thickness. It is suited for modelling 3-D thick shell structures where the normal stress and strain through the thickness are not negligible."³⁹ This should more closely model the thin film PZT layer, but there is no piezo-electric element equivalent to NKTP5 available. This analysis is only useful to assess the variance in results due to assumptions in the element type.

The third stage was to apply voltage constraints to one or both sides of the piezo-electric layer, and run a piezo Eigen analysis using piezo electric brick elements (NKTP 6). When one side of the PZT layer is constrained at zero volts, the analysis should display voltage generation over the PZT. If the other side of the PZT layer is connected by a floating electrode (modelled in NISA as a voltage rigid link) the average voltage should be generated, representing connection to a voltage amplifier. If the floating electrode is constrained at zero volts the charge output can be calculated, representing connection to a charge amplifier.

4.4. Verification of the beam models

Since the NISA models for the beams are known to be constructed from a low number of elements, particularly through the thickness of the beams, it was considered necessary to verify that they were still calculating the stresses correctly. The reduced number of elements reduced the model size, and run times for the model load-cases. The elements are also distorted, with large aspect ratios (20:1 for the PZT layer), again to try to moderate the size of the complete models. This section investigates the affect of these compromised elements on the output from the models.

4.4.1. FE analysis Models

In order to analyse the effect of element size on the modelling of the beams, a section of beam 80 μ m square, comprising 8 μ m of silicon, and 1 μ m of PZT was created.

- o This was constrained rigidly along one side face, to eliminate movement.
- o The opposite face was constrained by a displacement rigid link.
- o A force was applied to the master node of this rigid link, creating a cantilever bending moment.
- o The interface between the silicon and the PZT was constrained at zero volts.
- o The top surface of the PZT was constrained by a voltage rigid link.
- o Material properties are identical to those used in the full device models.

The results from the two models were compared, and an assessment of the errors made.

Few elements - as per the full device models

The silicon was modelled as two elements thick, whilst the PZT was a single elements thick. Each layer consisted of four elements by four elements. The silicon elements had an aspect ratio of 5:1, and the PZT 20:1.

Many elements - for increased accuracy

The silicon was modelled as 20 elements thick, whilst the PZT was 5 elements thick, with 50 by 50 elements in each layer. The silicon elements had an aspect ratio of 4:1, and the PZT 8:1. This model is shown in Figure 4-6.

4.4.2. Verification Calculations

Displacement is calculated in Equation 4-1 using the second moment of area (I) for the composite beam. This must be calculated as a beam of length to the load point, with the load plus a moment applied at the point where the rigid link joins the element model.

$$D = \frac{W}{6 \cdot E \cdot I} \cdot (2 \cdot l^3 - 3 \cdot l^2 \cdot a + a^3) + \frac{M}{2 \cdot E \cdot I} \cdot (l^2 + a^2)$$

$$D = \left(\frac{2 \cdot 0.1^3 - 3 \cdot 0.1^2 \cdot 0.02 + 0.02^3}{6} + \frac{0.02 \cdot (0.1^2 - 0.02^2)}{2} \right) \cdot \frac{1}{169 \times 10^6 \cdot 4.076 \times 10^{-9}}$$

$$\text{Displacement} = 0.4800 \mu\text{m}$$

Equation 4-1

The Charge Output is calculated in Equation 4-2 using I value for the silicon beam.

$$\varepsilon = \frac{M + W \cdot x}{E \cdot I} \cdot \frac{d}{2} = \frac{0.02 + 1 \cdot x}{169 \times 10^6 \cdot 3.413 \times 10^{-9}} \cdot \frac{0.08}{2}$$

$$Q = \int \varepsilon \cdot dx \cdot b \cdot d_{31} \cdot (c_{11} - \nu_{12})$$

$$Q = \int_0^{0.08} 0.02 + x \cdot dx \cdot \frac{0.04}{169 \times 10^6 \cdot 3.413 \times 10^{-9}} \cdot 0.08 \cdot 93.5 \times 10^{-15} \cdot (72.46 - 0.295 \cdot 20.75) \times 10^6$$

$$\text{Charge} = 16.52 \times 10^{-12} \text{ C}$$

Equation 4-2

Capacitance of the model is calculated in Equation 4-3 allowing the Voltage Output to be calculate in Equation 4-4 by dividing Equation 4-2 by Equation 4-3.

$$C = \epsilon_{33} \cdot \frac{b \cdot l}{t} = 6.4605 \times 10^{-12} \cdot \frac{0.08 \cdot 0.08}{0.001}$$

$$C = 41.35 \times 10^{-12} F$$

$$\text{Capacitance} = 41.35 \times 10^{-12} F$$

Equation 4-3

$$V = \frac{\text{Charge}}{\text{Capacitance}} = \frac{16.52 \times 10^{-12}}{41.35 \times 10^{-12}}$$

$$V = 0.3995V$$

$$\text{Voltage} = 0.3995 V$$

Equation 4-4

4.4.3. Verification Results

Voltage output from the cantilever load-case corresponds to the calculated output from the full device models. The displacement at the applied load point, and the average voltage generated by the PZT layer are consistent between the theory and the FE models with few or many elements.

	Few elements	Many elements	FE Variance	Theory
Displacement (μm)	0.4582	0.4663	1.74%	0.4800
Voltage Output (V)	0.3918	0.4084	4.06%	0.3995

The poor aspect ratio of the elements in the beams of the accelerometer models (few elements), and the fact that the PZT layer is only one element thick does not appear to adversely affect either the mechanical behaviour or the voltage output predictions. In this example, the model with the fine mesh has predicted less than 2% greater deflection, and 4% greater voltage output than the coarse model. Theoretical predictions fall within 5% of the FE model values calculated.

4.5. Large Deflection Theory

The range of proposed accelerometer devices all comprise of a proof-mass supported in a frame by either two or four beams. The beams are arranged in pairs, and in each case, the beams and mass form a bridge across the frame. Movement of the mass causes lateral displacement of the beams, and because both ends are restrained also creates axial loading in the beams. In Chapter 3.4.3 it was shown that 3% amplitude linearity should be maintained if the deflection is less than 0.15 times the beam thickness.

Linear theory is usually used for calculating small deflections of the beam. From Roark²⁶ this takes the form of Equation 4-5.

$$\text{Deflection} \quad dy = \frac{W.l^3}{192.EI}$$

Equation 4-5

Within the working range of the devices, it is required that the effect of axial load should not affect the linearity. As the lateral deformation (dy) increases, the axial load on the beams increases as a function of the lateral deformation squared (dy^2). This is stated from Roark in Equation 4-6.

$$\text{Deflection} \quad dy + \frac{A}{16I} dy^3 = \frac{W.l^3}{2\pi^4 EI}$$

Equation 4-6

For very small deflections, dy^3 tends to zero, and there is discrepancy between Equation 4-5 and Equation 4-6, since $2\pi^4$ equals 194.8 and not 192. For the calculations in this report, Equation 4-6 has been modified to use 192 instead of $2\pi^4$.

Roark continues to define the axial load in Equation 4-7, and similarly from vanKampen and Wolffenbuttel²⁴ we get Equation 4-8. These equations are equal when Equation 4-9 is satisfied.

$$\text{Axial load} \quad P = \frac{\pi^2 E.A}{4l^2} dy^2$$

Equation 4-7

$$\text{Axial load} \quad P = \frac{E.A}{2l} \int_{x=0}^l \left(\frac{dy(x)}{dx} \right)^2 dx$$

Equation 4-8

where $\frac{dy(x)}{dx}$ is the gradient of the beam.

$$y(x) = dy \cdot \cos\left(\frac{\pi \cdot x}{l}\right) - 1$$

Equation 4-9

where dy is the maximum deflection of the beam.

It is expected that the effect of axial strain is not significant if the displacement is significantly less than the beam thickness

$$\frac{dy^2}{d^2} \ll 1 \quad \text{where } d \text{ is the beam thickness.}$$

From the FE models, with 50g acceleration (maximum working range) the deflection is typically 0.4µm out of the 8µm beam thickness, giving the ratio of deflection over beam thickness as 0.05. Corresponding linear and non-linear theoretical values have also been calculated, and are shown in Table 4-1.

It can be seen that there is variation between the FE and the theoretical results, but the difference between the linear and non-linear theory is below 0.2%. The FE model predicts more displacement than theory, since the FE allows deformation of the proof-mass and frame in the regions around the ends of the beams. The variation between the FE and theoretical results is largest for beams with high strain, showing more deformation beyond the ends of the beams. The TAA001 XY device (Figure 4-2) is particularly restricted in its movement due to the end support beams, and the difference between theoretical methods is minimal.

Similar results are found for the in-plane deformations. The maximum deflection is less than 0.4µm in all cases, and the variation between the theoretical methods is below 0.2%.

4.6. Finite Element predictions

The results of NISA FE runs were compared to MathCAD models. The FE element types were NKTP 4 bricks, and NKTP 6 piezo-bricks. The Lanczos solver was used with sparse matrix analysis. A range of options were considered in the FE models, as detailed below.

4.6.1. Distribution of the PZT Film

There is a fabrication option to have PZT in patches only where required for sensing, as shown in Figure 4-1 to Figure 4-4, or as a continuous film over the entire surface of the sensor, with only the highlighted regions of the PZT being poled and active. This is determined by the choice of mask for the PZT etch, matching either the top or the bottom electrode.

The greater the coverage of the PZT film, the stiffer the beams become, increasing the resonant frequencies. The PZT coverage increases from left to right across each table. The MathCAD and NISA results are compared directly by reading down the columns in Table 4-2 to Table 4-5. The first resonant frequency is within 3% between methods in all cases, with higher modes (not tabulated) showing less accurate agreement. In all cases, the 1 μ m PZT layer increases the resonant frequencies by about 10% compared to the bare 8 μ m silicon beams. In all examples, the same percentage increase in resonant frequency is indicated irrespective of the method of calculation (mathematical or FE).

In the case of the TAA003 Z axis device, the in-plane mode shapes were at approximately 40° to the axis of the beams. This was due to the almost axis-symmetric configuration. The actual mode shape is shown in Figure 4-4. This introduces more undesirable, torsional deformations than had been assumed in the mathematical model, and stiffens the device. Thus the FE model predicts higher frequencies than the MathCAD model by around 5%.

4.6.2. Self Excitation of PZT

A series of models were run to assess the voltage stiffening effect due to self excitation of the PZT layer. These took the NISA model for the TAA001 Y axis model, with patches of PZT only where required for sensing, as shown in Figure 4-2. By connecting all of the bottom electrodes (between the silicon and the PZT) to zero volts, and applying different electrical constraints to the upper electrodes (on the visible surface of the PZT) a number of effects can be demonstrated. This is shown in Table 4-6.

The element type used for the FE analysis has a significant effect on the output. Comparing models with brick or thick shell elements for the PZT layer (NKTP 4 or 5), and brick elements throughout the rest of the model (NKTP 4), there is a 3.3% increase in the first resonant frequency. The use of general brick elements is forced by the element type availability (NKTP 6 bricks for the active piezo elements), but the variance between methods is an indicator of the absolute accuracy of the results.

The effect of voltage stiffening can be seen quite clearly by comparing the Y axis frequencies, and several features should be noted.

- The X and Z axis resonant frequencies are dominated by the end beams, where there is no PZT in these models, so are virtually unaffected by the PZT properties.
- When the piezo-electric layer is short circuited, the resonant frequencies match exactly with those generated by a non-piezo-electric model.
- With no top electrodes, the voltage stiffening is most significant, but still low. The X axis frequency is increased by 1%, and the previous assumptions to ignore the effect is shown to be reasonable.

- Where the electrodes are allowed to electrically float, the voltage is distributed throughout the PZT patch. This affects the stiffness of the beams, but less than when the PZT is completely open circuit.
- With the floating electrodes, symmetry in the voltage generated by X axis accelerations gives nearly zero output from any electrode. The voltages generated within a PZT patch are equal but opposite, and self cancel, eliminating the voltage stiffening.

Voltage stiffening of the PZT does not affect the resonant frequencies to any significant level, and can be reasonably omitted from further calculations. This also means that the method of amplifying the raw signal from the sensor will not affect the resonant frequencies.

4.6.3. Voltage Output from PZT sensors

The models used to compare the self excitation of the PZT also allow the output voltage to be demonstrated. This is only comparative, since Eigen analysis does not produce absolute force and displacement values, and only frequencies are true values. Figure 4-7 shows the relative voltage distribution generated on the PZT sensors when only one side is connected to an electrode. This pattern matches the stress distribution in the PZT.

When the electrodes are modelled above and below the PZT layer, the voltage generated is the average value over each electrode. All bottom electrodes are fixed at zero volts, and the top electrodes are allowed to float. The electrical behaviour is for the charge generated to be distributed over the capacitor (formed by the electrodes with PZT dielectric). Opposing charges will cancel out, reducing the voltage on the capacitor (the sensor output signal). The direction of sensitivity can be selected by connecting the electrodes such that the unwanted signals cancel out, and desired signals are maximised.

The numbering of electrodes is shown in Figure 4-8. For Y axis sensing opposite pairs are connected; electrodes 1 & 4, and electrodes 2 & 3. For Z axis sensing, inner electrodes 1 & 3 are connected, and outer electrodes 2 & 4 are connected. This device cannot be configured for X axis sensing. Table 4-7 shows the relative overall voltages generated using these configurations in response to accelerations in each of the primary axes.

4.6.4. Response of the Devices

The four proposed devices were created as FE models, with the TAA002 device being run twice, connected for sensing in X and Z directions. Each model was subjected to a range of load-cases, by applying acceleration in the stated direction or directions, and analysing the steady state response. The results are summarised in Table 4-8 to Table 4-12, with the full results shown in Appendix 5.

In each table of results, the electrode voltage responses from the FE models are stated, the total capacitance of the PZT sensors is quoted, and the charge output of each set of connected sensors is calculated (Voltage x Capacitance = Charge). In all cases, the symmetry of the models means that the capacitance of each set of connected sensors is half of the total capacitance quoted. The voltage and charge response of the MathCAD model is shown directly below the sensitive direction FE results for direct comparison. It can be seen that the cross-axis sensitivity is about 10 orders of magnitude lower than the sensitive axis sensitivity on the perfect device models.

4.6.5. Positional Tolerance

A second set of results for each device is obtained from imperfect models, where the sensor electrodes are offset from their intended positions by 2 microns in both X and Y directions. This represents misalignment between the masks for the top electrodes and the silicon etching. The FE models are loaded by applying 50g to each axis individually.

Table 4-13 to Table 4-17 show the results from the misaligned devices, and compare them to the response of a perfect device loaded in the sensitive direction. The 'Cross axis' sensitivity is the charge response generated from the non-sensitive axis divided by the charge response from the sensitive axis of the same model. For the response of the TAA001 Y-axis sensor to Z-axis acceleration, this calculates as

$$0.001pC/g \div 4.838pC/g$$

The 'Reduction in sensitivity' is the difference between the perfect device and the misaligned device in the charge response to acceleration applied in the sensitive direction. For TAA001 Y-axis sensor this calculates as

$$1 - (0.001pC/g \div 4.838pC/g).$$

The calculations are all to six significant figures, hence the displayed figures do not agree exactly.

With the electrodes misaligned by 2 microns in both X and Y directions, it can be seen from Table 4-13 to Table 4-17 that the cross axis sensitivity is below 0.05% in all cases except when the TAA002 device is sensing in the Y axis. The sensitivity in the desired direction is reduced by up to 0.33%. Again, the full table of results is shown in Appendix 5.

4.7. Discussion of FE models

4.7.1. Correlation Between Maths and FE

There is generally good correlation between the MathCAD and NISA results. The mode shapes of the deformed structures match the predictions used for the mathematical model very closely in almost all cases. In-plane deformations take the form of pivoting

about the mid thickness of the beams, whilst out-of-plane Z axis deformations are simply translations of the proof mass, with all beams deforming through an equal distance. These mode shapes are shown in Figure 4-1 to Figure 4-4.

For the TAA001 Z axis device, the resonant frequencies for all axes agree to within 5%. The Y axis is affected by the torsional deformation of the beams, but not to a significant extent. The Z axis may be affected by the mass of the beams (0.1% of the total), or the deformation beyond the ends of the beams. Neither consideration was included in the maths model, or has a significant affect on the resonant frequencies.

For the TAA001 Y axis device, resonant frequency calculations gave good agreement with the MathCAD for the first resonant frequency (Y axis within 1%), but less satisfactory in the Z (10% variance) and X (30% variance) axes. This is believed to be due to differences in the method for simplification of the beam structure in the mathematical and Finite Element models. When X or Z axis acceleration is applied, the end beams undergo significant axial strain. With this loading applied, the lateral stiffness of these beams is positively affected. In the main beams the effect is not significant, so was omitted from the maths calculations, but in this case it may cause up to 10% increase in the X and Z axis resonant frequencies. The X axis frequency is also affected by poor calculation of the torsional stiffness of the main beams in the maths model (Figure 4).

For the TAA002 high output device, the Y and Z axes are within 5%, but the X axis resonant frequency is 12% lower in the FE analysis than MathCAD. The X axis discrepancy is believed to be due to the poor modelling of the torsional distortion of the beams in the maths model, but this mode is still significantly above the first resonant frequency.

For the TAA003 Z axis device the first mode shape (Z axis) and frequency agreed to within 2% between FE and maths methods, but from FE the second and third mode shapes were at oblique angles to the expected axes (Figure 3.c), and the predicted shapes (true to the axes) were not calculated by FE. The calculation of the oblique mode shapes was not obvious from inspection of the original design, and highlights the importance of using full models in the FE, and not relying on previous assumptions. This caused more torsional deformation of the beams than expected, and gave a 5% higher resonant frequency.

When the PZT layer is added to the silicon structure, both FE and maths modelling methods show around a 10% increase in the resonant frequencies. This is very consistent, with all models giving increases in the range of 9 to 10%. This gives confidence to use the maths model for composite beams²⁸ to extrapolate results from the FE models.

The advantages of FE and maths methods can be combined, since the maths can handle sub-micron layer thicknesses, but the FE is able to calculate more accurately the stiffness of the beams under torsional and axial loadings. For example, the maths model is able to calculate for the electrode layers (0.1 μ m of Platinum), which prove unfeasible to model in NISA. From the maths model, the addition of Platinum electrodes both sides of the PZT layer increases the stiffness of the beams by 8%, and since resonant frequency is proportional to the square root of stiffness, an increase of 4% in the resonant frequencies. This combined approach means that more detail can be included in the final model.

4.7.2. Distribution of the Applied PZT Film

The greater the area of the sensor which is covered by the PZT film, the greater the stiffness of the beams, and consequently the higher the resonant frequencies. This is in line with the expected behaviour in the mathematical model, where it is assumed that the deformation is limited to the beams. The correlation to within 3% between resonant frequencies calculated using maths and FE, and the frequency increase of less than 1% between the PZT patches and full coverage of PZT in the FE models shows this to be a reasonable assumption.

In the case of the TAA001 Y axis sensor, the X and Z axis resonant frequencies are dominated by the end beams. If the PZT film is applied as patches on the main beams only, the moving mass is increased without significantly increasing the stiffness of the support. The X and Z axis resonant frequencies are fractionally decreased by the addition of the PZT patches. When the PZT film is applied to the entire face of the sensor, the stiffness of the end beams increases, and all resonant frequencies are increased.

4.7.3. Voltage Output from PZT sensors

In all of the devices modelled, the lowest resonant frequency is associated with the axis to be sensed, and this is increased by the addition of the PZT film. This implies that the PZT sensor regions are correctly placed where there is high strain caused by the acceleration to be sensed.

The voltage generation patterns demonstrated by the TAA001 Y axis sensor without electrodes are shown in Figure 4-7. These match the predictions of surface strain in the silicon beams from the maths model. This again confirms correct placement of the sensing electrodes.

When the average voltages generated on floating electrodes are analysed (section 4.6.3) it can be seen that the symmetry of motion is very high. On this geometrically perfect FE simulation there is very little cross-axis sensitivity, with 10 orders of magnitude separation between the desired signal and the noise from other axes. The voltages generated by X axis resonance may be due to rounding errors in the calculation, or to

the axis of rotation being fractionally away from the ideal mid-point of the main beams. Cross axis signal noise is expected to be affected by positional tolerances on the placement of the PZT and electrodes on the beams, and by electrical pick-up.

4.8. Comparison of FE and mathematical models

The FE Eigen analysis to find resonant frequencies agrees well with the mathematical models (within 3% for the first resonant frequency), and generally confirms the mode shape predictions, but highlights some areas of weakness in the models.

Full models should be used in the FE analysis, since the greater the symmetry of the model, the greater the likelihood of oblique mode shapes occurring. In the highly symmetrical example from Yu & Lan²⁵, the FE modelling assumes the same constraints of symmetry as the maths, and uses a quarter model. This does not allow the oblique axis modes to be calculated.

The ability of the mathematical model to calculate stiffness due to torsional deformation of the beams (Figure 4) is shown to be questionable. When the torsional component is a significant portion of the overall stiffness, the FE Eigen analysis resonant frequency results can vary by up to 12% from the maths model. If this is combined with high axial loads in the beams, the resonant frequency calculations can be up to 30% different between FE and the maths. This modelling weakness does not cause any great concern, since the torsional deformation is in the un-wanted axial directions, and does not affect the lowest resonant frequencies.

The choice of element type for the FE model is shown to affect the resonant frequency by 3.3%, but the type of elements used is forced by limited availability of piezo-elements. The results calculated show piezo or non-piezo brick elements used to be in closer agreement with the maths model than the non-piezo thick shell elements.

The addition of 1 μm of PZT to the 8 μm thick beams increases the resonant frequencies by about 10%. This is consistent for both the maths and FE models, and gives confidence to extrapolate FE results by using the multi-layer, multi-material beam model (Appendix 1.3). This maths model allows calculation with layer thickness which would be un-feasible in NISA, and can calculate how the resonant frequencies change with the layer build-up on the beams.

The voltage stiffening effect of open or closed circuit electrodes for the PZT gives less than 1% variation in the resonant frequencies. The closed circuit configuration simulates all available charge being absorbed by the charge amplifier, and gives identical resonant frequency results to the non-piezo model.

The FE models agree well with the MathCAD predictions for charge generation. The FE typically predicts charge generation up to 4% greater in the sensitive direction than the maths.

Cross-axis sensitivity for the device exactly as drawn is typically 10 orders of magnitude below the desired sensitivity. When misalignment of the electrodes is considered, the cross-axis sensitivity increases. 2 microns out of position in both X and Y directions typically gives less than 0.05% cross-axis signal, which is well within the 1% specified.

Misalignment of the electrodes reduces the sensitivity of the devices, by less than 0.33% for 2 microns out of position in both X and Y directions. This is well within the 3% signal amplitude linearity specified.

Predicted stress in the sensors over the working range is at least two and usually three orders of magnitude below the fracture strength. Under shock loading of 1000g in all directions (1730g total load, applied as a single transient 'ground acceleration' loading), the end beams of the TAA001 device are stressed to approximately their fracture strength (0.6 GPa). For all devices under a loading of 1000g in any one axial direction, there is a safety margin of at least two times. In all cases, acceleration in the Z axis direction generates the maximum strain in the device. The fracture strength specification to survive 1000g loading should be achieved by all devices.

Modelling of the accelerometers using FE methods has confirmed the specification requirement that the deflection of the beams is sufficiently small for there to be good linearity of the sensors. This has been cross checked by calculations based on the applied forces, which show that non-linearity from this source should be less than 0.2%.

Table 4-1 Displacement from 50g Z-axis acceleration

	FE Displacement	Linear Theory	Non-Linear Theory	Theory Variation
TAA001 XY	0.039 μm	0.0323 μm	0.0323 μm	0.001 %
TAA001 Z	0.417 μm	0.407 μm	0.406 μm	0.17 %
TAA002	0.430 μm	0.405 μm	0.404 μm	0.17 %
TAA003	0.418 μm	0.412 μm	0.411 μm	0.18 %

Table 4-2 TAA001 Z axis sensor - both sides of PZT layer held to zero volts

First three resonant frequencies (Hz)

Axis	MathCAD		MathCAD
X	7309		7987
Y	6834		7468
Z	5043		5511
	NISA 8um Silicon	NISA 8um Silicon	NISA 8um Silicon
X	7306	7952	8001
Y	6572	7148	7183
Z	4944	5385	5408

Table 4-3 TAA001 Y axis sensor - both sides of PZT layer held to zero volts

First three resonant frequencies (Hz)

Axis	MathCAD	MathCAD	MathCAD
X	20534	20539	22437
Y	5066	5506	5535
Z	18025	18042	19695
	NISA 8um Silicon	NISA 8um Silicon	NISA 8um Silicon
X	26564	26489	28949
Y	5096	5495	5538
Z	16406	16354	17863

Table 4-4 TAA002 High Output sensor - both sides of PZT layer held to zero volts

First three resonant frequencies (Hz)

Axis	MathCAD		MathCAD
X	8865		9686
Y	5063		5532
Z	5095		5568
	NISA 8um Silicon	NISA 8um Silicon	NISA 8um Silicon
X	7957	8679	8704
Y	4971	5422	5444
Z	4941	5385	5402

Table 4-5 TAA003 Z axis sensor - both sides of PZT layer held to zero volts

First three resonant frequencies (Hz)

Axis	MathCAD		MathCAD
X	6980		7628
Y	6980		7628
Z	5027		5493
	NISA 8um Silicon	NISA 8um Silicon	NISA 8um Silicon
X	7232	7866	7907
Y	7232	7866	7907
Z	4945	5392	5410

Table 4-6 TAA001 Y axis sensor Predicted resonant frequencies

First three resonant frequencies (Hz)

Axis	MathCAD with 1um PZT	NISA 8um Non-piezo (NKTP 4)	NISA 8um Thick Shell (NKTP 5)
X	20539	26489	26495
Y	5506	5495	5678
Z	18042	16354	16364
	NISA Piezo Bottom electrode 0 V No Top Electrodes	NISA Piezo Bottom electrode 0 V Floating Top Electrodes	NISA Piezo Electrodes Both Sides 0V (short circuit)
X	26491	26489	26489
Y	5552	5540	5495
Z	16358	16357	16354

TAA001 Y axis sensor electrode configurations.

8um silicon beams with PZT patches (electrodes over entire PZT patch).

Table 4-7 TAA001 Relative open circuit Voltage Output calculated using NISA

Electrode No.	Mode 1 - Y axis	Mode 2 - Z axis	Mode 3 - X axis
1	2.668E+10	-7.972E+09	-7.767E-01
2	-1.765E+10	1.186E+10	1.581E+00
3	-2.668E+10	-7.972E+09	3.765E+00
4	1.765E+10	1.186E+10	-6.267E+00
Overall			
Y axis Connection	4.639E+10	0.000E+00	-5.818E+00
Z axis Connection	0.000E+00	1.894E+10	-3.643E+00

Table 4-8 TAA001 Y-axis sensor Charge response

	Voltage mV/g	Capacitance 28.891 nF	Charge pC/g
X 50g	1.451e-12 -1.145e-12		0.000 0.000 37.50e-12
Y 50g Sensitive	0.168 -0.168		2.419 -2.419 4.838
MathCAD	0.165	29.458	4.873
Z 50g	-0.112e-3 -0.112e-3		-0.002 -0.002 0.000
ALL 50g	0.167 -0.168		2.418 -2.421 4.838

Table 4-9 TAA001 Z-axis sensor Charge response

	Voltage mV/g	Capacitance 7.252 nF	Charge pC/g
X 50g	0.151e-9 -0.151e-9		0.000 0.000 1.098e-9
Y 50g	7.834e-12 -7.957e-12		0.000 0.000 57.26e-12
Z 50g Sensitive	0.759 -0.758		2.752 -2.748 5.500
MathCAD	0.704	7.643	5.380
ALL 50g	0.759 -0.758		2.752 -2.748 5.500

Table 4-10 TAA002 Connected as a Y-axis sensor Charge response

	Voltage	Capacitance	Charge
	mV/g	19.803 nF	pC/g
X 50g	10.75e-12		0.000
	-10.70e-12		0.000
			0.212e-9
Y 50g Sensitive	0.430		4.261
	-0.427		-4.223
			8.485
MathCAD	0.404	20.651	8.337
Z 50g	1.929e-3		0.019
	1.929e-3		0.019
			0.198e-9
ALL 50g	0.430		4.261
	-0.427		-4.223
			8.485

Table 4-11 TAA002 Connected as a Z-axis sensor Charge response

	Voltage	Capacitance	Charge
	mV/g	19.803 nF	pC/g
X 50g	0.392e-9		0.000
	-0.393e-9		0.000
			7.767e-9
Y 50g	12.86e-12		0.000
	-12.91e-12		0.000
			0.255e-9
Z 50g Sensitive	0.992		9.826
	-0.997		-9.869
			19.695
MathCAD	0.915	20.651	18.891
ALL 50g	0.992		9.826
	-0.997		-9.869
			19.695

Table 4-12 TAA003 Z-axis sensor Charge response

	Voltage	Capacitance	Charge
	mV/g	12.022 nF	pC/g
X 50g	0.117e-9		0.000
	-0.117e-9		0.000
			1.408e-9
Y 50g	64.43e-12		0.000
	-64.78e-12		0.000
			0.777e-9
Z 50g Sensitive	0.475		2.853
	-0.474		-2.849
			5.702
MathCAD	0.446	12.399	5.533
ALL 50g	0.475		2.853
	-0.474		-2.849
			5.702

Table 4-13 TAA001 Y-axis sensor Charge response. 2um offset

	(mV/g)		(pC/g)
X 50g	0.128e-6		0.000
	0.082e-6		0.000
	Cross axis	0.000%	0.670e-6
Y 50g	0.167		2.411
	-0.168		-2.421
	Reduction in sensitivity	0.138%	4.832
Z 50g	-74.2e-6		-0.001
	-154.5e-6		-0.002
	Cross axis	0.024%	0.001
All 50g	0.167		2.408
	-0.168		-2.422
			4.830

Table 4-14 TAA001 Z-axis sensor Charge response. 2um offset

	(mV/g)		(pC/g)
X 50g	-0.914e-3		-0.003
	-1.420e-3		-0.005
	Cross axis	0.033%	0.002
Y 50g	0.210e-3		0.001
	-0.220e-3		-0.001
	Cross axis	0.028%	0.002
Z 50g	0.757		2.745
	-0.756		-2.741
Reduction in sensitivity		0.242%	5.486
All 50g	0.755		2.739
	-0.757		-2.744
			5.483

Table 4-15 TAA002 Connected as a Y-axis sensor Charge response. 2um offset

	(mV/g)		(pC/g)
X 50g	0.2491e-6		0.000
	0.1167e-6		0.000
	Cross axis	0.000%	1.311e-6
Y 50g	0.425		4.205
	-0.430		-4.257
Reduction in sensitivity		0.272%	8.461
Z 50g	2.782e-3		0.028
	1.038e-3		0.010
	Cross axis	0.204%	0.017
All 50g	0.427		4.232
	-0.429		-4.247
			8.479

Table 4-16 TAA002 Connected as a Z-axis sensor Charge response. 2um offset

	(mV/g)		(pC/g)
X 50g	-0.774e-3		-0.008
	-1.597e-3		-0.016
	Cross axis	0.041%	0.008
Y 50g	38.3e-6		0.000
	-37.6e-6		0.000
	Cross axis	0.004%	0.001
Z 50g	0.990		9.798
	-0.994		-9.841
Reduction in sensitivity		0.283%	19.639
All 50g	0.988		9.782
	-0.995		-9.848
			19.630

Table 4-17 TAA003 Z-axis sensor Charge response. 2um offset

	(mV/g)		(pC/g)
X 50g	-0.126e-3		-0.001
	-0.497e-3		-0.003
	Cross axis	0.039%	0.002
Y 50g	-0.125e-3		-0.001
	-0.497e-3		-0.003
	Cross axis	0.039%	0.002
Z 50g	0.473		2.843
	-0.472		-2.840
Reduction in sensitivity		0.334%	5.683
All 50g	0.472		2.837
	-0.473		-2.841
			5.679

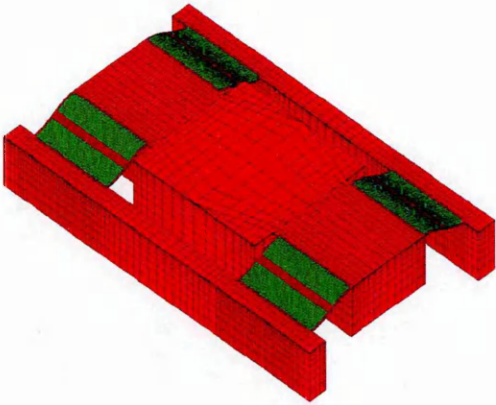


Figure 4-1 FE model of Z-axis sensor TAA001

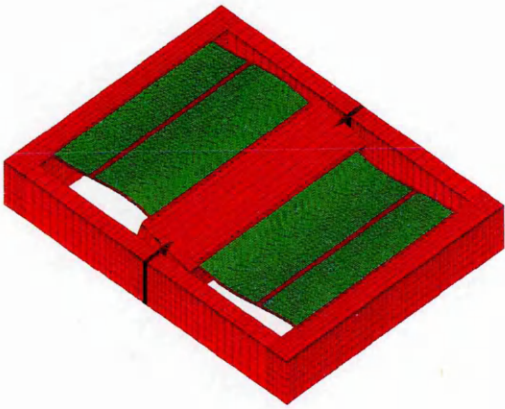


Figure 4-2 FE model of X- or Y-axis sensor TAA001

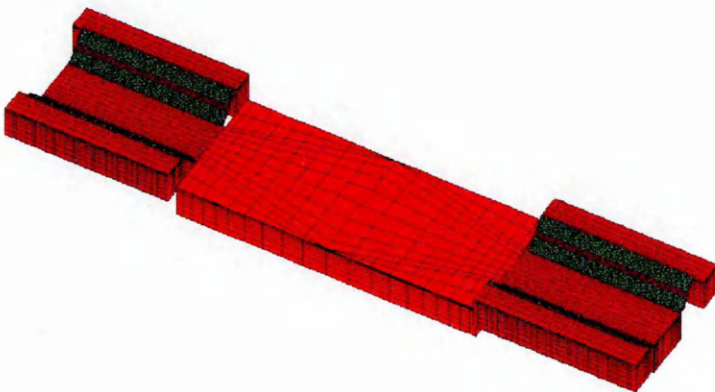


Figure 4-3 FE model of High output Z-axis sensor (Oversize) TAA002

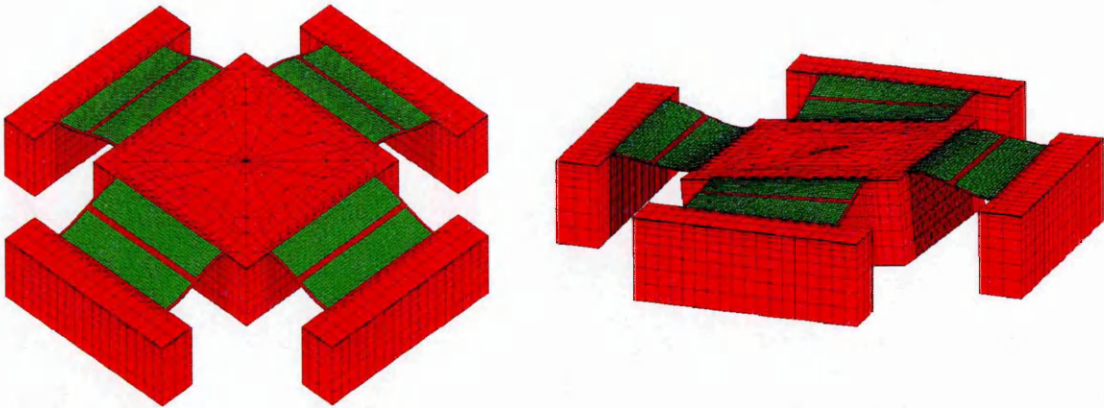


Figure 4-4 FE model of Z-axis sensor TAA003

Z-axis resonance is on-axis, as assumed in the mathematical model, but the in-plane resonance is at approximately 40° to the direction of the beams.

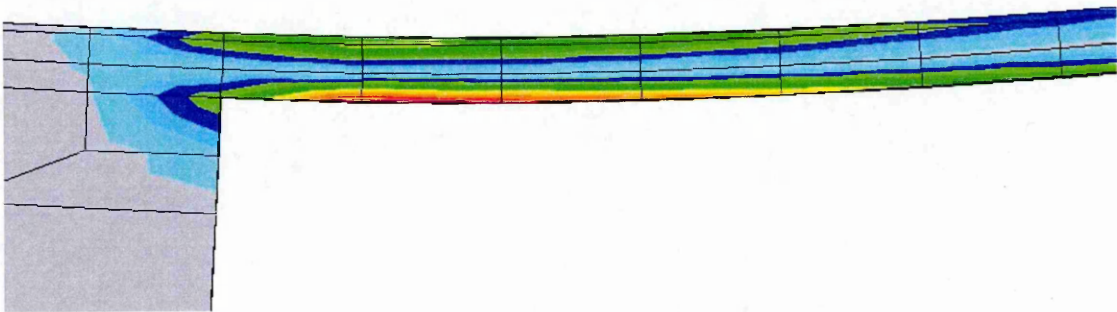


Figure 4-5 Stress distribution in a deformed beam

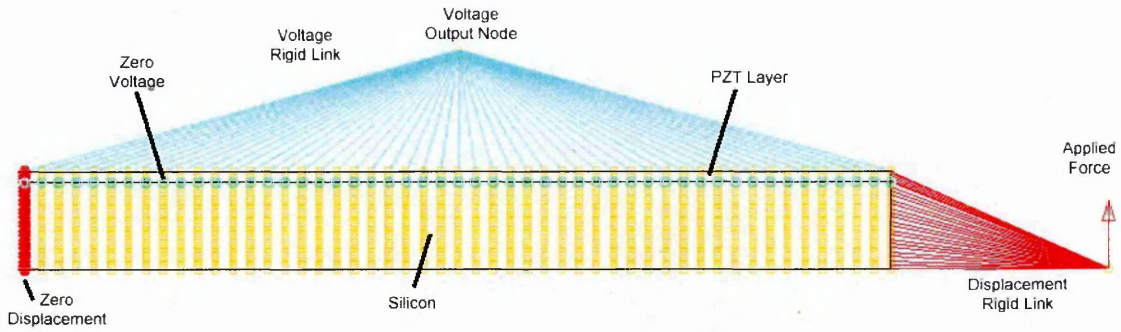
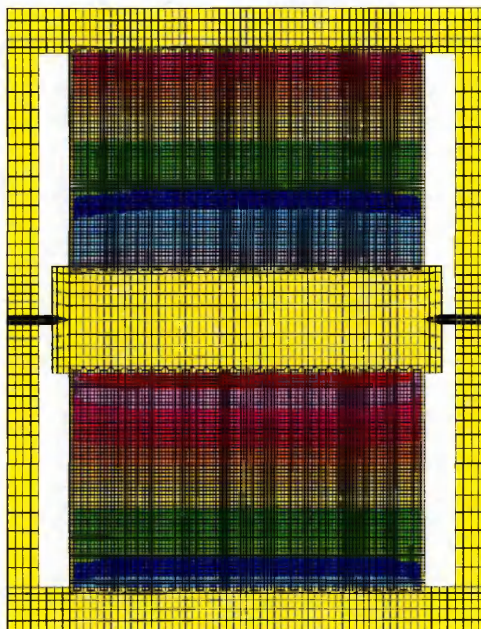


Figure 4-6 FE model for validating beam element aspect ratio

Screen shot of the high accuracy model, showing displacement constraints and the applied force in red, voltage constraints in blue, and the boundaries of each material in black.

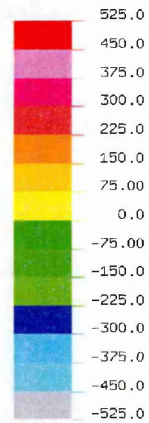
DISPLAY III - GEOMETRY MODELING SYSTEM (11.0.0) PRE/POST MODULE



VOLTAGE

VIEW :-5.245E+10
RANGE: 5.245E+10

(Band * 1.0E8)



EMRC-NISA/DISPLAY

AUG/13/02 10:11:22

ROTX
180.0
ROTY
0.0
ROTZ
0.0



MODE NO. = 1 FREQUENCY = 5.55165E+03 Hz
X-Y MODEL - PART PZT ONE ELECTRODE

Figure 4-7 Voltage generation from Y-axis acceleration

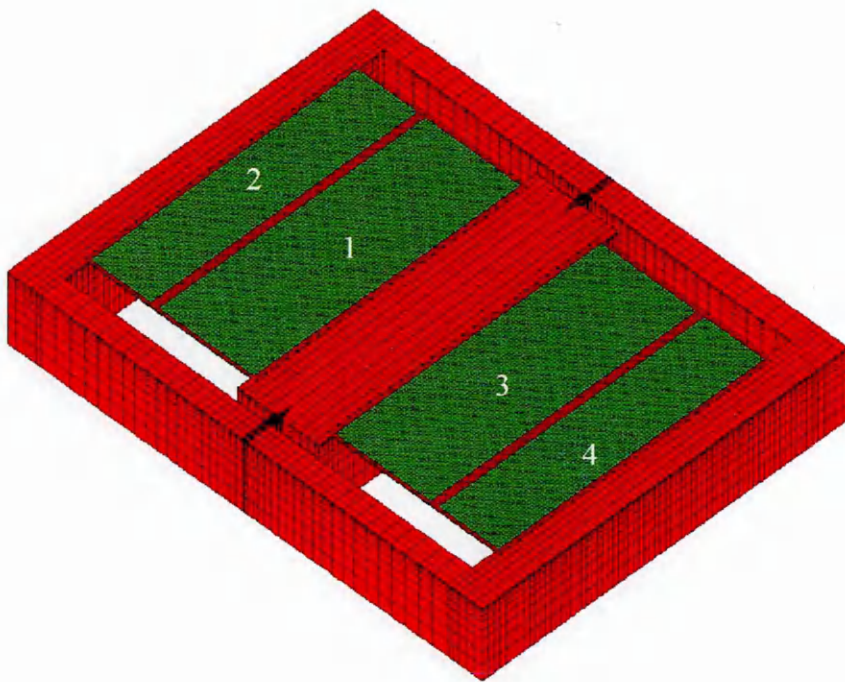


Figure 4-8 TAA001 Electrode numbering

5. Prototype Manufacturing

5.1. Physical prototype Fabrication

The work by Kunz²³ describes the basic fabrication route used to manufacture the accelerometer wafers. Development of this fabrication route, and fabrication of all the devices tested was undertaken at Cranfield University, primarily by Ming Yu Lim, with contributions from Meiling Zhu, Rob Wright and Paul Kirby. The full details are recorded in the PhD thesis from Ming Yu Lim 2004, and are beyond the scope of this thesis, so only the most influential points are noted here.

A set of four prototype devices have been designed and analysed in Chapters 3 and 4. Of these devices, drawing TAA001 is the primary interest since it forms a complete three-axis sensor. These were fabricated and tested, and some of the TAA001 devices have also been packaged. In order to reduce the number of processes involved in the fabrication of prototype devices, two simplifications were introduced. Individual dies were separated from the wafer by the through-wafer DRIE processing, eliminating the need for a separate sawing process. This also avoids exposure to vibration, cutting lubricant and debris, which are usually encountered during wafer dicing. Secondly, the wafers were fabricated without covers. This reduced the number of masks required and the number of wafers handled. It also eliminated the wafer bonding, required to attach covers, but left the devices vulnerable to mechanical damage from handling.

There are a number of areas where the fabrication has not followed the detail exactly as envisaged when constructing the model. This is due to a combination of lack of knowledge of the fabrication process and some difficulties encountered during fabrication. Since the modelling is intended to provide a tool for the development of the accelerometer design, it was considered essential to feed back information from the practical prototypes into the models.

The physical devices described in this Chapter were made from either 300-micron SOI wafers with 8-micron device layer, or 500-micron SOI wafers with 8-micron device layer. The mathematical models were recalculated using these dimensions, to predict the behaviour due to the reduced proof masses.

5.2. Sensor Fabrication Issues

5.2.1. Oversize DRIE on the handle wafer

On all the wafers processed, it was noted that the DRIE on the Handle wafer layer was 20 to 30 μm oversize, resulting in a lip of device layer silicon (8-micron thick) protruding at the base of the handle silicon. This is clearly visible in Figure 5-1⁴⁰ around all through holes in the die. The origin of this dimensional deviation lies within the fabrication process, so has been left for others to investigate. The objective here is to analyse the effect of this change to the design, such that the performance of the prototype can be compared to the theoretical predictions.

The over-etching increases the length of the beams, and reduces the mass. In Figure 5-1 it can be seen that the walls are vertical as desired, but the etching of the handle wafer is larger than the front side. The effects on the three-axis die (TAA001) and the single Z-axis design (TAA003) have been calculated in Table 5-1. It should be noted that the first wafer processed was 300 microns thick, not 525 microns as used in the original design calculations, due to limited availability of suitable SOI wafers. This was calculated to reduce Z-axis signals by 43%, and in-plane signals reduce by 67%.

Due to the significant increase in the length of the end beams, revised calculations show X and Y-axis devices on the tri-axial TAA001 die decrease the resonant frequency in the unwanted cross-axis directions by around 50%. The reduction in sensor beam stiffness is almost balanced by the reduction in mass, resulting in an increase of the lowest resonant frequency of 2%, to 9.4kHz in the desired direction. X and Y-axis signal strength is decreased by 7% to 1.6pC/g, whilst the z-axis component of cross-axis sensitivity increases to 0.3pC/g, a factor of 3. However, the cross-axis signals should be self-cancelling, due to the symmetry of the design. The effect on the TAA001 X-axis end beams is that they would be more flexible than expected, and would be able to withstand 60% greater displacement of the proof mass before failure (1.3 μm as opposed to 0.8 μm).

For the Z-axis device on the TAA001 die, resonant frequencies are decreased by about 10%, with the lowest resonance at 5.8kHz, in the Z direction as desired. Z-axis signal strength is reduced by 4% to 3.0pC/g, whilst the cross-axis signal decreases by 8% to 0.7pC/g. Again, the cross-axis signals are self-cancelling, due to the symmetry of the design.

The effect on the single Z-axis design (TAA003) has also been calculated. Resonant frequencies are reduced by about 6%, with the lowest resonance at 6.0kHz in the Z-axis direction. The signal strength in the Z-axis is reduced to 3.1pC/g, about 6%.

It should be noted that with the over-size etching, the sensor electrodes are no longer located over the most highly strained areas of PZT, at the extreme ends of the beams. This is the main reason for the reduction in signal strength.

5.2.2. Buried Oxide Layer etching sequence

The final stages of fabrication for the accelerometer were planned to be DRIE of the handle wafer, then RIE of the buried oxide layer. Since the etching will cut completely through the wafer, it must be mounted onto a carrier wafer. This is achieved using photo-resist as an adhesive layer between the device wafer and the carrier. DRIE is used to etch the handle wafer, then RIE to etch the buried oxide, before washing away the photo-resist using acetone solvent.

During the RIE stage, it was noted that most of the end beams on the TAA001 devices had broken. Investigations were run into the effect on the structure of pressure differences introduced during processing (if the photo-resist adhesive layer was incomplete). Whilst this is a possible mechanism, the investigation proved inconclusive.

The fabrication sequence was modified, so that the buried oxide layer was etched from the front of the wafer, before the main DRIE through-etch. Whilst this did not resolve the broken structures, it indicated that they were not due to the RIE vacuum, and focused attention on the stresses in the layers deposited on the beams: silicon oxide, platinum electrodes and PZT. Investigation then centred on the layer-stress distribution.

5.2.3. Effect of stress in the PZT and Platinum electrodes

An alternative explanation for the failure of the end beams was the inherent stresses in the accelerometer structure causing distortion when the buried oxide layer is removed. When the SOI wafer is created, and the PZT and electrodes are deposited, each layer interacts with the previous one. Slight mismatching of the crystal lattice structure and coefficient of thermal expansion between layers causes stresses⁴¹. These can be influenced by the details of the method of deposition, and may be relieved by annealing the structure.

Part of the manufacturing process for the SOI wafers is to monitor and try to control the stresses between layers, so that they are balanced through the thickness and result in a relatively flat wafer. When the bottom platinum electrode is deposited, it is under compressive stress, causing convex curvature of the wafer, but this may be annealed out during the PZT deposition, since this is processed at 530°C to fuse the material. The top platinum electrode is patterned by the 'lift-off' technique. It does not undergo annealing, but because of the fragmented nature of the pattern, the layer stresses are expected to be partially relieved. The PZT is under a slight compressive stress, but the affect of this is amplified by its relatively large thickness.

When the layers are patterned to create the proof mass and beams, sections of the handle wafer are removed. At the start of the RIE process the beams consist of complete layers of: buried oxide– 1.5µm, device silicon– 8.0µm, front field oxide– 0.3µm, bottom platinum electrode – 0.1µm, PZT film – 1.0µm, and the patterned top electrode – 0.1µm. The beams are much more susceptible to the effects of stress than the complete wafer,

since 98% of the thickness has been removed. General deformation of the beams into a dome shape was observed on the fabricated samples.

The significant stresses were understood to be in the PZT and platinum electrode (compressive stress of 800- 2300MPa), and the buried oxide layer (also compressive stress, but not quantified). When the buried oxide is removed, it was predicted that the beams would be deformed by the stress in the top electrode, only present on the sensor beams.

Calculation of the deformation due to 800MPa stress in the top electrodes shows that the proof-mass would be displaced vertically by around 0.3 μm . 2300MPa would displace the proof-mass by 0.83 μm . The higher displacement is sufficient to reach the fracture strength of between 800MPa⁴² and 2000MPa⁴³ within the silicon of the end beams.

The electrode stress values quoted by Cranfield equate to 0.5 to 1.5% strain in the Platinum. These values are very high compared to the expected internal stress values quoted in the public domain⁴⁴, but there are two possible explanations. The electrodes are deposited at a relatively high rate of 1.7nm/sec, and the crystal lattice mis-matching between the layers. Internal stress values for thin platinum films, deposited onto <100> Silicon at varying rates have been measured⁴¹ as 185-275MPa (0.1nm/sec) to 739-955MPa (0.7nm/sec).

Finite element modelling, based on 20MPa stress in the composite PZT/Platinum layer, and 25MPa in the buried oxide layer, has shown the beam stresses to be significant. A number of load-cases were run with and without the buried oxide, to demonstrate the effect of the buried oxide layer in balancing stresses. The outcome is that without the buried oxide layer, the beam models exhibit slight arching, with a pronounced downward curve at their free edges, deforming by up to a micron. This correlates with the deformations noted under microscopic examination of the dies. Models with the buried oxide layer on the back of the beams reduced the deformation due to stress between layers by a factor of 10. The maximum stress was not significantly affected by the presence or absence of the buried oxide layer. The results of the FE investigation are summarised in Table 5-2. Subsequent fabrication work retained the buried oxide layer on the beams, since the layer stresses are balanced, even though they are not eliminated.

5.2.4. Effect of PZT layer thickness

The thickness of the PZT layer as deposited was 1.3-1.4 μm rather than 1.0 μm as designed. The influence of the PZT and oxide layer thickness was investigated for the projected results.

From inspection of the theoretical model in Chapter 3, it can be seen that the signal strength is proportional to:

Distance from Neutral Axis to Centre of PZT film (NA-PZT)

Second Moment of Area of Beam (I_z)

The original model used the assumption that the PZT film was 1 μ m thick on the silicon beam. The platinum electrodes and surface oxide layer were ignored, since they could not be modelled in the finite element analysis. When the surface oxide, PZT and electrode layers are all considered, the beam stiffness is increased, but the distance from the neutral axis is also increased.

Beam dimensions for the three-axis in-plane sensors (TAA001 X and Y-axes) were used to calculate Table 5-3. It can be seen that based on the layer thickness values quoted by K. Kunz²³, the signal strength was 92% of the value calculated using the simplified layer structure. The actual layer thickness values fabricated by Cranfield University are slightly greater than those quoted by Kunz, and reduce the signal strength by a further 5%. Trends for increasing both the surface oxide layer (SiO₂) and PZT film thickness were investigated.

An increase in the PZT layer thickness increases the variance in strain through the layer. The top surface (furthest from the neutral axis of the beam) will be strained more than the bottom surface, so the top surface should be generating more charge. However, the affect of film thickness on charge distribution through the PZT film has not been investigated. It is assumed that the charge will distribute evenly, and all calculations are based on mid-material strains.

5.2.5. Poling the PZT

Trials were conducted to evaluate the poling of the thin film PZT, which forms the functional sensing element in the accelerometer. These trials were based on information from Cranfield University, outlining their previous experience in poling thin film PZT. The PZT is polarised by applying a dc voltage between the top and bottom electrodes, whilst the material is heated. The objective was to establish temperature, voltage and time requirements to achieve poling, together with a process cycle for poling multiple sections of a sensor in a time effective manner.

To maximise the charge signal from the accelerometer, it is proposed to polarise the segments of each accelerometer in opposing directions, as shown in Figure 5-2. The output connection from each individual accelerometer (X, Y, or Z-axis) is achieved by connecting all of the top electrodes on one accelerometer together to form one input to an amplifier, and the bottom electrode of the same accelerometer to the other amplifier input.

Discussions with staff and researchers at Cranfield University have indicated that the sol-gel PZT is partially poled by the process of deposition. The crystal orientation within the PZT film is strongly influenced by the bottom platinum electrode²³, and

electrical fields are generated during the process of sputtering the top electrode and RIE etch of the PZT. It is believed that the electrical fields induce the initial polarisation. Kunz²³ describes the fabrication process, and includes an annealing stage for the top electrode by heating to 500°C for 5 minutes in O₂ to improve adhesion. This would heat the PZT above the Curie point (approximately 440°C³⁸), and should disrupt any electric-field induced poling. However, trials at Cranfield University found that this process step can cause damage to the electrodes, so it has not been adopted. The direction of initial polarisation is equal to the effect of poling with the bottom electrode earthed, and the top electrode connected to a positive DC voltage. This configuration is referred to as 'positive poling'.

Assessment of the level of poling achieved was quantified by measuring the capacitance of each segment before and after poling. Data is not available for unpolarised thin film PZT. Therefore, in order to estimate the percentage change in the capacitance readings before and after polarisation, a simple method has been derived. The average material dielectric constant quoted for bulk material from Yu and Lan²⁵ $(\epsilon_{r,11} + \epsilon_{r,22} + \epsilon_{r,33})/3$ was compared with $\epsilon_{r,33}$, the dielectric constant in the polarised direction (un-polarised material is assumed random). For the bulk material properties used in the modelling work, $\epsilon_{r,11} = \epsilon_{r,22} = 1179$ and $\epsilon_{r,33} = 730$. Thus the fully polarised dielectric $\epsilon_{r,33}$ is 71% of the average dielectric. However, the actual change in capacitance is affected by the difference in the material properties, and the natural polarisation of the material as deposited. A reduction in the capacitance value to 75% of the original was considered to signify complete polarisation.

The poling procedure was based on recommendations from Cranfield University, and correlates with the values indicated by PZT sol-gel manufacturers Inostek³⁵ and Mitsubishi Materials⁴⁵.

- Probe upper and lower electrodes of PZT section to be poled.
- Heat to 130°C on a hotplate.
- Apply 15V dc to the PZT, and hold for 10 minutes.

This was confirmed by a series of experiments, with the resultant polarisation plotted against voltage and time. The effect of the natural polarisation should be noted in Figure 5-3 and Figure 5-4, where the polarisation null point is offset from zero. In Figure 5-4, 'negative time' represents time at a negative polarisation voltage. Whilst poling in the positive direction achieves a plateau against both time and voltage, completely reversing the inherent poling does not appear to be possible.

The minimisation of cross-axis sensitivity of the accelerometer relies upon equal polarisation in all segments. The negative poling of segments is not recommended, since the direction of poling significantly affects the level of poling achieved. An alternative connection configuration is required to accommodate the poling of all segments in the same direction. This leaves the bottom electrode electrically floating,

and connects one top electrode areas to each of the amplifier inputs (signal and reference).

Since all PZT sensor elements must be polarised in the same direction, alternative methods of polarising the whole wafer can be considered. These would dramatically reduce the time required for poling, and are considered to be highly advantageous.

5.2.6. Connection of the Electrodes

In order to sense acceleration in the specified direction, each sensor is designed to maximise the desired charge signal, and self-cancel cross-axis signals. This is achieved by selecting the order of connection of the PZT elements⁴⁶.

The desired connection configuration maximised the charge signal. This is obtained by polarising the PZT elements in opposite directions, then connecting all stacks in parallel. When acceleration is applied in the sensitive direction, all the PZT elements which are in compression (inside the curvature of the beam) are polarised in one direction, and the remaining PZT elements which are in tension (outside the curvature of the beam) are polarised in the opposite direction. The electrical outputs of all PZT elements will be the same polarity, so are connected in parallel. However, this is not practical, due to the inherent polarisation of the PZT. All PZT elements are partially polarised in the same direction as a by-product of the fabrication process, and this polarisation cannot be satisfactorily reversed.

The actual electrode connection configuration is to connect the two PZT elements of each sensor in series. By polarising all the PZT elements in the same direction, the voltage signal is increased, favouring a voltage driven amplifier. The same energy is available from the displacement of charge within the PZT, but the voltage is doubled and the charge halved compared with the parallel connection. In this case, the capacitance value of the PZT elements becomes significant, since this dictates the conversion rate of charge to voltage. This configuration is easily achieved from inherently partially-polarised PZT, and allows polarisation of the whole wafer in one process step.

Direct connection of the bottom electrodes between individual sensors on the three-axis die is prevented by trench isolation of the silicon device layer, and an oxide layer beneath the bottom platinum electrodes. However, the silicon-oxide insulating layer is a dielectric, and capacitors are created by the bottom electrodes and silicon device-layer. The level of electrical coupling between axes due to this capacitance was considered, but found to be negligible.

5.2.7. Mounting of the Sensor Die

Due to the design of the accelerometer and the method of fabrication, the proof masses are flush with the back of the die. If they are to move freely, as they must for the sensor to operate, there must be a gap beneath the masses. The rear of the sensor die is covered

by the circuit board, so a 35 μ m thick copper track was patterned to support only the edges of the die.

The sensor die must be mounted sufficiently rigidly to allow accelerations to be transmitted from the board to the sensor. The adhesive must be restricted to the perimeter of the die, since excessive adhesive could bond the proof masses in place. Initially, an epoxy die attach adhesive was selected to form a strong bond to both the silicon die and the copper tracks on the PCB. However, this was cured at 120°C, and resulted in a serious thermal mismatch. The dies became compressed during cooling due to the relatively high shrinkage rate of the PCB compared to the silicon. The beams buckled out of plane due to the shrinkage of the frame, and the preload incurred prevented the sensor from operating. Following this failure, a silicone adhesive was selected. This is much more compliant, absorbing the thermal mismatch, but still appears to transmit the measured accelerations adequately. The main concern is the affect on the dynamic response of the sensor, reducing high frequency measurements, but this compliance would also provide a degree of shock resistance for the sensor die.

5.2.8. Package Design

Sensor design TAA001 is the primary interest since it forms a complete three-axis sensor. It has been packaged with the amplifier electronics to form a usable prototype sensor for general evaluation. The other sensors follow the same die fabrication route, and were used with breadboard amplifiers for laboratory investigation.

The prototype package was developed as a 25mm square to determine X and Y orientations, split through the thickness to become two halves, clamping the PCB. The halves were secured together using machine screws. Exploded views of the prototype assembly are shown in Figure 5-5 and Figure 5-6, and assembled in Figure 5-7.

This package is significantly larger than the target specification of 5mm square by 10mm long, mainly due to the use of packaged electronic components and space for screw fasteners. The size can be reduced by standard electronic miniaturisation techniques, such as using bare-die amplifiers and printed thick-film resistors, once the design has been proven. Evaluation of the prototype assemblies will validate the theoretical modelling, and guide the design of the production sensors.

The sensor packages had been designed and made with charge amplifiers before making the findings on poling of the PZT. It was decided to continue with the charge amplifiers, despite the reduced charge signals, in order to discover what other issues might be contained within the accelerometer assembly design. The charge amplifier comprises of an op-amp based integrating amplifier, with capacitive feed-back. In order to maintain the low frequency response desired, a 1G Ω feedback resistor was required, together with very low input bias current op-amps. This circuit converts a very high impedance input to a low impedance output, with unity voltage gain. The high impedance input circuits are very susceptible to interference, so must be electrically screened. This is

achieved with the aluminium package. The low impedance output is electrically robust, allowing transmission of the signal without undue noise generation, retaining the resolution desired.

Thanks must go to Paul Towers and Ian Braithwaite for their assistance on the electrical circuit design. The circuit is shown in Figure 5-8.

5.3. Practical implications on the models

A number of practical fabrication issues have affected the performance of the sensor, and the expected performance has been re-calculated based on them.

It was noted that the DRIE etching of the back of the wafer was over-size by $20\mu\text{m}$. This is predicted to reduce signal strength by 6 to 8%. Over-etching of the handle DRIE also increases the length of the end beams for the X and Y-axis sensors. The out-of-plane stiffness of these beams is reduced by 35%, allowing more vertical displacement of the proof mass, and consequently more cross-axis signal. Changes in resonant frequencies due to the etching variance are not considered sufficient to compromise the overall performance of the sensor.

Increasing the thickness of the surface oxide layer (SiO_2 between the silicon of the beams and the PZT elements) to $0.3\mu\text{m}$ and PZT film to $1.3\mu\text{m}$ has reduced the expected signal strength by 5%. The change in thickness of the PZT film has a proportionately larger effect than the change in the surface oxide layer thickness.

The fabrication sequence has been changed to etch the buried oxide layer from the front of the wafer, leaving the oxide on the back of the beams. Figure 5-2 shows the original wafer construction, with the buried oxide layer shown in black, removed from the back of the beams. Retaining the buried oxide layer on the beams balances the stresses between the beam layers, visibly reducing the distortion at the edge of the beams and increasing the yield of sensors complete with their end beams. The oxide layer has increased the beam thickness by $1.5\mu\text{m}$, so the expected signal strength is reduced by a further 17% and the resonant frequency predictions increased by 15%.

The greatest reduction in signal strength was due to inherent poling of the PZT. The PZT must all be polarised in one direction, so the two PZT sensors on each accelerometer must be connected in series. This reduces the signal charge by 50%, and doubles the signal voltage. The original choice of charge amplification, as used in Chapter 6.3, becomes questionable, and alternative electronic amplification should be investigated.

Overall, the variations between the theoretically optimised design and the physical prototype dies reduced the calculated signal from 5pC/g to 1.8pC/g on each axis.

Table 5-1 Effect of 20µm over-size on the DRIE rear-side etching.

Device	TAA001 X-axis or Y-axis			
	525um wafer to Design drawing	300um wafer to Design drawing	300um wafer with 20µm over etch	Over-etch effect
Mass (mg)	1.615	0.953	0.874	91.7%
Natural resonant frequencies				
f 0x	5066	9241	9442	102.2%
f 0y	20546	28516	13046	45.8%
f 0z	18025	23457	16039	68.4%
Charge Generation before Self-cancelling				
sqx	4.873	1.699	1.579	92.9%
sqy				
sqz	0.180	0.107	0.316	295.3%

Device	TAA001 Z-axis			
	525um wafer to Design drawing	300um wafer to Design drawing	300um wafer with 20µm over etch	Over-etch effect
Mass (mg)	3.592	2.121	2.05	96.7%
Natural resonant frequencies				
f 0x	6834	9227	8272	89.7%
f 0y	7309	11591	10846	93.6%
f 0z	5043	6563	5833	88.9%
Charge Generation before Self-cancelling				
sqx				
sqy	2.217	0.773	0.715	92.5%
sqz	5.381	3.177	3.044	95.8%

Device	TAA003 Z-axis only			
	525um wafer to Design drawing	300um wafer to Design drawing	300um wafer with 20µm over etch	Over-etch effect
Mass (mg)	2.398	1.416	1.336	94.4%
Natural resonant frequencies				
f 0x	6856	10197	9650	94.6%
f 0y	6856	10197	9650	94.6%
f 0z	5027	6542	6032	92.2%
Charge Generation before Self-cancelling				
sqx	1.473	0.513	0.472	92.0%
sqy	1.473	0.513	0.472	92.0%
sqz	5.533	3.267	3.065	93.8%

Table 5-2 FE results for stress between layers

Thermal model equivalent to 20MPa in PZT stack and 25MPa in Buried Oxide

	a	b	c	d	e
PZT thickness	1.8 μm	1.0 μm	1.0 μm	1.8 μm	1.8 μm
BOX thickness	2.0 μm	2.0 μm	2.0 μm	1.5 μm	1.5 μm
BOX on beams	Yes	No	Yes	Yes	No
Deformations (nm)					
Centre of beam	-13	134	-76	34	198
Edge of beam	85	-773	593	-208	-1277
Arch of Mass	20	10	17	34	14
Maximum Stress (GPa)					
Pivot Beams	42.3	41.5	42.5	43.2	40.7
Main Beams	42.7		47.5	43.0	43.7

Table 5-3 Effect of beam construction on beam stiffness and signal strength

	Layer thickness (μm)		
	Si / PZT	Kunz dims	Actual dims
Pt	0	0.1	0.1
PZT	1	1	1.3
Pt	0	0.1	0.1
SiO ₂	0	0.1	0.3
Silicon	8	8	8
I_z (10^{-9}m^4)	102	113	125
NA to mid PZT	4.27	4.34	4.55
NA-PZT / I_z	0.0419	0.0384	0.0364
Signal strength	100%	92%	87%

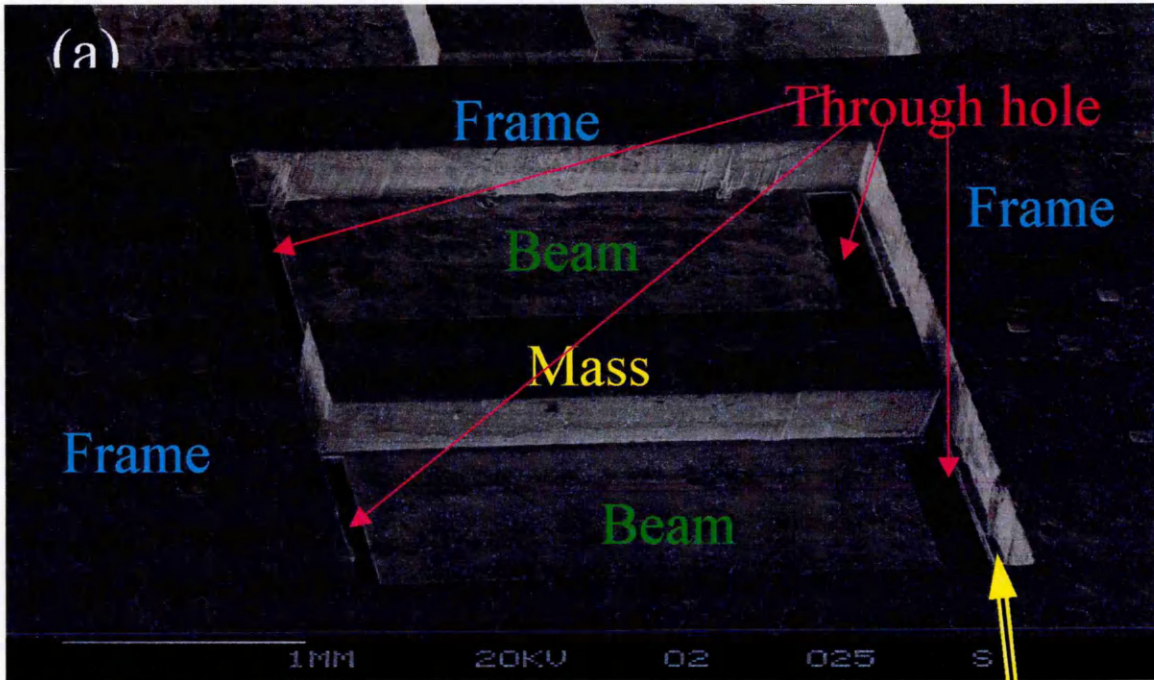


Figure 5-1 SEM photograph from the rear of wafer 1 showing DRIE under-cut
 The etched wall should be in-line with the Through hole edge.

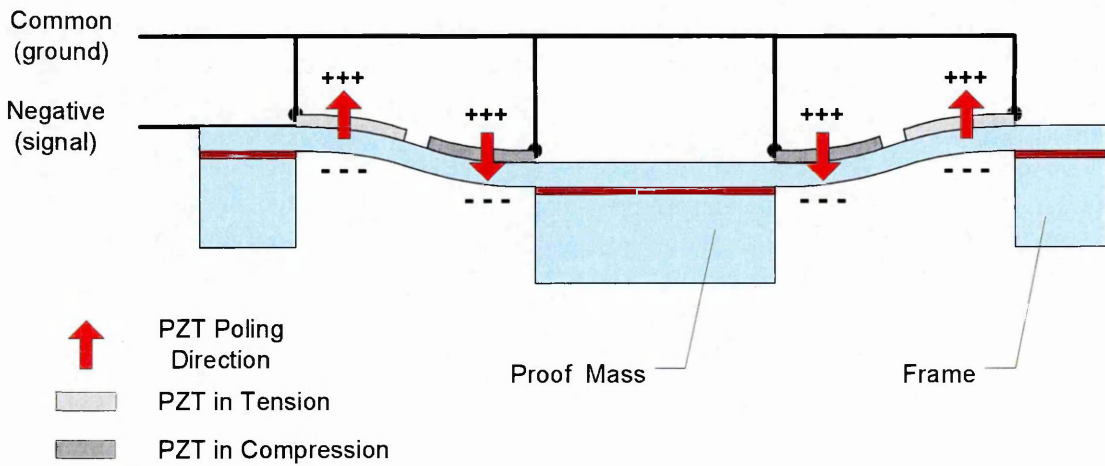


Figure 5-2 Poling direction and Electrical Connections for Sensing

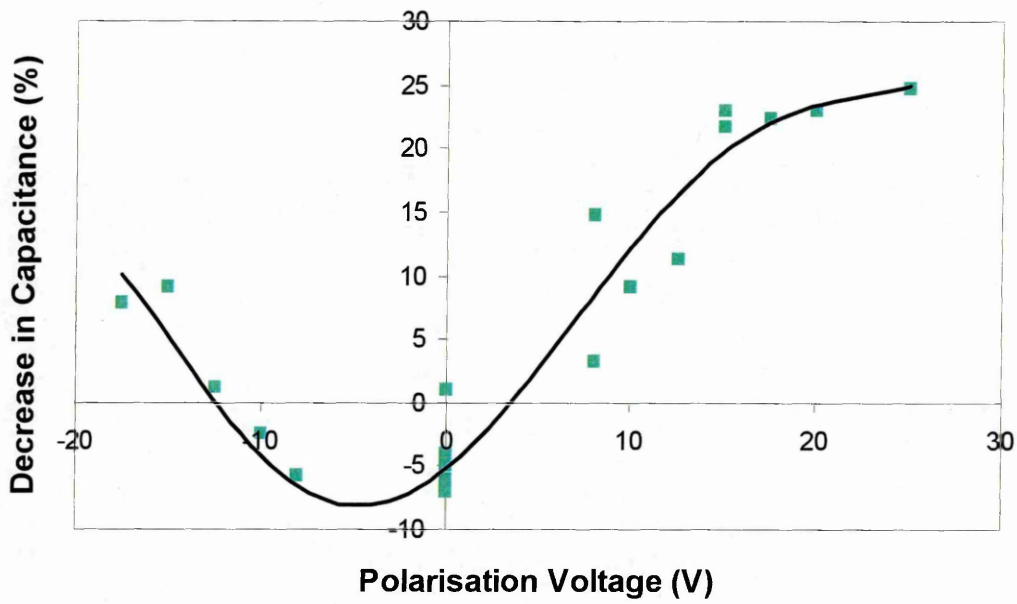


Figure 5-3 Graph of Change in Segment Capacitance against Polarisation Voltage
 Poling at 125-140°C for 10 minutes

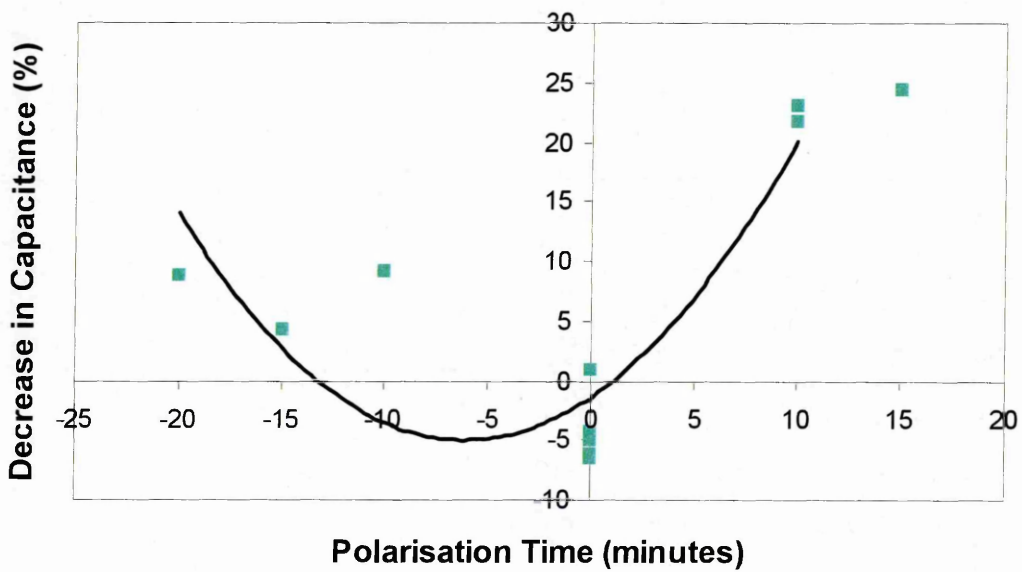


Figure 5-4 Graph of Change in Segment Capacitance against Polarisation Time
 Poling at 125-140°C and 15V. Negative time indicates negative poling voltage.

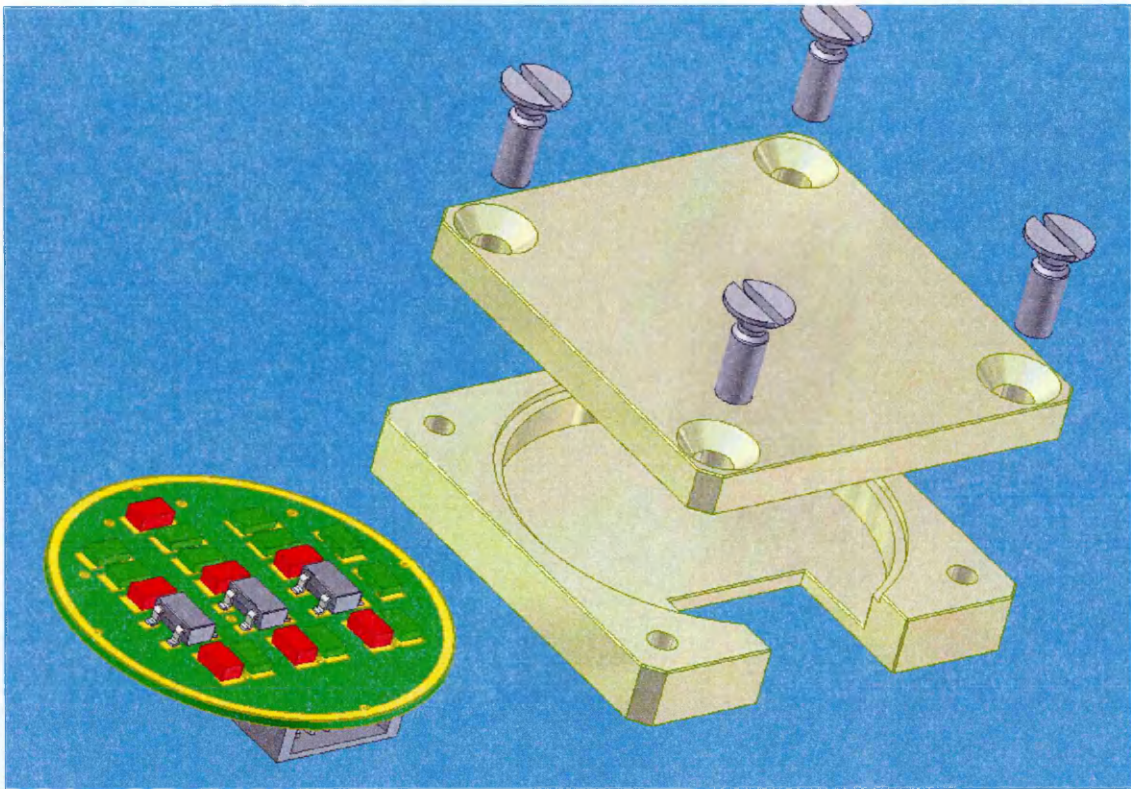


Figure 5-5 View of Prototype PCB (amplifier side) and Package

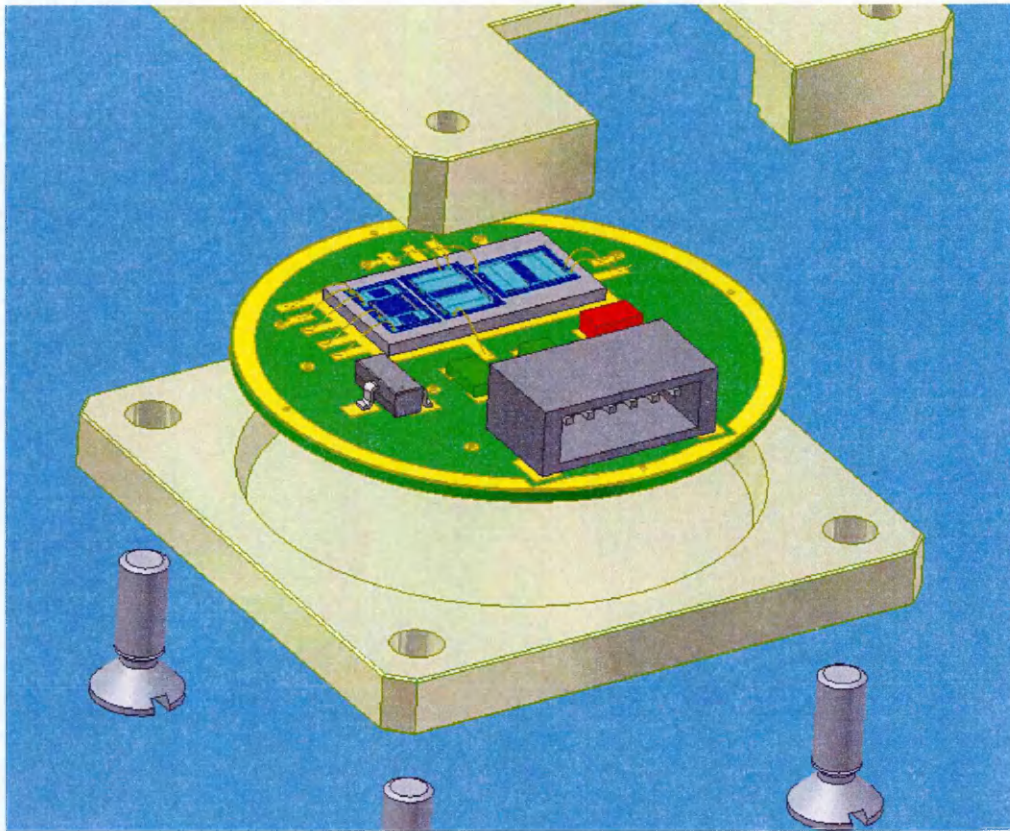


Figure 5-6 View of Prototype Accelerometer - Sensor Side

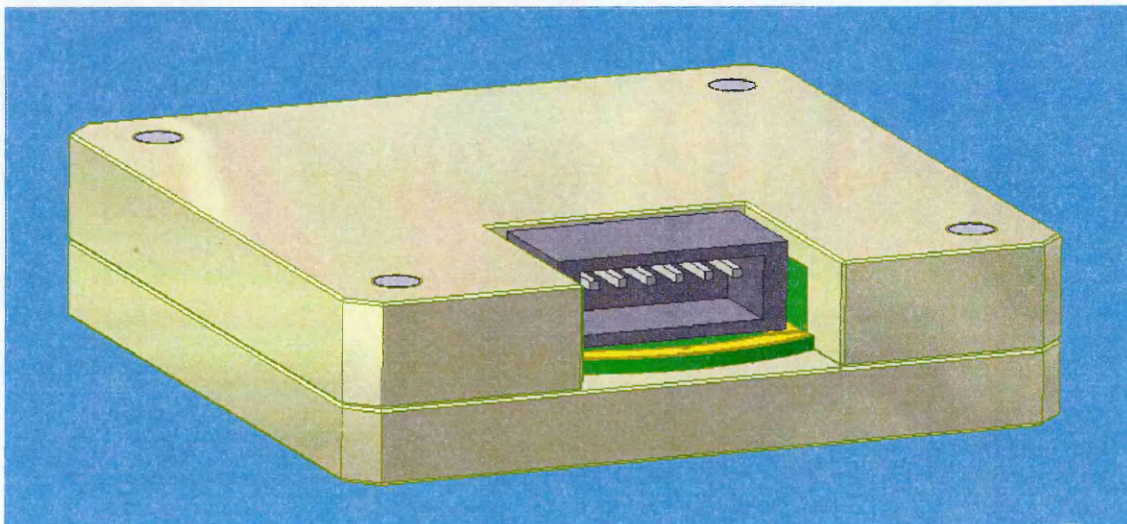


Figure 5-7 Assembled Prototype Accelerometer and Package

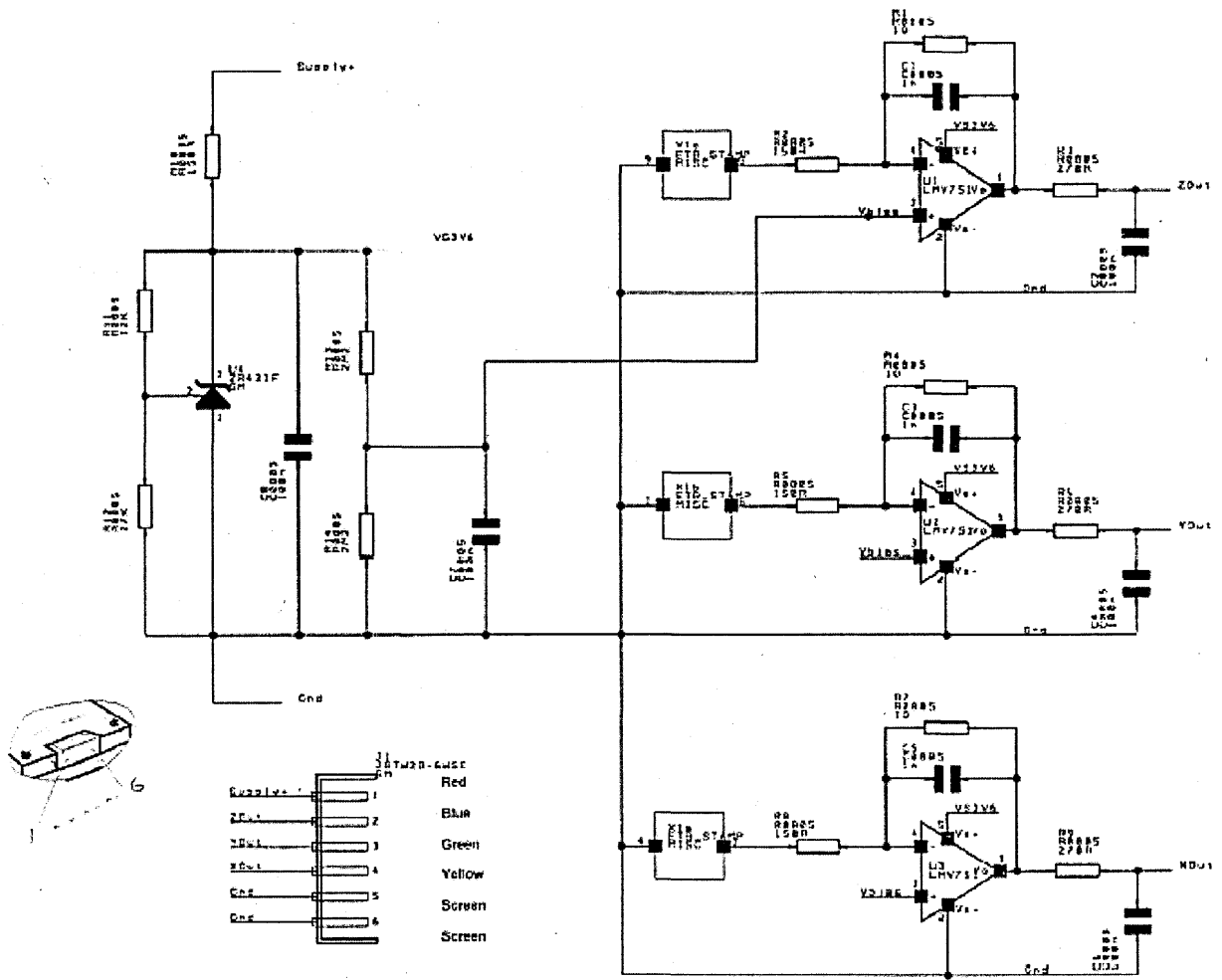


Figure 5-8 Prototype Accelerometer Package Circuit Diagram

6. Analysis of the Test Results

6.1. Test Objectives

The testing of the accelerometer prototypes falls into two categories: bare die testing; and laboratory characterisation of the accelerometer assembly, including amplification.

The first objective is to verify the electrical continuity and capacitance of each sensor, then to assess the electro-mechanical coupling integrity of the sensor die, and ensure that the structure is functioning generally as expected.

The second objective of the testing is to characterise the prototype sensor and electronics such that quantified sensor systems can be manufactured. Whilst evaluating the prototype devices, the compromises required for their manufacture must be considered. Changes to the fabrication process are required for production scale manufacture, and through evaluation of the prototype devices it is hoped to be able to interpret if these changes will benefit or detract from the intended design.

6.2. Bare die testing

6.2.1. Sensor capacitance

The capacitance of each sensor was measured as an assessment of the continuity of the electrodes, and dielectric property of the PZT. The dielectric strength changes when the PZT is poled, so can be used as an indication of the state of poling.

The theoretical capacitance values were based on 52/48 composition PZT with dielectric constant $\epsilon_{33}=6.46 \times 10^{-9}$ F/m. These values were 7.36nF for the x and y-axis sensors, and 1.91nF for the z-axis sensor on dies made to drawing TAA001 with 1 μ m of PZT. In practice, the PZT was deposited at 1.3 μ m thick, reducing the expected capacitance by the reciprocal of the thickness to 5.66nF and 1.47nF respectively.

The actual capacitance values measured were consistently around 3.6nF for x and y-axis sensors, and 1.0nF for the z-axis, approximately 2/3 of the predicted values. The derived dielectric value for the 30/70 composition PZT actually used $\epsilon_{33}=4.1 \times 10^{-9}$ F/m.

6.2.2. Device isolation

There is a capacitive coupling between axes, due to the parasitic capacitances in the die and the PCB. These have been measured, to allow estimation of this component of cross-axis noise.

Each sensor effectively comprises of two piezo-electric capacitors. The sensors are connected such that one top electrode is earthed, and the other provides the signal output. The bottom electrode of each device is allowed to float, but is expected to be at approximately half the signal voltage.

The individual sensors are trench isolated by patterning through the device silicon layer, but are capacitive coupled. The bottom electrodes form capacitors with the handle layer silicon, using the front surface oxide and buried oxide layer as dielectric. The device silicon layer forms an intermediate electrode of no great consequence. The theoretical capacitance is calculated as 54pF per sensor, using the area of the bottom electrode and the oxide thickness (2.85mm^2 , $0.3\mu\text{m}$ and $1.5\mu\text{m}$ thick, $\epsilon_r=3.82$). Two such capacitors are connected in series to couple the sensors, giving an effective value of 27pF. In practice this is marginally reduced, since there is also some resistance through the silicon.

Die capacitance between X and Y-axes was measured using a Wayne Kerr component analyser at Cranfield University. The value obtained was 24.4pF, with a $\tan\delta$ value of 0.025. This compares accurately with the theoretical value above, derived in Appendix 6. Capacitive coupling of the PZT sensors is small compared to the capacitance of the actual sensors, typically 3.6nF per axis. Cross-axis noise is related to the relative values of these two capacitors, so there is a separation factor of 250, the cross-axis coupling due to parasitic capacitance is expected to be 0.4%.

6.2.3. Drive and pick-off

Testing the bare die sensor allows the mechanical structure to be assessed independently from the electronic amplifiers. The bare sensor die can be driven from a signal generator, using part of the PZT sensor element as an actuator. The piezo-electric properties can be measured, since they affect both the driving efficiency and the response signal, and the resonant frequencies of the structure can be used to assess mechanical integrity.

The resonant frequencies of the three-axis die were investigated by driving the PZT. A signal generator was connected to one set of top electrodes, using the bottom electrode as earth. The signal was 1V peak to peak, with frequencies from 50Hz to 15kHz. An oscilloscope was connected with one channel measuring the signal generator drive and the other measuring the inner electrode pick-off signal. The flat response is 1.72mV-peak X-axis, 1.44mV-peak Y-axis, and 3.04mV-peak Z-axis for 500mV-peak driving signal. There are two stages of piezoelectric coupling coefficient, where electrical

energy is converted to mechanical energy, transmitted through the structure, then returned to electrical energy by the second piezoelectric stack. By comparison of the input and output signals, the coupling coefficient for this structure can be derived as 5.5% efficient for the in-plane sensors and 7.8% efficient at each stage for the z-axis.

At resonance, the pick-off signal increases significantly and the relative phase of the drive and pick-off changes from in-phase below resonance, through 90° phase lag at the resonant frequency to anti-phase above resonance. This phase relationship behaviour can help to identify resonant frequencies in the structure, but they can also be identified directly due to the increased amplitude of the response. The X and Y-axes resonate around 10kHz, as shown in Figure 6-1. These frequencies should be identical but differ by 2% due to fabrication variances. They were also 50% higher than predicted, and this is believed to be due to stresses in the PZT and electrode layers causing deformation of the beams into shallow domes, as could be clearly seen under a microscope. For the Z-axis sensor, the first resonance was at 5330Hz, with 3dB points at 5310 and 5350Hz, giving a quality factor $Q \approx 130$. This indicates minimal damping of the motion, as would be expected from the large clearances. A second resonance was observed at 7550Hz, and comparison with the theoretical models indicates that this is from the in-plane resonant mode. The Z-axis values compare 10% higher than the model predictions, indicating less stress induced stiffening on beams of smaller area.

	Theoretical		Measured	
	Peak 1	Peak 2	Peak 1	Peak 2
X	6670 Hz	18090 Hz	10160 Hz	-
Y	6670 Hz	18090 Hz	10370 Hz	-
Z	5030 Hz	6855 Hz	5330 Hz	7550 Hz

Testing the bare die by driving the PZT as an actuator allows a production characterisation test, without requiring a vibrating table. Probing of the die is greatly simplified, since the frame will remain stationary. If a shaker table is used to check the function of the sensor as an accelerometer, the probes must maintain contact throughout the vibration cycle. This is unlikely to prove satisfactory.

6.3. Laboratory characterisation

6.3.1. Sensitivity

The response from dies on the first wafer fabricated was qualitatively measured. There was significant variance between dies, up to a factor of three, and this was greater than the change in response due to poling. For some dies, there was minimal change in response due to poling, whilst others increased their response by a factor of two. Analysis of these dies showed extensive deformation of the beams, as discussed in Chapter 5.2, which was believed to be the origin of the scattered results. Further wafers

were fabricated, and the dies from these wafers produced results that are more consistent.

Testing was run by a number of facilities using the first packaged prototypes, with charge amplifier electronics. Results for the on-axis response of the accelerometer in each direction were:

	Theory	B	C	Average
X	2.44 mV/g	0.71 mV/g	0.79 mV/g	0.75 ± 0.05 mV/g
Y	2.44 mV/g	0.78 mV/g	0.79 mV/g	0.75 ± 0.05 mV/g
Z	2.69 mV/g	0.96 mV/g	1.07 mV/g	1.00 ± 0.05 mV/g

The dies from wafer three, used in the prototypes, were acceptably repeatable, but produced only about one third of the predicted charge. This is mostly due to the actual use of thin-film 30/70 PZT rather than bulk 52/48 Zirconate / Titanate ratio which was specified in the calculations. There is also an unknown contribution due to deviation in the mechanical stiffness of the structure. The derived piezoelectric charge constant for thin film 30/70 PZT is $d_{31} = -31 \times 10^{-12}$ C/N. This complements previous PZT characterisation work by Southin⁴⁷.

6.3.2. Resolution

The resolution of the sensor system is dominated by the electrical noise generated in the amplifier, cable and oscilloscope. The output of the charge amplifier is of the order of 1mV/g, and this was initially fed directly into the oscilloscope. However, the noise floor of the oscilloscope is 0.2mV, so the resolution was a very poor 0.2g. A x100 amplifier was introduced between the charge amplifier and the oscilloscope, increasing the signal to 100mV/g. The noise remained around 1mV/g, so the resolution was improved to 10millig. This is still above the desired 1millig resolution, but acceptable for initial evaluation. The noise floor is partially attributable to the oscilloscope, but there is also a contribution from the cable.

Since we are seeking to detect 1 μ V change at the charge amplifier output, the level of electrical screening required is high. Virtually any electro-magnetic pick-up will be noticeable on the output. The impedance of the circuit increases its sensitivity to both interference and stray signals generated in the cable. A selection of circuits were evaluated, and with any high impedance set-up (10k Ω or above) flexing of the cable generates intolerable interference signals. The charge amplifiers in the prototypes had 270 Ω output impedance, and cable flexing was not detectable.

The resolution of the sensor can be improved by reducing the frequency response bandwidth, by electrically filtering out the high frequencies. This removes some of the

electrical noise from the output signal, and is a technique widely used in the noise and vibration analysis industry.

6.3.3. Frequency response

The response of the accelerometer is limited in frequency. The piezo-electric material only produces a charge output when there is a change in strain, corresponding to a change in acceleration. The charge signal is dissipated through a $1\text{G}\Omega$ resistor, and decays to zero signal with time. The time constant to decay to 50% of the original signal was calculated as 0.16Hz using $f=1/(2*\pi*R*C)$.

The low frequency cut-off was practically assessed by measuring the time to decay to V_0/e in response to a step input. This gave a 3dB cut-off frequency of 0.3Hz; roughly double the theoretical frequency. This difference could be due to resistor value tolerance, dirt and moisture reducing the $1\text{G}\Omega$ resistor value, but since no suitable instrumentation was available, this could not be accurately assessed.

High frequency response of the prototype devices is limited by the lowest resonant frequency of the structure. From the drive and pick-off investigations in Chapter 6.2.3, the first resonance is on the Z-axis at 5330Hz with a quality factor $Q=130$. From Figure 6-1, the level response can be seen to be around 3.04mV, so the 3dB cut-off would be when the amplitude response rises above 6.08mV. This is at 4.5kHz, where the response is rising with frequency. The 2kHz upper frequency cut-off was in-line with expectations, based on working at no more than one third of the resonant frequency.

6.3.4. Amplitude non-linearity

In the design calculations, the acceleration range to be measured was limited by the out of plane deformation of the beams across the bridge creating non-linear response. In the practical trials, these assumptions of flat beams under no initial tension were compromised by the internal stresses between the layers of the beam structures. This stress caused deformation of the beams into shallow domes. With this in mind, the response of the accelerometer was measured at 160 Hz against a range of acceleration amplitudes from 1 to 20g. The results are plotted in Figure 6-2, and can be seen to be linear with amplitude. Analysis showed that 95% of data from tests was within 3% of linear from 0 to 20g. Limitations in the power capability of the shaker table available prevented testing over the entire 50g range of the accelerometer.

6.3.5. Resonant frequency

The resonant frequency was measured by the drive and pick-off method in Chapter 6.2.3. This finds the primary resonant frequency in the Z-axis at 5310Hz, and the secondary resonance at 7kHz. There is 95% correlation with the finite element eigenvalue models, giving good confidence in the theory.

6.3.6. Cross-axis sensitivity

Cross axis sensitivity is the amount of unwanted signal from the orthogonal axes that is present on a particular axis. This requires that the input signal is aligned exactly across the sensitive axis, so that there is no on-axis component of the input acceleration. With commercial shaker systems, reasonable efforts are made to maintain a true direction for the vibration source, but alignment of the sensor die to this axis within better than a few degrees is unlikely.

Cross axis sensitivity currently shows about 5% for the charge amplifier circuit, and up to 100% for the JFET voltage follower circuit. The latter is due to capacitive coupling in the cable and the high impedance output of the circuit, so should be disregarded unless the JFET circuit is used. There is some element of capacitive coupling with the charge amplifier cable, but the cross-axis signal is still present at 1Hz where electrical cross-talk would be dissipated by the low circuit resistance, so is more likely to be due to the electro-mechanical behaviour of the dies.

The expected mechanism for cross-axis sensitivity is thought to be due to the stress deformation of the beams, and some damage to the structures (primarily the failure of the end beams). The pattern of the electrodes on the beams is within 5 microns of the intended position, and finite element analysis in Chapter 4.6.5 indicated that this should result in less than 1% cross-axis sensitivity. However, from experience with the poling procedure, it is expected that there could be variation between PZT segments in the level of poling achieved. This would result in the cross-axis signals not cancelling out. The largest cross-axis signals are found in the x and y-axis sensors, where many of the end beams are damaged. This allows increased movement in response to acceleration in the unwanted directions, and the generation of larger cross-axis signals. If these do not cancel out, due to asymmetry in the state of poling, they will be present in the sensor output.

6.3.7. Temperature

The affect of temperature on the accelerometer has not been analysed, but the electrical behaviour of the sensor and electronics are known to be affected by changes in temperature. The sensor PZT increases both the dielectric strength and charge generation rate with temperature. The charge activity within the electronics also increases with temperature, but the use of a negative feedback loop in the charge amplifier should achieve good temperature stability. However, without further testing the temperature compensation characteristic cannot be assessed.

6.3.8. Shock limit / Structural strength

The shock limit has not been measured, but is estimated from accidental damage due to drop-testing. The impact from a 0.5m drop onto aluminium caused breakage of the beams, and peak acceleration was estimated, based on the sensor package mass, drop height and properties of aluminium. Shock limit values are lower than predicted, and

this is believed to be due to the layer stresses within the beams and PZT stacks which pre-stress the structure.

6.4. Summary of Testing

The testing of practical devices has shown the theoretical models to be generally accurate, and has allowed the derivation of material property values for the thin film PZT. This test work supports the use of the theoretical and FE models for the prediction of device behaviour, but highlighted the difficulties encountered during fabrication; primarily the inter-layer stress build up on the beam structures.

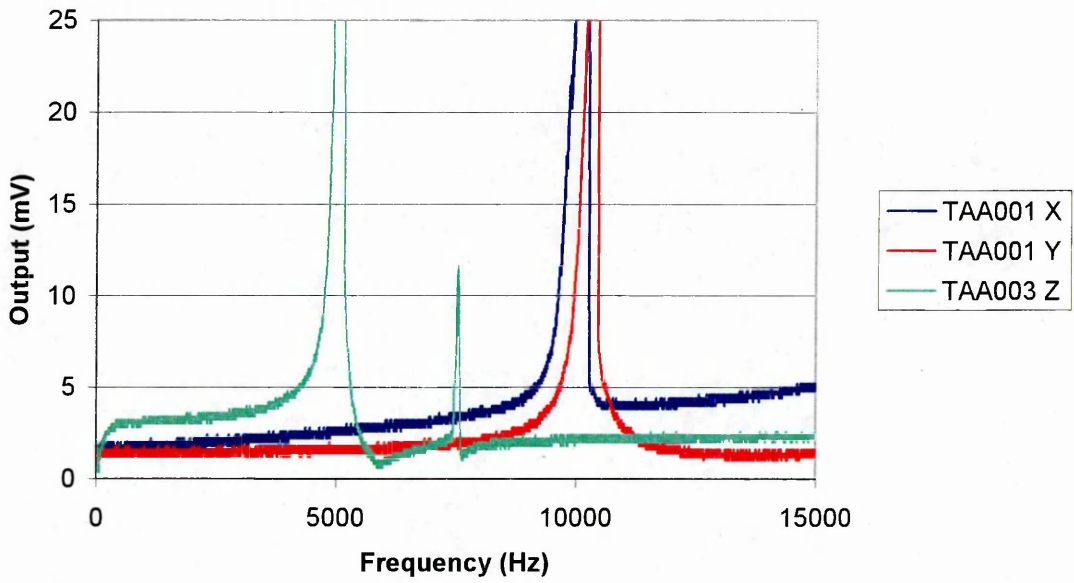


Figure 6-1 Frequency sweep response to 500mV-peak Drive signal

The first peak for each axis sensor is in the measured direction.
 The second peak on TAA003 Z-axis sensor is in-plane resonance.

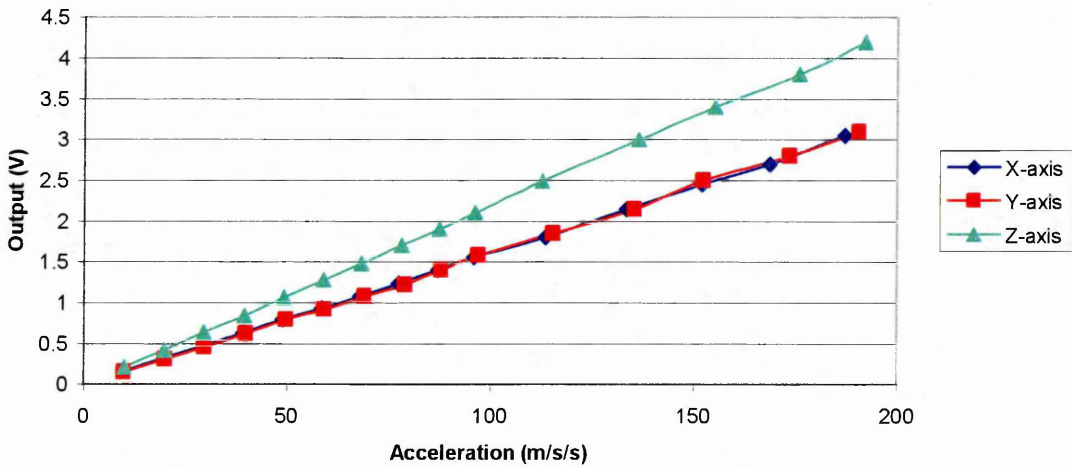


Figure 6-2 Accelerometer response to 1 to 20g input signals

7. Conclusions and Recommendations

7.1. Model construction

The findings from a number of previous research projects, by the likes of vanKampen²⁴, Kunz²³, Scheeper²⁷ and Weinberg²⁸ have been traced back to the classical theory of Roark²⁶, and shown to be consistent in their approach. These findings have been combined to form the basis for the mathematical models presented here.

Mathematical and finite element models have been created to simulate MEMS fabricated accelerometers, where thin flexible beams are deformed in response to the acceleration of a proof mass supported on them. The surface strain of the beams is measured using thin-film PZT in order to resolve the magnitude of the acceleration. The models were used to calculate the resonant frequencies and charge generation values, and agree to within 5%. The finite element models have shown that the mode-shapes presumed in the mathematical models were correct, on all but the highly symmetrical design, where there is a high degree of rotational symmetry and the resonant mode-shape was off-axis.

Designs have been produced for a tri-axial accelerometer die, and two single-axis dies. These designs were calculated to maximise the signal strength, and maintain the first resonant frequency above 5kHz. For maximum sensitivity, the first resonant frequency mode-shape should coincide with the direction and mode shape of the sensitive axis. For the three-axis sensor, three individual devices are created within the available footprint of 5mm by 10mm. Each device was designed with 5pC/g sensitivity in a single direction, and first resonant frequency above 5kHz.

7.2. Physical Prototypes

Practical fabrication of the accelerometer designs was carried-out by Ming-Yu Lim, at Cranfield University. This work has revealed a number of fabrication limitations affecting the design.

Stresses between the layers in the PZT elements and the silicon beams deform the beams into compound-curved surfaces, with an inherent increase of stiffness. The best resolution found was to try to balance the stresses by changing the fabrication sequence, and retaining the oxide layer on the back of the beams.

The electrical connection of the sensors had to be revised, since it proved unsatisfactory to try to reverse the inherent polarisation in the PZT created during the fabrication process. All PZT must be polarised in the same direction, and the segments connected in series, which halved the signal charge, but doubled the voltage output. This was one reason for changing the preferred choice of amplification from charge amplifier to voltage amplifier.

Testing of the physical samples has allowed validation of the models. Sensitivity was approximately 1/3 of the predicted value, mostly due to the use of low-sensitivity 30/70 PZT instead of the 52/48 composition used for the models. Resolution of 10millig was achieved over a 200Hz bandwidth (filtering out the high frequency noise), and a useful frequency range of 0.3Hz to 2kHz within 3dB of linear amplitude response. Amplitude linearity of better than 5% was achieved, together with less than 5% cross-axis sensitivity. These figures were all close to the predicted values, and refinement of both manufacturing and test methods should allow further improvement.

7.3. Revision of material properties

The models are all limited by the materials properties data available. Practical experimentation involving the deposition of the desired material by the chosen method is the only way to generate valid material data. Values using 30/70 composition PZT have been derived for the piezo-electric charge constant $d_{31} = -31 \times 10^{-12}$ C/N and the dielectric strength $\epsilon_{33} = 4.1 \times 10^{-9}$ F/m.

The overall efficiency of the accelerometer structure in converting from mechanical to electrical energy was also assessed. This piezoelectric coupling coefficient was found to be 5.5% for the in-plane sensors, and 7.8% for the Z-axis sensor.

7.4. Future work

A primary objective of the STAMP project was to develop an accelerometer for commercial production. To this end, the work described in this thesis is being continued to achieve a set of repeatable fabrication process steps, and achieve a production-scale manufacturing route. The models developed in this work will continue to be available for the design of further variants of accelerometer.

One area that is of great importance to the usability of an accelerometer, or any other sensor, is temperature dependant variability. In an ideal situation, the sensor would behave repeatability irrespective of temperature. However, with the stresses in the

accelerometer die structure, temperature induced changes in the PZT properties, and temperature dependency of the behaviour of semi-conductor electronics it is expected that some level of temperature compensation will be required for the accelerometer. The whole area of temperature stability has been neglected in this thesis, since the stresses in the accelerometer die structure were not repeatable between wafers. Once the fabrication process is under control, investigation of temperature stability will be required.

References

- ¹ Kistler **Kistler Conventional Accelerometer, Principle of Operation**
Kistler Instrumente AG Winterthur, Switzerland, www.kistler.ch
- ² Endevco 65 Endevco Corporation (September 2001)
Endevco Model 65 - Isotron Accelerometer Datasheet
- ³ Thompson B.J. Thompson (2000)
A Guide to Accelerometer Specifications
Test & Measurement World, 15 February 2000
- ⁴ Madou Marc J. Madou (1997), **Fundamentals of Microfabrication**,
CRC Press LLC, 1997. pp.159-160.
- ⁵ TAG Electronics Techniques d'Avant-Garde
www.tagelectronics.co.uk/Products/products/all/app_sens_accel.asp
- ⁶ Endevco 7268 Endevco Corporation (October 2001)
Endevco Model 7268B - Piezoresistive Accelerometer Datasheet
- ⁷ SensoNor SensoNor asa **SA50 Dual Axis Accelerometer Datasheet**
www.sensonor.com/
- ⁸ Li G. Li, Z. Li, C. Wang, Y. Hao, T. Li, D. Zhang, G. Wu (2001)
Design and fabrication of a highly symmetrical capacitive triaxial accelerometer
Journal of Micromechanics and Microengineering 11, pp.48-54.
- ⁹ Boser B.E. Boser, R.T. Howe (1995)
Surface Micromachined Accelerometers
IEEE 1995 Custom Integrated Circuits Conference, pp.15.1.1-15.1.8.

-
- ¹⁰ Analog IMI Analog Devices application notes, www.imi-mems.com/
- ¹¹ Lemkin M. Lemkin, B.E. Boser (1999)
A Three-Axis Micromachined Accelerometer with a CMOS Position-Sense Interface and Digital Offset-Trim Electronics
IEEE Journal of Solid-State Circuits 34, No 4, pp.456-468.
- ¹² Analog Analog Devices
ADXL 150/ ADXL 250 Datasheet www.analog.com/
- ¹³ Endevco 7290 Endevco Corporation (November 2000)
Endevco Model 7290A – Variable Capacitance Accelerometer Datasheet
- ¹⁴ VTI Hamlin VTI Hamlin (2001) <http://www.vti.fi/technology/more.html>
- ¹⁵ Xie H. Xie and G. Fedder **A CMOS z-axis capacitive accelerometer with comb-finger sensing**
MEMS '00, pp.496-501. – *Proceedings of The 13th IEEE International Conference on Micro Electro Mechanical Systems, January 2000*
- ¹⁶ MSI Measurement Specialties Incorporated
ACH-04-08-05 Accelerometer Datasheet
- ¹⁷ deReus R. deReus, J.O. Gulløv, P.R. Scheeper (1999)
Fabrication and Characterization of a Piezoelectric Accelerometer
Journal of Micromechanics and Microengineering 9, pp. 123-126.
- ¹⁸ Zou Q. Zou, W. Tan, E.S. Kim, G.E. Loeb (2003)
Highly Symmetric Tri-axis Piezoelectric Bimorph Accelerometer
MEMS 2004, pp.197-200 – The 17th Annual IEEE International Conference on MEMS, Maastricht, Netherlands, January 2004.
- ¹⁹ Zou Q. Zou, W. Tan, E.S. Kim, G.E. Loeb (2003)
Implantable Bimorph Piezoelectric Accelerometer for Feedback Control of Functional Neuromuscular Stimulation
Transducers '03, pp.1379-1382.
The 12th International Conference on Solid State Sensors, June 2003.
- ²⁰ Yoon Y.S. Yoon, J.H. Kin, M.T. Hsieh, D.L. Polla (1998)
Fabrication and Characterisation of Microelectromechanical System Device Based on PZT Films and Surface Micromachining
Journal of the Korean Physical Society 32, pp.S1760-S1762.

-
- ²¹ Beeby S.P. Beeby, J.N. Ross, N.M. White (2000)
Design and Fabrication of a micromachined silicon accelerometer with thick-film printed PZT sensors
Journal of Micromechanics and Microengineering 10, pp. 322-328.
- ²² Beeby S.P. Beeby, N.J. Grabham, N.M. White (2001)
Microprocessor implemented self-validation of thick-film PZT/silicon accelerometer *Sensors & Actuators A92*, pp. 168 – 174.
- ²³ Kunz K. Kunz, P. Enoksson, G. Stemme (2001)
Highly sensitive tri-axial silicon accelerometer with integrated PZT thin film detectors *Sensors & Actuators A92*, pp. 156 – 160.
- ²⁴ vanKampen R.P. vanKampen and R.F. Wolfenbuttel (1998)
Modeling the mechanical behaviour of bulk-micro-machined silicon accelerometers *Sensors & Actuators A64*, pp. 137 – 150.
- ²⁵ Yu J-C. Yu and C-B. Lan (2001)
System modeling of microaccelerometer using piezoelectric thin films *Sensors & Actuators A88*, pp. 178 – 186.
- ²⁶ Young W.C. Young (1989)
Roark's Formulas for Stress and Strain, Sixth Edition,
Mc Graw-Hill International Editions. ISBN 0-07-100373-8.
- ²⁷ Scheeper P.R. Scheeper, J.O. Gulløv, L.M. Kofoed (1996)
A Piezoelectric Triaxial Accelerometer
Journal of Micromechanics and Microengineering 6, pp. 131-133.
- ²⁸ Weinberg M.S. Weinberg (1999)
Working Equations for Piezoelectric Actuators and Sensors
ASME / IEEE Journal of MEMS, Vol.8, No.4, pp. 71 – 78.
- ²⁹ Smits J.G. Smits and W-S. Choi (1991)
The constituent equations of piezoelectric heterogeneous bimorphs
IEEE Transactions on Ultrasonics, Ferroelectrics, and Frequency Control, Vol.38, No.3, May 1991, pp. 256 – 270
- ³⁰ Yi T. Yi, L.Li, C-J.Kim (2000),
Microscale material testing of single crystal silicon: process effects on surface morphology and tensile strength
Sensors and Actuators, A83, pp.172-178

-
- ³¹ Spiering V.L. Spiering, S. Bouwstra, R.M.E.J. Spiering (1993)
On-chip decoupling zone for package-stress reduction
Sensors & Actuators A39, pp. 149 – 156.
- ³² Gardiniers J.G.E. Gardiniers, A.G.B. Verholen, N.R. Tas, M. Elwenspoek (1998)
Direct Measurement of Piezoelectric Properties of Sol-Gel PZT Films
Journal of the Korean Physical Society 32, pp.S1573-S1577.
- ³³ Huang Z. Huang, Q.Zhang, R.W. Whatmore (1999)
Low temperature crystallisation of lead zirconate titanate thin films by a sol-gel method
Journal of Applied Physics 85, pp.7355-7361.
- ³⁴ Shepard J.F. Shepard, P.J. Moses, S.Trolier-McKinstry (1998)
The wafer flexure technique for the determination of the transverse piezoelectric coefficient (d_{31}) of PZT thin films
Sensors & Actuators A71, pp. 133 – 138.
- ³⁵ Inostek **Inostek Inc. Website**, Inostek Inc, 356-1 Gasan, Keumchun, Seoul 153-802, KOREA, www.inostek.com/dslee07/t_pzt.htm
- ³⁶ Kim 2003 S-H. Kim, et al.(2003)
Electromechanical Properties of Pb(Zr,Ti)O₃ Films for MEMS Applications
Journal of the Korean Physical Society 42, pp. S1101-S1104
- ³⁷ Kim 2002 S-H. Kim, et al.(2002)
Orientation effects in chemical solution derived Pb(Zr_{0.3},Ti_{0.7})O₃ thin films on ferroelectric properties
Thin Solid Films 416, pp.264-270
- ³⁸ Jaffe B. Jaffe, W.R. Cook, H. Jaffe (1971)
Piezoelectric Ceramics, *Academic Press*, New York.
- ³⁹ EMRC **NISA DispIV Help Manual**
Engineering Mechanics Research Corporation,
1607 East Big Beaver Road, Troy, Michigan 48083 USA
- ⁴⁰ Lim M.Y. Lim, May 2003 (Unpublished),
Silicon Traixial Accelerometer Vibration Measurement Project, Cranfield University Progress Report, Year 1, Cranfield University

-
- ⁴¹ Branger V. Branger, V. Pelosin, K. F. Badawi and Ph. Goudeau (1996) , **Study of the mechanical and microstructural state of platinum thin films** *Thin Solid Films* 275, pp. 22-24
- ⁴² Lisby T.H. Lisby, O. Hansen, J.A. Branebjerg (2002), **Fabrication and Characterisation of Flexible Silicon Substrates with Electroplated Gold Leads**, *IEEE*
- ⁴³ Komai K. Komai, K. Minoshima, S. Inoue (1998), **Fracture and fatigue behavior of single crystal silicon microelements and nanoscopic AFM damage evaluation**, *Microsystem Technologies* 5, pp.30–37 (Springer-Verlag)
- ⁴⁴ MEMSnet **MEMSnet website**, www.MEMSnet.org/material/platinumpfilm/
- ⁴⁵ Mitsubishi **Mitsubishi Materials Corporation Website**, 1-5-1, Otemachi Chiyoda-Ku, TOKYO, Japan www.mmc.co.jp/adv/ele/english/electric5-2.html
- ⁴⁶ Zhu M. Zhu, May 2002 (unpublished), **Electrode Connection Discussion**, Cranfield University
- ⁴⁷ Southin J.E.A. Southin, S.A. Wilson, D. Schmitt, R.W. Whatmore (2001) **e_{31} determination for PZT films using a conventional d_{33} meter** *Journal of Physics D: Applied Physics* 34 (2001) pp.1456-1460

Further Reading

A number of other texts were read during the preparation of this thesis, but were not of direct relevance. However, they are of interest as background reading, so are listed below.

- Ando T. Ando, X. Liu, S. Nakao, T. Kasai, M. Shikida, K. Sato (2004)
Effect of Crystal Orientation on Fracture Strength and Fracture Toughness of Single Crystal Silicon
MEMS 2004, pp.177-180 – The 17th Annual IEEE International Conference on MEMS, Maastricht, Netherlands, January 2004.
- Beliveau A. Beliveau, G.T. Spencer, K.A. Thomas, S.L. Robertson (1999)
Evaluation of MEMS Capacitive Accelerometers
IEEE Design & Test of Computers, Oct-Dec 1999, pp.48-56.
- Burdess J.S. Burdess, A.J. Harris, D. Wood, R. Pitcher (2000)
The structural characteristics of microengineered bridges
Proceedings of the IMechE 214-C, pp.351-357.
- Chen P-L. Chen, R.S. Muller, R.D. Jolly, G.L. Halac, R.M. White, A.P. Andrews, T.C. Lim, M.E. Motamedi (1982)
Integrated Silicon Microbeam PI-FET Accelerometer
IEEE Transactions on Electron Devices ED-29, pp.27-33.
- Dunn S. Dunn, R.W. Whatmore (2001)
Substrate effects on domain structures of PZT 30/70 sol-gel films via PiezoAFM
Journal of the European Ceramic Society 22, pp.825-833.
- Hu H-H. Hu and W. Fang (2004)
A Novel (111) Single-Crystal-Silicon Accelerometer Using Parallel-Connected Parallel Plate Capacitance
MEMS 2004, pp.597-600 – The 17th Annual IEEE International Conference on MEMS, Maastricht, Netherlands, January 2004.
- Gaucher P. Gaucher (2002)
Piezoelectric micro-electro-mechanical systems for acoustic applications *Piezoelectric Materials in Devices*, pp.261-282
EPFL Swiss Federal Institute of Technology
Workshop "Piezoelectric for the End User", Interlaken, Feb 2002

- Kraft M. Kraft (2000)
Micromachined Inertial Sensors State of the Art and a Look into the Future
Journal IMC Measurement and Control 33, No 6.
- Li G. Li, Z. Li, C. Wang, Y. Hao, T. Li, G. Wu (2000)
Design and Simulation of a Novel Highly Symmetrical Piezoelectric Triaxial Accelerometer
MSM 2000, Technical Proceedings of the 2000 International Conference on Modeling and Simulation of Microsystems
- Maiwa H. Maiwa (2003)
Temperature dependence of the electrical and electromechanical properties of lead zirconate titanate thin films
Applied Physics Letters 83, No 21, American IOP, pp.4396-4398.
- Petersen K.E. Petersen, A. Shartel, N.F. Raley (1982)
Micromechanical Accelerometer Integrated with MOS Detection Circuitry
Transactions on Electron Devices ED-29, No 1, pp.23-27
- Renard S. Renard (2000)
SOI Micromachining Technologies for MEMS
Proceedings of SPIE Volume: 4174, pp.193-199
 Micromachining and Microfabrication Process Technology VI
- Toyama M. Toyama, R. Kubo, E. Takata, K. Tanaka, K. Ohwada (1994)
Characterisation of piezoelectric properties of PZT thin films deposited on Si by ECR sputtering
Sensors & Actuators A45, pp. 125-129.
- Vakili Amini B. Vakili Amini, S. Pourkamali, and F. Ayazi (2004)
A High Resolution, Stictionless, CMOS Compatible SOI Accelerometer with a Low Noise, Low Power, 0.25 μ m CMOS Interface
MEMS 2004, pp. 572-575 – The 17th Annual IEEE International Conference on MEMS, Maastricht, Netherlands, January 2004
- Yazdi N. Yazdi, F. Ayazi, K. Najafi (1998)
Micromachined Inertial Sensor
Proceedings of the IEEE 86, No 8, pp1640-1647.

Appendix 1. MathCAD models

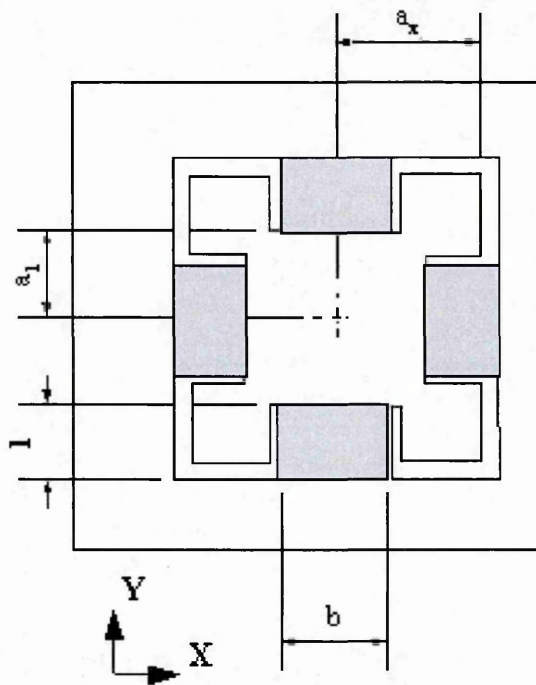
1.1.	Highly symmetrical design.....	106
1.2.	In-plane sensing	109
1.3.	Multi-layer beam stiffness.....	112

1.1. Highly symmetrical design

Mathematical Model of Inset Highly Symmetric STAMP Accelerometer

This model is based on a quarter model of the multiple supported mass. It uses Roark theory to determine the stiffness characteristics of a proposed accelerometer configuration in the x, y, and z directions.

Note: rotary acceleration of the device about x (Rx) will generate an error on the y-axis signal.



Device Variables

$$a_x := 1.2 \cdot 10^{-3} \cdot \text{m}$$

$$a_1 := 0.83 \cdot 10^{-3} \cdot \text{m}$$

$$L := 420 \cdot 10^{-6} \cdot \text{m}$$

$$b := 1100 \cdot 10^{-6} \cdot \text{m}$$

$$tw := 525 \cdot 10^{-6} \cdot \text{m}$$

$$d := 8 \cdot 10^{-6} \cdot \text{m}$$

$$E := 169 \times 10^9 \frac{\text{N}}{\text{m}^2}$$

$$\rho := 2330 \frac{\text{kg}}{\text{m}^3}$$

tw = thickness of wafer

d = thickness of beams

Z_c = depth to centre of mass

Resonant Frequency Calculation

For square proof mass

$$a_y := a_x \quad x(y) := a_x \quad y := a_y$$

For inset beams

$$x(y) := a_x - \left(y \leq \frac{b}{2} + 10^{-5} \text{m} \right) \cdot (a_x - a_1) - \left(y \geq a_1 \right) \cdot \left(\frac{b}{2} + 10^{-5} \text{m} \right)$$

$$M := 4 \cdot \rho \cdot \int_0^{tw} \int_0^{a_x} x(y) \, dy \, dz \quad M = 5.009 \times 10^{-6} \text{kg}$$

$$Z_c := \frac{tw}{2} \quad Z_c = 262.5 \times 10^{-6} \text{m}$$

$$I_{\theta x} := 4 \cdot \rho \cdot \int_0^{tw} \int_0^{a_x} x(y) \cdot (y^2 + z^2) \, dy \, dz \quad I_{\theta x} = 2.68 \times 10^{-12} \text{kgm}^2$$

$$I_x := \frac{b \cdot d^3}{12} \cdot 10^{12}$$

$$I_x = 46.933 \times 10^{-9} \text{ m}^4$$

$$K_x := 4 \cdot \frac{12 \cdot E \cdot I_x}{L^3 \cdot 10^{12}}$$

$$K_x = 5138.797 \frac{\text{N}}{\text{m}}$$

Z axis stiffness

$$K_{\theta x} := K_x \cdot \frac{L^2 + 3 \cdot a_1 \cdot L + 3 \cdot a_1^2}{6}$$

$$K_{\theta x} = 0.002817 \text{ N}\cdot\text{m}$$

Y axis stiffness

$$K := \frac{b}{2} \cdot \left(\frac{d}{2}\right)^3 \cdot 10^{12} \cdot \left[\frac{16}{3} - 3.36 \cdot \frac{d}{b} \left(1 - \frac{d^4}{12 \cdot b^4} \right) \right]$$

$$K = 186.873 \times 10^{-9} \text{ m}^4$$

$$G := 64.1 \cdot 10^9 \cdot \frac{\text{N}}{\text{m}^2}$$

$$T_{\theta x} := \frac{2 \cdot K \cdot G}{L \cdot 10^{12}}$$

$$T_{\theta x} = 57.041 \times 10^{-6} \text{ N}\cdot\text{m}$$

Y axis torsion

$$K_{\theta x} + T_{\theta x} = 2.87 \times 10^{-3} \text{ N}\cdot\text{m}$$

Overall y-axis Stiffness

Check : In-plane Stiffness

Out of plane Stiffness

$$K_x := 2 \cdot \frac{E \cdot d \cdot b^3}{L^3} + 2 \cdot \frac{E \cdot b \cdot d}{L} \quad K_x = 55.66 \times 10^6 \frac{\text{N}}{\text{m}}$$

$$K_y := \frac{K_{\theta x}}{a_1 \cdot Z_c} \quad K_y = 12.93 \times 10^3 \frac{\text{N}}{\text{m}}$$

$$\frac{K_x}{K_y} = 4305.133$$

Effectively Zero in-plane movement if greater than 1000

Check : Limit of Deflection
0.15d for 3% Linearity

Axial strain affects linearity less than 3% if limit is greater than 50g

$$A_x := \frac{0.15 \cdot d \cdot K_x}{M} \quad A_x = 126 \text{ g}$$

$$A_{xT} := \frac{0.15 \cdot d \cdot (K_{\theta x} + T_{\theta x})}{M \cdot a_1 \cdot Z_c} \quad A_{xT} = 322 \text{ g}$$

Resonant Frequencies

$$f_{0z} := \frac{1}{2\pi} \cdot \sqrt{\frac{K_x}{M}} \quad f_{0y} := \frac{1}{2\pi} \cdot \sqrt{\frac{K_{\theta x}}{I_{\theta x}}} \quad f_{0yT} := \frac{1}{2\pi} \cdot \sqrt{\frac{K_{\theta x} + T_{\theta x}}{I_{\theta y}}}$$

$$f_{0z} = 5097.939 \text{ Hz} \quad f_{0y} = 5159.727 \text{ Hz} \quad f_{0yT} = 5211.707 \text{ Hz}$$

Note : f_{0y} is included to show the error if torsion is ignored

Piezo-generated output for a given beam deflection

$$d_{31} := -93.5 \cdot 10^{-12} \frac{\text{C}}{\text{N}} \quad v = 0.31 \quad c_{11} := 11.425 \cdot 10^{10} \frac{\text{N}}{\text{m}^2} \quad c_{12} := 5.83 \cdot 10^{10} \frac{\text{N}}{\text{m}^2} \quad \theta_a := \frac{dy}{a_1}$$

$$M_d(v) := \frac{12 \cdot E \cdot I_x}{L^3} \cdot dy \cdot v - \frac{6 \cdot E \cdot I_x}{L^2} \cdot dy$$

Moments for Z axis

$$dQ_d(v) := d_{31} \cdot M_d(v) \cdot \frac{d}{2 \cdot E \cdot I_x} (c_{11} - \nu \cdot c_{12})$$

$$Q_z := \int_{0.1 \cdot L}^{0.4 \cdot L} dQ_d(v) \cdot \frac{b}{dy} dv - \int_{0.6 \cdot L}^{0.9 \cdot L} dQ_d(v) \cdot \frac{b}{dy} dv \rightarrow \frac{1.6957379057142857142 \cdot 10^{-4}}{m} \cdot C$$

Charge per beam per metre movement - z-axis

$$M_y(v) := \frac{12 \cdot E \cdot I_x}{L^3} \cdot a_1 \cdot \theta_a \cdot v - \frac{6 \cdot E \cdot I_x}{L^2} \cdot a_1 \cdot \theta_a + \frac{6 \cdot E \cdot I_x}{L^2} \cdot \theta_a \cdot v - \frac{4 \cdot E \cdot I_x}{L} \cdot \theta_a \quad \text{Moments for Y axis}$$

Check : Point of zero Bending

$$\phi := M_y(v) = 0 \text{ solve, } v \rightarrow 2.2413461538461538462 \cdot 10^{-4} \cdot m$$

$$dQ_s(v) := d_{31} \cdot M_s(v) \cdot \frac{d}{2 \cdot E \cdot I_x} (c_{11} - \nu \cdot c_{12})$$

$$\frac{\phi}{L} = 0.534$$

$$Q_y := \int_{0.1 \cdot L}^{0.4 \cdot L} dQ_s(v) \cdot \frac{b}{\theta_a} dv - \int_{0.6 \cdot L}^{0.9 \cdot L} dQ_s(v) \cdot \frac{b}{\theta_a} dv \rightarrow 1.7635674219428571428 \cdot 10^{-7} \cdot C$$

Charge per beam per radian movement - y-axis

Integral limits set to 0.1-0.4L and 0.6-0.9L by default

Use alternative values for optimisation based on ϕ

Charge Output

$$S_{Qz} := \frac{M}{K_z} \cdot 4 \cdot Q_z$$

$$S_{Qy} := \frac{M \cdot Z_c}{K_{\theta x}} \cdot 2 \cdot Q_y$$

$$S_{QyT} := \frac{M \cdot Z_c}{K_{\theta x} + T_{\theta x}} \cdot 2 \cdot Q_y$$

$$S_{Qz} = 6.483 \times 10^{-12} \frac{C}{g}$$

$$S_{Qy} = 1.614 \times 10^{-12} \frac{C}{g}$$

$$S_{QyT} = 1.582 \times 10^{-12} \frac{C}{g}$$

Capacitance of the PZT elements

$$\epsilon_{33} := 6.46 \cdot 10^{-9} \frac{F}{m} \quad t_{\text{piezo}} := 0.3 \cdot 10^{-6} m$$

$$A := 4 \cdot b \cdot 0.3L$$

$$c := \frac{\epsilon_{33} \cdot A}{t_{\text{piezo}}} \quad c = 11.938 \times 10^{-9} F$$

Total area of piezo elements on two beams corresponding to the charge integrals

Voltage output before charge amplifier

$$\frac{S_{Qz}}{2 \cdot c} = 271.535 \times 10^{-6} \frac{V}{g}$$

$$\frac{S_{Qy}}{c} = 135.235 \times 10^{-6} \frac{V}{g}$$

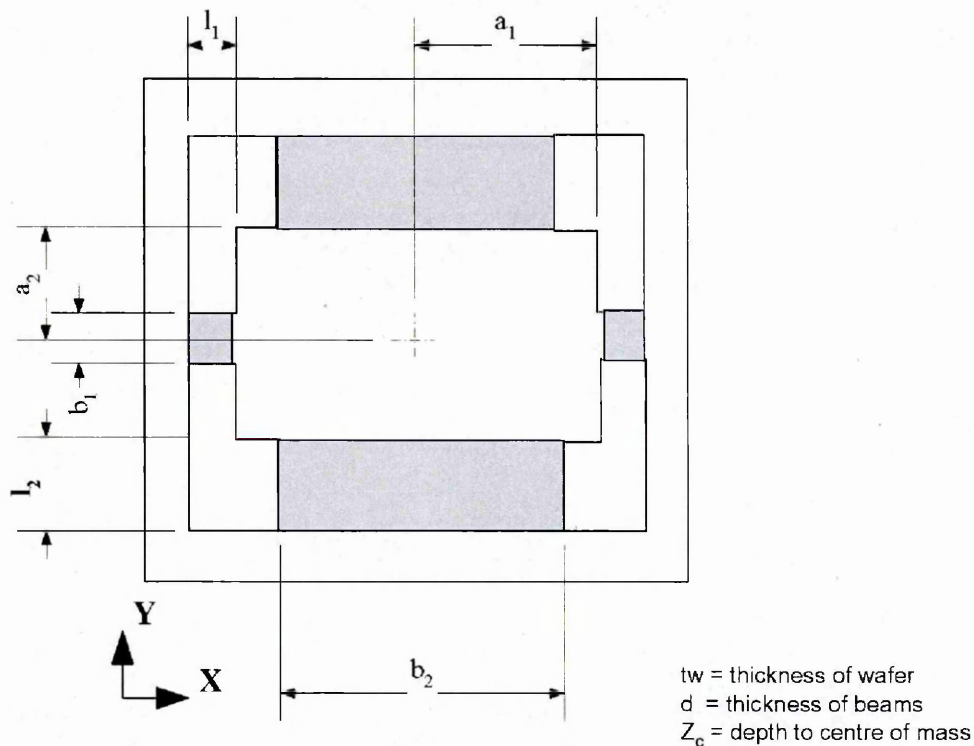
$$\frac{S_{QyT}}{c} = 132.551 \times 10^{-6} \frac{V}{g}$$

1.2. In-plane sensing

Mathematical Model of Asymmetric STAMP Accelerometer

This model is based on a quarter model of the multiple supported mass. It uses Roark theory to determine the stiffness characteristics of a proposed accelerometer configuration in the x, y, and z directions.

Note: rotary acceleration of the device about x (Rx) will generate an error on the y-axis signal.



Device Variables

$$\begin{aligned}
 b_1 &:= 50 \cdot 10^{-6} \cdot \text{m} & l_1 &:= 75 \cdot 10^{-6} \cdot \text{m} & b_2 &:= 2000 \cdot 10^{-6} \cdot \text{m} & l_2 &:= 1200 \cdot 10^{-6} \cdot \text{m} & E &:= 169 \times 10^9 \cdot \frac{\text{N}}{\text{m}^2} \\
 a_x &:= 1.1 \cdot 10^{-3} \cdot \text{m} & a_y &:= 0.65 \cdot 10^{-3} \cdot \text{m} & d &:= 8 \cdot 10^{-6} \cdot \text{m} & \text{tw} &:= 525 \cdot 10^{-6} \cdot \text{m} \\
 N &:= \text{kg} \cdot \frac{\text{m}}{\text{s}^2} & \rho C &:= 10^{-12} \cdot \text{C} & b &:= (b \leq 2 \cdot a_x) \cdot b + (b > 2 \cdot a_x) \cdot 2 \cdot a_x & a_1 &:= a_x & \rho &:= 2330 \frac{\text{kg}}{\text{m}^3} \\
 & & & & & & a_2 &:= a_y & &
 \end{aligned}$$

Resonant Frequency Calculation

Formulae for the sloping sides of a wet etched mass.

$$x := a_x - \frac{z}{\sqrt{2}} \quad y := a_y - \frac{z}{\sqrt{2}} \quad \text{tw} := (tw \leq a_x \cdot \sqrt{2}) \cdot tw + (tw > a_x \cdot \sqrt{2}) \cdot a_x \cdot \sqrt{2}$$

$$M := \int_0^{tw} 4.0 \cdot \rho \cdot x \cdot y \, dz \rightarrow 2.1338878074661586737 \cdot 10^{-6} \cdot \text{kg}$$

$$Z_c := \int_0^{tw} \frac{4 \cdot \rho \cdot x \cdot y \cdot z}{M} \, dz \rightarrow 2.1115271465527890633 \cdot 10^{-4} \cdot \text{m}$$

$$I_{\theta x} := \int_0^{tw} 4 \cdot \rho \cdot x \cdot y \cdot \left(\frac{y^2}{3} + z^2 \right) \, dz \rightarrow 3.2527966769433264953 \cdot 10^{-13} \cdot \text{m}^2 \cdot \text{kg}$$

$$I_{\theta y} := \int_0^{tw} 4 \cdot \rho \cdot x \cdot y \cdot \left(\frac{x^2}{3} + z^2 \right) \, dz \rightarrow 7.898435705123301424 \cdot 10^{-13} \cdot \text{m}^2 \cdot \text{kg}$$

$$I_{z1} := \frac{b_1 \cdot d^3}{12} \cdot 10^{12} \quad I_{z3} := \frac{b_2 \cdot d^3}{12} \cdot 10^{12} \quad M = 2.134 \times 10^{-6} \text{ kg}$$

$$K_{z1} := 2 \cdot \frac{12 \cdot E}{10^{12}} \cdot \frac{I_{z1}}{l_1^3} \quad K_{z2} := 2 \cdot \frac{12 \cdot E}{10^{12}} \cdot \frac{I_{z2}}{l_2^3} \quad \text{Flexing stiffness}$$

Flexing stiffness

$$K_z = 20710.637 \frac{\text{N}}{\text{m}}$$

$$K_{\theta x} := K_{z2} \cdot \frac{l_2^2 + 3 \cdot a_2 \cdot l_2 + 3 \cdot a_2^2}{3} \quad K_z := K_{z1} + K_{z2} \quad K_{\theta x} = 336.999 \times 10^{-6} \text{ N}\cdot\text{m}$$

$$K_1 = \frac{b_1}{2} \cdot \left(\frac{d}{2} \right)^3 \cdot 10^{12} \cdot \left[\frac{16}{3} - 3.36 \cdot \frac{d}{b_1} \cdot \left(1 - \frac{d^4}{12 \cdot b_1^4} \right) \right] \quad G := 64.1 \cdot 10^9 \cdot \frac{\text{N}}{\text{m}^2}$$

$$T_{\theta x} := \frac{2 \cdot K_1 \cdot G}{l_1 \cdot 10^{12}} \quad K_1 = 7.673 \times 10^{-9} \text{ m}^4 \quad T_{\theta x} = 13.116 \times 10^{-6} \text{ N}\cdot\text{m}$$

$$K_{\theta y} = K_{z1} \cdot \frac{l_1^2 + 3 \cdot a_1 \cdot l_1 + 3 \cdot a_1^2}{6} \quad K_{\theta y} = 0.013274 \text{ N}\cdot\text{m} \quad d_2 := 9 \cdot 10^{-6} \text{ m}$$

$$K_2 = \frac{b_2}{2} \cdot \left(\frac{d_2}{2} \right)^3 \cdot 10^{12} \cdot \left[\frac{16}{3} - 3.36 \cdot \frac{d_2}{b_2} \cdot \left(1 - \frac{d_2^4}{12 \cdot b_2^4} \right) \right] \quad K_y := \frac{K_{\theta x} + T_{\theta x}}{a_2 \cdot Z_c}$$

$$T_{\theta y} := \frac{2 \cdot K_2 \cdot G}{l_2 \cdot 10^{12}} \quad K_2 = 484.622 \times 10^{-9} \text{ m}^4 \quad T_{\theta y} = 51.774 \times 10^{-6} \text{ N}\cdot\text{m}$$

$$f_{0z} := \frac{1}{2\pi} \cdot \sqrt{\frac{K_z}{M}} \quad f_{0y} := \frac{1}{2\pi} \cdot \sqrt{\frac{K_{\theta x} + T_{\theta x}}{I_{\theta x}}} \quad f_{0x} := \frac{1}{2\pi} \cdot \sqrt{\frac{K_{\theta y} + T_{\theta y}}{I_{\theta y}}} \quad K_x := \frac{K_{\theta y} + T_{\theta y}}{a_1 \cdot Z_c}$$

$$f_{0z} = 15679.459 \text{ Hz}$$

$$f_{0y} = 5221.518 \text{ Hz}$$

$$f_{0x} = 20672.662 \text{ Hz}$$

$$K_x = 57372.564 \frac{\text{N}}{\text{m}}$$

Piezo-generated output for a given beam deflection

$$d_{31} := -93.5 \cdot 10^{-12} \frac{\text{C}}{\text{N}} \quad v := 0.295 \quad c_{11} := 7.246 \cdot 10^{10} \frac{\text{N}}{\text{m}^2} \quad c_{12} := 2.075 \cdot 10^{10} \frac{\text{N}}{\text{m}^2} \quad \theta_a := \frac{dy}{a_2}$$

$$M_d(v) := \frac{12 \cdot E \cdot I_{z2}}{l_2^3} \cdot dy \cdot v - \frac{6 \cdot E \cdot I_{z2}}{l_2^2} \cdot dy$$

$$dQ_d(v) := d_{31} \cdot M_d(v) \cdot \frac{d}{2 \cdot E \cdot I_{z2}} \cdot (c_{11} - v \cdot c_{12})$$

$$Q_z := \int_{0.0 \cdot l_2}^{0.367 \cdot l_2} dQ_d(v) \cdot \frac{b_2}{dy} dv - \int_{0.417 \cdot l_2}^{1.0 \cdot l_2} dQ_d(v) \cdot \frac{b_2}{dy} dv \rightarrow \frac{1.1795549049735000000 \cdot 10^{-4}}{\text{m}} \cdot \text{C}$$

Charge stiffness per beam per 1 μm movement - z-axis

$$M_s(v) := \frac{12 \cdot E \cdot I_{z2}}{l_2^3} \cdot a_2 \cdot \theta_a \cdot v - \frac{6 \cdot E \cdot I_{z2}}{l_2^2} \cdot a_2 \cdot \theta_a + \frac{6 \cdot E \cdot I_{z2}}{l_2^2} \cdot \theta_a \cdot v - \frac{4 \cdot E \cdot I_{z2}}{l_2} \cdot \theta_a$$

$$dQ_s(v) := d_{31} \cdot M_s(v) \cdot \frac{d}{2 \cdot E \cdot I_{z2}} \cdot (c_{11} - v \cdot c_{12})$$

$$Q_y := \int_{0.0 \cdot l_2}^{0.583 \cdot l_2} dQ_s(v) \cdot \frac{b_2}{\theta_a} dv - \int_{0.633 \cdot l_2}^{1.0 \cdot l_2} dQ_s(v) \cdot \frac{b_2}{\theta_a} dv \rightarrow 1.5816258228168750001 \cdot \text{pC/radian}$$

$$S_{qz} := \frac{M}{K_z} \cdot 2 \cdot Q_z \quad S_{qz} = 238.367 \times 10^{-15} \frac{\text{C}}{\text{g}}$$

$$A_z := \frac{d \cdot K_z}{2 \cdot M} \quad A_z = 38822 \frac{\text{m}}{\text{s}^2}$$

$$S_{qy} := \frac{M \cdot Z_c}{K_{\theta x} + T_{\theta x}} \cdot 2 \cdot Q_y \quad S_{qy} = 3.992 \times 10^{-12} \frac{\text{C}}{\text{g}}$$

$$A_y := \frac{d \cdot K_y}{2 \cdot M} \quad A_y = 4782 \frac{\text{m}}{\text{s}^2}$$

Charge Output

$$A_x := \frac{d}{2 \cdot M} \cdot \frac{K_{\theta y} + T_{\theta y}}{a_1 \cdot Z_c} \quad A_x = 107546 \frac{\text{m}}{\text{s}^2}$$

Capacitance of the PZT elements is

$$\epsilon_{33} := 6.46 \cdot 10^{-9} \frac{\text{F}}{\text{m}} \quad A := 2 \cdot b_2 \cdot 0.95 l_2$$

$$t_{\text{piezo}} := 1.0 \cdot 10^{-6} \text{ m} \quad \text{Total area of 4 piezo elements}$$

$$c := \frac{\epsilon_{33} \cdot A}{t_{\text{piezo}}} \quad c = 29.458 \times 10^{-9} \text{ F}$$

acceleration for 1/2 beam thickness deflection

Voltage output before amplification

$$\frac{S_{qz}}{c} = 8.092 \times 10^{-6} \frac{\text{V}}{\text{g}}$$

$$\frac{S_{qy}}{c} = 135.524 \times 10^{-6} \frac{\text{V}}{\text{g}}$$

1.3. Multi-layer beam stiffness

Derivation of multimorph piezo-electric beam theory from MS. Weinberg.
Material property values from Yu + Lan.

$$b := 2000 \cdot 10^{-6} \cdot \text{m} \quad L := 1200 \cdot 10^{-6} \cdot \text{m} \quad tw := 525 \cdot 10^{-6} \cdot \text{m} \quad i := 0, 1 \dots 5$$

$$\text{Layers} := \begin{pmatrix} \text{"Pt Electrode"} \\ \text{"PZT"} \\ \text{"Pt Electrode"} \\ \text{"Thermal SiO2"} \\ \text{"Silicon"} \\ \text{"Buried SiO2"} \end{pmatrix} \quad E := \begin{pmatrix} 171 \\ 72.5 \\ 171 \\ 79 \\ 169 \\ 79 \end{pmatrix} \cdot 10^9 \cdot \frac{\text{N}}{\text{m}^2} \quad d := \begin{pmatrix} 0.1 \\ 1.0 \\ 0.1 \\ 0.3 \\ 8.0 \\ 1.2 \end{pmatrix} \cdot 10^{-6} \cdot \text{m} \quad \nu := \begin{pmatrix} 0.39 \\ 0.28 \\ 0.39 \\ 0.3 \\ 0.065 \\ 0.3 \end{pmatrix}$$

Area of the layer

Distance of the layer centroid from the top surface

Distance of the Neutral Axis from the top surface

$$A := d \cdot b$$

$$z_i := \sum_{j=0}^i d_j - \frac{d_i}{2}$$

$$A = \begin{pmatrix} 200 \\ 2 \times 10^3 \\ 200 \\ 600 \\ 1.6 \times 10^4 \\ 2.4 \times 10^3 \end{pmatrix} \cdot 10^{-12} \cdot \text{m}^2$$

$$z = \begin{pmatrix} 0.05 \\ 0.6 \\ 1.15 \\ 1.35 \\ 5.5 \\ 10.1 \end{pmatrix} \cdot 10^{-6} \cdot \text{m}$$

$$z_M := \frac{\sum_i z_i \cdot E_i \cdot A_i}{\sum_i E_i \cdot A_i}$$

$$T := \sum_i d_i$$

$$z_M = 5.383 \times 10^{-6} \cdot \text{m} \quad T = 10.7 \cdot 10^{-6} \cdot \text{m}$$

$$T - z_M = 5.317 \times 10^{-6} \cdot \text{m}$$

$$I_{t_i} := \frac{b \cdot (d_i)^3}{12} + A_i \cdot (z_i - z_M)^2$$

$$I_t \cdot 10^{12} = \begin{pmatrix} 5.688 \\ 45.914 \\ 3.583 \\ 9.762 \\ 85.554 \\ 53.696 \end{pmatrix} \cdot 10^{-9} \cdot \text{m}^4$$

Overall beam value with Normalised Young's Modulus equivalent to a silicon-only beam.

$$I_{z2} := \sum_i \left(I_{t_i} \cdot E_i \cdot \frac{10^{12}}{E_4} \right)$$

$$I_{z2} = 144.295 \cdot 10^{-9} \cdot \text{m}^4$$

Non-multimorph beam comprising the Silicon layer only (for comparison).

$$I_{Si} := \frac{b}{12} \cdot (d_4)^3 \cdot 10^{12}$$

$$I_{Si} = 85.333 \cdot 10^{-9} \cdot \text{m}^4$$

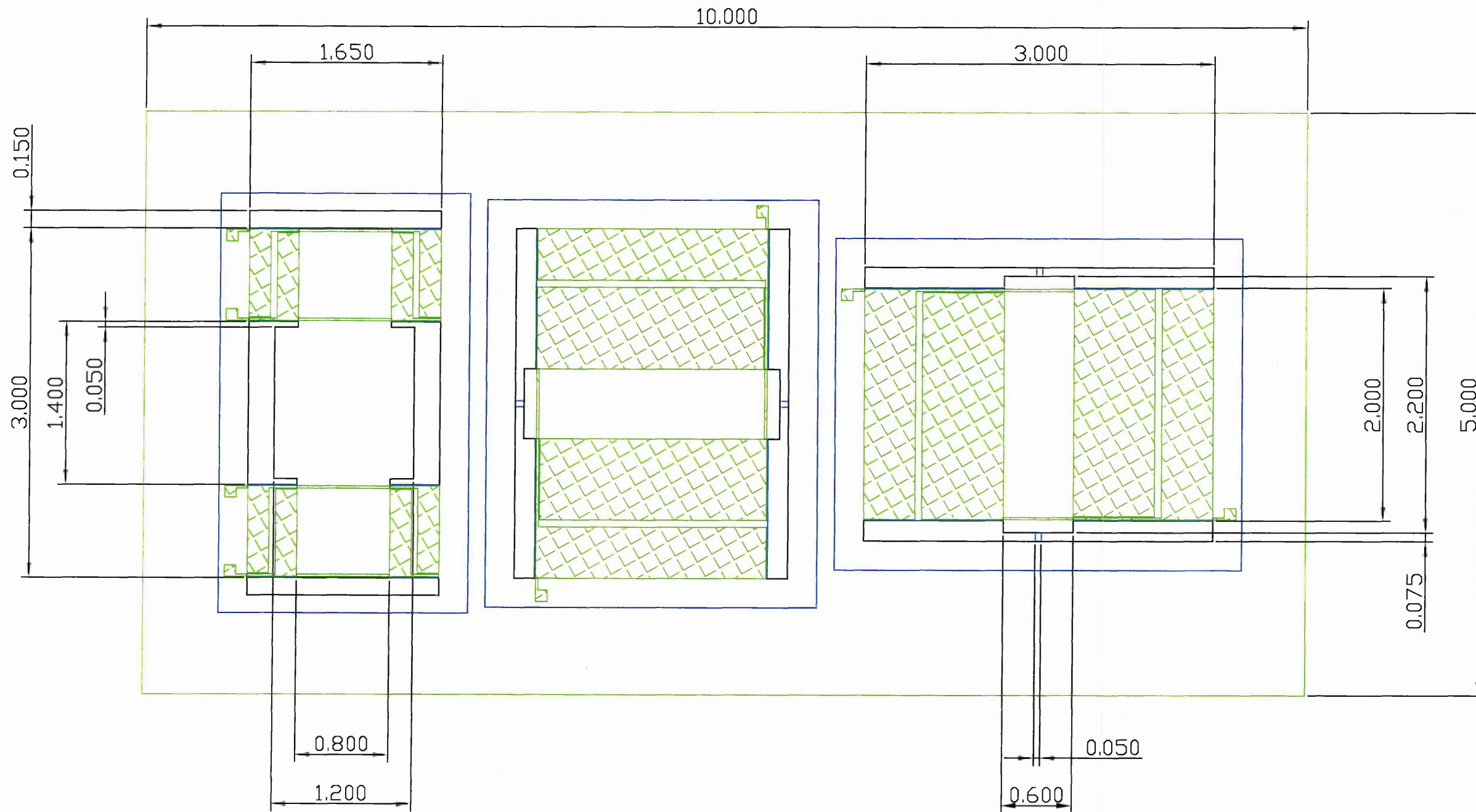
Appendix 2. Table of dimensions for proposed devices


Optimisation of device variables for alternative accelerometer designs

	X & Y		Z		Z	
	Modified Semi-symmetric		Semi-symmetric		Highly symmetric	
	1 pair compliant beams y-axis		2 pairs of beams			
	1 pair rigid beams on x-axis		on y-axis			
Dimensions (DRIE etch mass, beam) (um)					Inset	
ax	1400	1100	1200	1200	1500	700
ay	300	300	300	500	600	700
tw	525	525	525	525	525	525
L	1180	1200	490	455	425	525
	75	75				
b	2500	2000	600	800	800	1000
	50	50				
d	8	8	8	8	8	8
a1	ax		ax - b/2	ax - b/2	ax - b/2	
a2	ay		ay	ay	400	700
Mass (mg)						
M	2.055	1.615	1.761	2.936	3.592	2.398
Resonant frequency (Hz)						
fz	16000	18025	5038	5036	5043	5026
fy	5050	5066	8125	8894	7309	6980
fx	18745	20534	6106	5545	6834	6980
Charge Output (pC/g)						
qz	0.426	0.264	4.966	7.136	7.618	7.759
qy	8.606	6.809	2.287	2.494	3.139	2.009
qx						
Acceleration limit (fracture strength) (g)						
Az	2287	2902				
Ay						
Ax	6131	6162				
1um thk Piezo has 80% coverage over beams						
Cap'tance	0.031 uF	0.025 uF	0.006 uF	0.008 uF	0.007 uF	0.011 uF
Area y	2960	3000	1580	1910	1650	2450
x	2950	2350	2500	2500	3100	2450

Appendix 3. Drawings for Prototype Accelerometers

TAA001.	Three axis sensor	116
TAA002.	Oversize, high output sensor	117
TAA003.	Single axis, highly symmetrical sensor.....	118

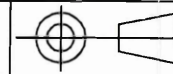


- REVERSE SIDE ETCH ON BASE WAFER
- DEVICE LAYER ETCH
-  PZT SENSOR POSITIONS

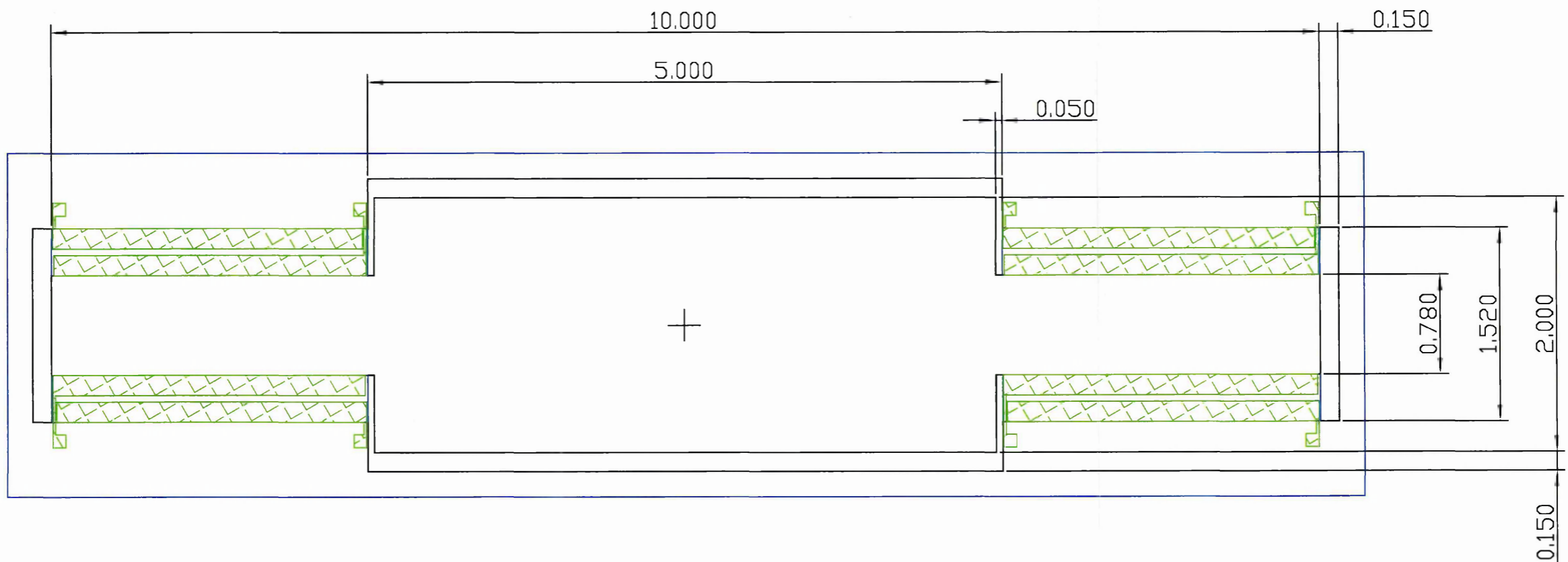
NOTE :-
THIS DRAWING IS CREATED AS LAYERS TO
CORRESPOND TO THE PATTERN STAGES OF
FABRICATION.

Initial Issue		A
		30/05/02
CHANGE DESCRIPTION		
TITLE		DRAWING No.
COMPLETE DEVICE FOR		TAA-001
FIRST TRIAL MASK		

IF IN DOUBT ASK	SCALE 20:1	TOLERANCES See Drg	DIMENSIONS IN mm	DRAWN DATE JMH 30/05/02	This drawing and all information contained in it remains the copyright of ETB Ltd
-----------------	---------------	-----------------------	---------------------	----------------------------------	--

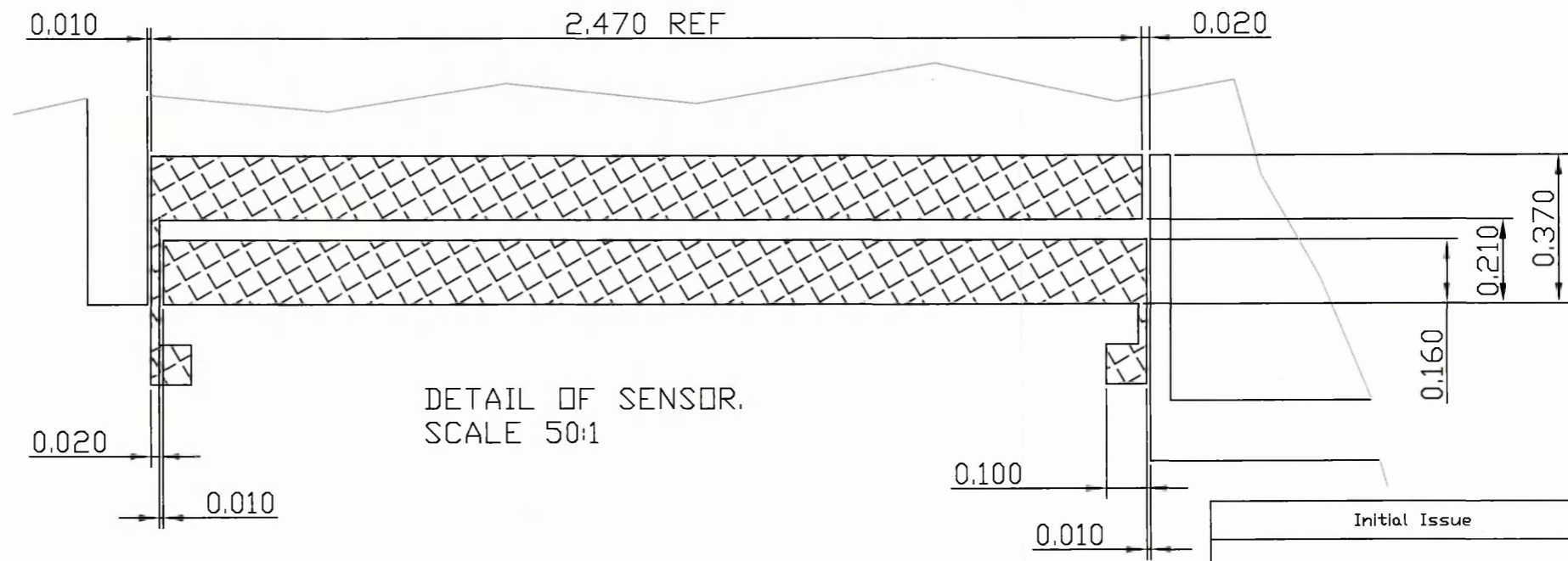


ISSUE
SHT 1 OF 1

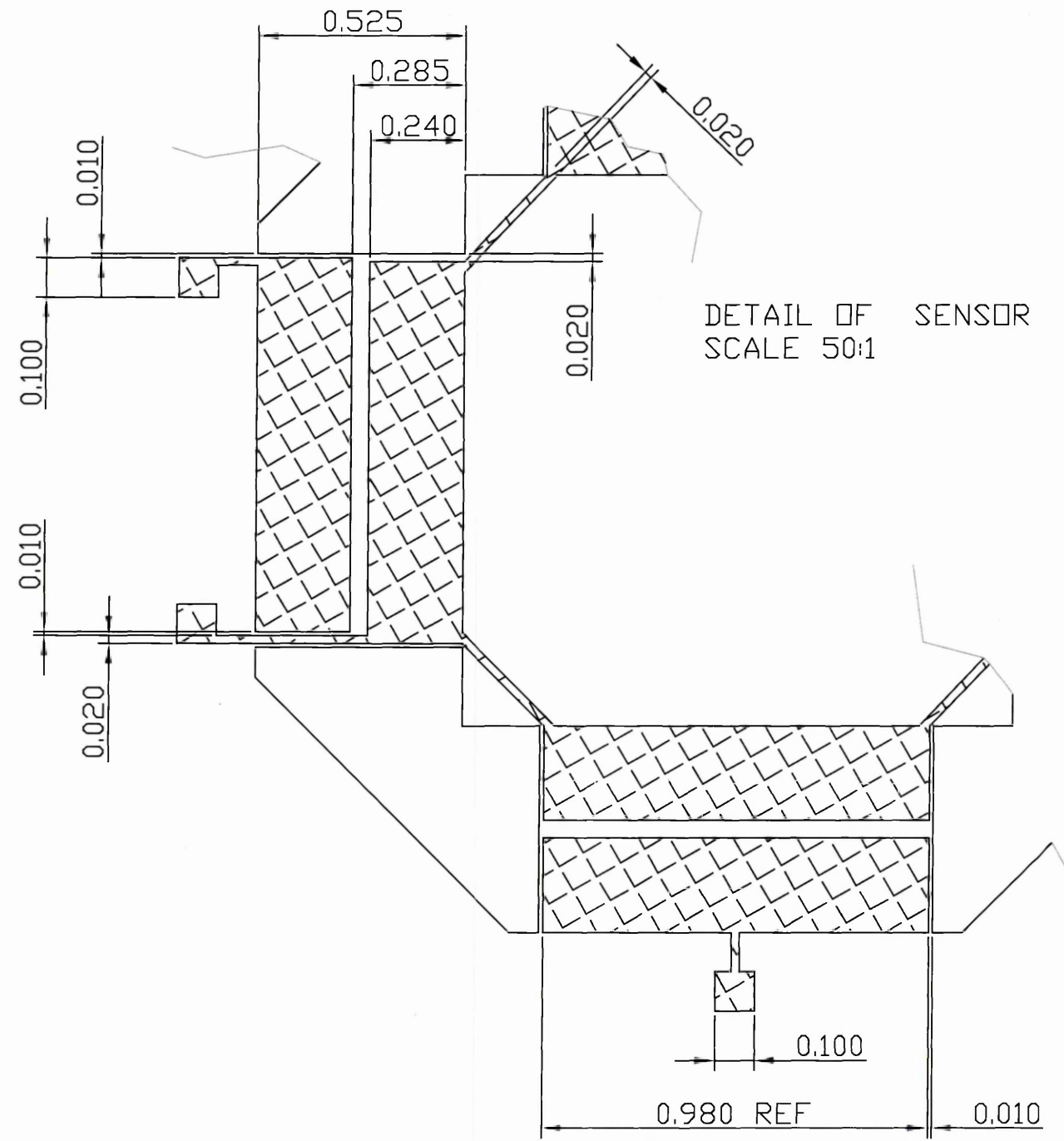
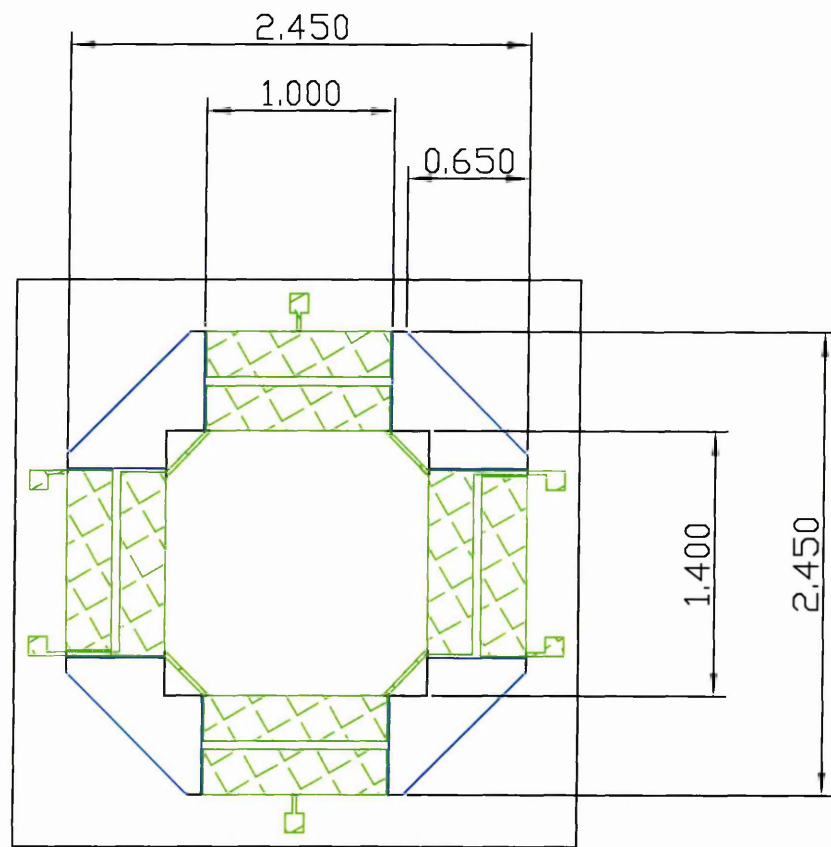


NOTE 1-
 THIS DRAWING IS CREATED AS LAYERS TO CORRESPOND TO THE PATTERN STAGES OF FABRICATION. THE SILICON DIMENSIONS ARE SYMMETRICAL ABOUT BOTH AXES. THE PZT SENSOR PATTERN REPEATS IN 4 PLACES.

- REVERSE SIDE ETCH ON BASE WAFER
- DEVICE LAYER ETCH
- PZT SENSOR POSITIONS



IF IN DOUBT ASK	SCALE 20:1	TOLERANCES See Drg	DIMENSIONS IN mm	DRAWN DATE JMH 30/05/02	This drawing and all information contained in it remains the copyright of ETB Ltd		ISSUE SHT 1 OF 1	Initial Issue	A 30/05/02
								CHANGE DESCRIPTION	
TITLE OVERSIZE DEVICES FOR FIRST TRIAL MASK								DRAWING No. TAA-002	



- REVERSE SIDE ETCH ON BASE WAFER
- DEVICE LAYER ETCH
- PZT SENSOR POSITIONS FOR Z-AXIS

NOTE 1—
 THIS DRAWING IS CREATED AS LAYERS TO CORRESPOND TO THE PATTERN STAGES OF FABRICATION.
 THE SILICON DIMENSIONS ARE SYMMETRICAL ABOUT BOTH AXES.
 THE PZT SENSOR PATTERN REPEATS IN 2 PLACES.

Initial Issue	A 30/05/02
CHANGE DESCRIPTION	ISSUE & DATE
TITLE HIGH-SYM DEVICE FOR FIRST TRIAL MASK	DRAWING No. TAA-003

IF IN DOUBT ASK	SCALE 20:1	TOLERANCES See Drg	DIMENSIONS IN mm	DRAWN DATE JMH 30/05/02	This drawing and all information contained in it remains the copyright of ETB Ltd	ISSUE SHT 1 OF 1
-----------------	---------------	-----------------------	---------------------	----------------------------------	---	---------------------

Appendix 4. Scaling Factor Analysis

In order to work with more convenient units in NISA, it was decided to use millimetres as the default length dimension, and leave mass and time in standard SI units. This appendix checks the scaling factors used on different dimensions, as input to the NISA files.

***MATERIAL**

EX	,	1,0, 1.69000E+08,	mN/mm ²	= N/m ² *E-03
NUXY	,	1,0, 6.00000E-02,	-	
GXY	,	1,0, 6.41000E+07,	mN/mm ²	= N/m ² *E-03
DENS	,	1,0, 2.33000E-06	kg/mm ³	= kg/m ³ *E-09

***MATPIEZO**

EXX	,	2,0, 0,0.10443E-16,0	MF/mm	= F/m *E-09
EYY	,	2,0, 0,0.10443E-16,0		
EZZ	,	2,0, 0,6.46050E-18,0		
PZ13	,	2,0, 0, -0.308E-05,0	C/mm ²	= C/m ² *E-06
PZ23	,	2,0, 0, -0.308E-05,0		
PZ33	,	2,0, 0,0.1095E-04,0		
PZ52	,	2,0, 0,0.1025E-04,0		
PZ61	,	2,0, 0,0.1025E-04,0		

****EXECUTIVE data deck**

GFACTOR = 9810.0		mm/s ²	= m/s ² *E+03
------------------	--	-------------------	--------------------------

***GROUND**

LABEL	IFN	IAT	SFTR
ACCZ	101	201	1.000000E+03
ACCY	101	202	1.000000E+03
ACCX	101	203	1.000000E+03

'1000g' Acceleration force applied is

$$GFACTOR \times SFTR = 9.81e6 \text{ mm/s}^2$$

Voltage and electric field are output from the PZT elements when they are strained. The units convert as :-

$$V = J/C \quad J = N.m/s^2 = kg.m^2/s^2 \quad C \equiv kg/s$$

$$\text{giving} \quad V = m^2/s = 10^6 \text{ mm}^2/s$$

Appendix 5. Full Results from Ground Acceleration FE

TAA001

	Voltage	Stress	Voltage	Stress	Capacitance	Charge	Dielectric (F/m)
			mV/g	N/m ²	nF	pC/g	6.46E-09
TAA001 Y					28.891		Side Beams
X 50g	7.26E-08	71.62	1.451E-12	71620		0.000	4799
	-5.72E-08	-71.62	-1.145E-12	-71620		0.000	-4799
						3.750E-11	
Y 50g	8.37E+03	2714	1.675E-01	2714000		2.419	7845
	-8.37E+03	-2714	-1.675E-01	-2714000		-2.419	-7845
						4.838	
MathCAD			0.165		29.458	4.873	
Z 50g	-5.58E+00	161.3	-1.116E-04	161300		-0.002	19127
	-5.58E+00	-232.4	-1.116E-04	-232400		-0.002	-18952
						0.000E+00	
ALL 50g	8.37E+03	2717	1.674E-01	2717000		2.418	31771
	-8.38E+03	-2720	-1.676E-01	-2720000		-2.421	-30284
						4.838	
	2 micron misalignment						
X 50g	6.41E-03		1.282E-07			0.000	
	4.09E-03		8.176E-08			0.000	
		Cross axis	0.0000%			6.701E-07	
Y 50g	8.34E+03		1.669E-01			2.411	
	-8.38E+03		-1.676E-01			-2.421	
		Reduction in sensitivity		0.1376%		4.832	
Z 50g	-3.71E+00		-7.424E-05			-0.001	
	-7.73E+00		-1.545E-04			-0.002	
		Cross axis	0.0240%			0.001	
All 50g	8.34E+03		1.667E-01			2.408	
	-8.38E+03		-1.677E-01			-2.422	
						4.830	
TAA001 Z					7.252		
X 50g	7.57E-06	4264	1.513E-10	4264000		0.000	
	-7.57E-06	-4264	-1.514E-10	-4264000		0.000	
						1.098E-09	
Y 50g	3.92E-07	2579	7.834E-12	2579000		0.000	
	-3.98E-07	-2579	-7.957E-12	-2579000		0.000	
						5.726E-11	
Z 50g	3.79E+04	9173	7.589E-01	9173000		2.752	
	-3.79E+04	-9210	-7.579E-01	-9210000		-2.748	
						5.500	
MathCAD			0.704		7.643	5.380	
ALL 50g	3.79E+04	15956	7.589E-01	15956000		2.752	
	-3.79E+04	-14894	-7.579E-01	-14894000		-2.748	
				5.79E-11		5.500	
	2 micron misalignment						
X 50g	-4.57E+01		-9.138E-04			-0.003	
	-7.10E+01		-1.420E-03			-0.005	
		Cross axis	0.0334%			0.002	
Y 50g	1.05E+01		2.098E-04			0.001	
	-1.10E+01		-2.201E-04			-0.001	

		Cross axis		0.0283%		0.002
Z 50g	3.79E+04			7.571E-01		2.745
	-3.78E+04			-7.560E-01		-2.741
		Reduction in sensitivity		0.2422%		5.486
All 50g	3.78E+04			7.555E-01		2.739
	-3.78E+04			-7.567E-01		-2.744
						5.483

TAA002

	Voltage	Stress	Voltage	Stress	Capacitance	Charge	Dielectric
			mV/g	N/m ²	nF	pC/g	6.46E-09
							(F/m)
TAA002 Y axis sensitive					19.803		
X 50g	5.38E-07	972	1.075E-11	972000		0.000	
	-5.35E-07	-972	-1.070E-11	-972000		0.000	
						2.124E-10	
Y 50g	2.15E+04	5839	4.304E-01	5839000		4.261	
	-2.13E+04	-5839	-4.265E-01	-5839000		-4.223	
						8.485	
MathCAD			0.404		20.651	8.337	
Z 50g	9.65E+01	11907	1.929E-03	11907000		0.019	
	9.65E+01	-11940	1.929E-03	-11940000		0.019	
						1.980E-08	
ALL 50g	2.15E+04	18584	4.304E-01	18584000		4.261	
	-2.13E+04	-16804	-4.265E-01	-16804000		-4.223	
						8.485	
	2 micron misalignment						
X 50g	1.25E-02		2.491E-07			0.000	
	5.84E-03		1.167E-07			0.000	
		Cross axis	0.0000%			1.311E-06	
Y 50g	2.12E+04		4.246E-01			4.205	
	-2.15E+04		-4.299E-01			-4.257	
		Reduction in sensitivity		0.2722%		8.461	
Z 50g	1.39E+02		2.782E-03			0.028	
	5.19E+01		1.038E-03			0.010	
		Cross axis	0.2036%			0.017	
All 50g	2.14E+04		4.274E-01			4.232	
	-2.14E+04		-4.289E-01			-4.247	
						8.479	
TAA002 Z axis sensitive					19.803		
X 50g	6.43E-07	972	1.286E-11	972000		0.000	
	-6.46E-07	-972	-1.291E-11	-972000		0.000	
						2.552E-10	
Y 50g	1.96E-05	5907	3.917E-10	5907000		0.000	
	-1.96E-05	-5907	-3.927E-10	-5907000		0.000	
						7.767E-09	
Z 50g	4.96E+04	11766	9.924E-01	11766000		9.826	
	-4.98E+04	-11834	-9.967E-01	-11834000		-9.869	
						19.695	
MathCAD			0.915		20.651	18.891	
ALL 50g	4.96E+04	18474	9.924E-01	18474000		9.826	
	-4.98E+04	-16727	-9.967E-01	-16727000		-9.869	

							19.695
	2 micron misalignment						
X 50g	-3.87E+01			-7.735E-04			-0.008
	-7.98E+01			-1.597E-03			-0.016
		Cross axis		0.0414%			0.008
Y 50g	1.91E+00			3.828E-05			0.000
	-1.88E+00			-3.761E-05			0.000
		Cross axis		0.0038%			0.001
Z 50g	4.95E+04			9.895E-01			9.798
	-4.97E+04			-9.939E-01			-9.841
		Reduction in sensitivity		0.2828%			19.639
All 50g	4.94E+04			9.879E-01			9.782
	-4.97E+04			-9.946E-01			-9.848
							19.630

TAA003

	Voltage	Stress	Voltage	Stress	Capacitance	Charge	Dielectric
			mV/g	N/m ²	nF	pC/g	6.46E-09
							(F/m)
TAA003					12.022		
X 50g	5.86E-06	3087	1.172E-10	3087000		0.000	
	-5.86E-06	-3087	-1.171E-10	-3087000		0.000	
							1.41E-09
Y 50g	3.22E-06	3087	6.443E-11	3087000		0.000	
	-3.24E-06	-3087	-6.478E-11	-3087000		0.000	
							7.767E-10
Z 50g	2.37E+04	6038	4.746E-01	6038000		2.853	
	-2.37E+04	-6066	-4.740E-01	-6066000		-2.849	
							5.702
MathCAD			0.446		12.399		5.533
ALL 50g	2.37E+04	10378	4.746E-01	10378000		2.853	
	-2.37E+04	-9754	-4.740E-01	-9754000		-2.849	
							5.702
	2 micron misalignment						
X 50g	-6.27E+00			-1.255E-04			-0.001
	-2.48E+01			-4.966E-04			-0.003
		Cross axis		0.0391%			0.002
Y 50g	-6.26E+00			-1.252E-04			-0.001
	-2.48E+01			-4.966E-04			-0.003
		Cross axis		0.0392%			0.002
Z 50g	2.37E+04			4.730E-01			2.843
	-2.36E+04			-4.724E-01			-2.840
		Reduction in sensitivity		0.3344%			5.683
All 50g	2.36E+04			4.720E-01			2.837
	-2.36E+04			-4.727E-01			-2.841
							5.679

Appendix 6. Signal Coupling in the Device-Layer Silicon

Analysis of the capacitance and resistance of the Device-Layer Silicon

The construction of the three-axis accelerometer prototype configures the bottom electrode of each sensor as the signal electrode, with all top electrodes connected to earth. This leads to simplified electrical connection, but capacitive coupling of the three signals through the device-layer silicon. The following calculations quantify the cross-axis coupling through this route.

Wafer Construction

Layer	Thickness	Resistivity	Dielectric (ϵ_r)
PZT sensor	1.0 μm		730
Field oxide	0.3 μm		3.82
Device-Layer Silicon	8.0 μm	1-10 $\Omega\text{-cm}$	
Buried Oxide Layer	1.5 μm		3.82
Handle-Layer Silicon	500 μm	1-10 $\Omega\text{-cm}$	

The following electrical properties are calculated based on drawing TAA001, shown in Appendix 3.

Sensor Capacitances

$C = \frac{\epsilon_0 \epsilon_r A}{t}$	Area	Capacitance
Capacitance of X or Y axis sensor	4.80 mm^2	31.0 nF
X or Y Bottom Electrode to Device-Layer	2.85 mm^2	321 pF
X or Y Device-Layer to Handle-layer	2.85 mm^2	64 pF

Capacitor Reactance

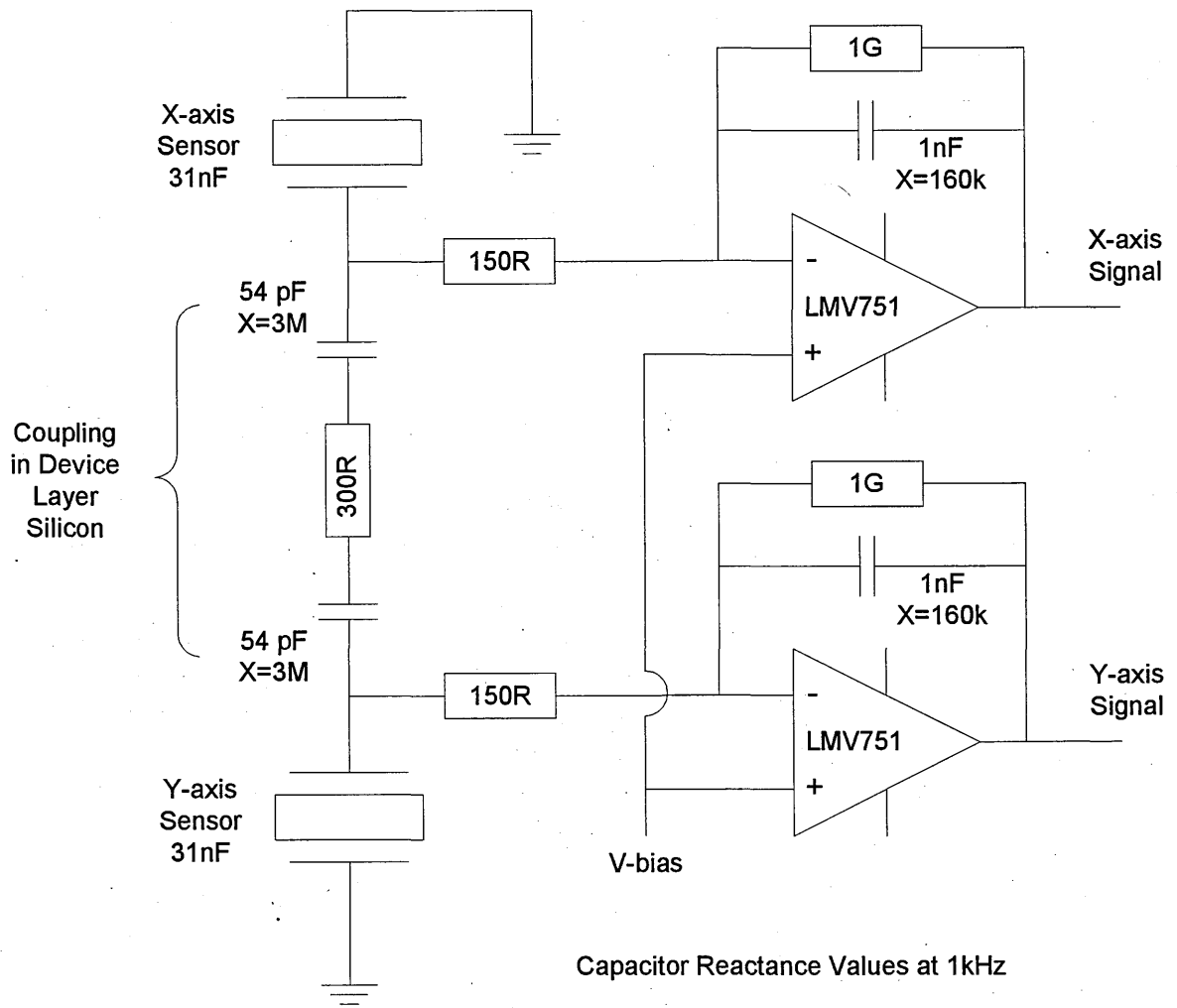
$X = \frac{1}{2\pi f C}$	Frequency	Reactance
X or Y Bottom Electrode to Device-Layer	10 Hz	300 $\text{M}\Omega$
	1 kHz	3.0 $\text{M}\Omega$
Amplifier Feedback Capacitor (1 nF)	10 Hz	16 $\text{M}\Omega$
	1 kHz	160 $\text{k}\Omega$

Handle-Layer Silicon Resistance

$R = \frac{\rho.L}{w.t}$	Length	Width	Resistance
Between X and Y sensors	0.15 mm	5.0 mm	6 Ω
Across X or Y sensor	Significantly affected by clearance beside beams		
Along X or Y sensor	3.6 mm	2.4 mm allowing gaps	300 k Ω

From the equivalent circuit diagram below, it can be seen that the cross-axis path from one sensor electrode to another is the sum of the two capacitor reactance values and the silicon device-layer resistance. From the figures calculated, it can be seen that this is dominated by the capacitor reactance between the electrodes and the device-layer silicon.

At 1 kHz, the reactance between sensors is of the order of 6 M Ω , compared to 150 Ω input resistors and 160 k Ω feedback reactance for the amplifiers. The amplifier signal inputs (negative) should be at virtually identical voltage, since the positive inputs are connected to a shared reference voltage, therefore the cross-axis signal through the silicon device-layer is of the order of 300 in 6 000 000, or 50ppm. This improves as the frequency reduces, so is well below the required resolution of the sensor.



Equivalent Accelerometer Circuit

showing additional components due to cross-axis coupling in the device layer silicon